10-16-2015 12:00 AM

Hyperpolarized 129Xe Magnetic Resonance Imaging of Radiation-Induced Lung Injury

Ozkan Doganay
The University of Western Ontario

Supervisor
Giles Santyr
The University of Western Ontario

Graduate Program in Medical Biophysics
A thesis submitted in partial fulfillment of the requirements for the degree in Doctor of Philosophy

Recommended Citation

Doganay, Ozkan, "Hyperpolarized 129Xe Magnetic Resonance Imaging of Radiation-Induced Lung Injury" (2015). *Electronic Thesis and Dissertation Repository*. 3297.
https://ir.lib.uwo.ca/etd/3297

Hyperpolarized ^{129}Xe Magnetic Resonance Imaging of Radiation-Induced Lung Injury

Thesis format: Integrated Article

by

Ozkan Doganay

Graduate Program in Medical Biophysics

A thesis submitted in partial fulfillment
of the requirements for the degree of
Doctor of Philosophy

The School of Graduate and Postdoctoral Studies
The University of Western Ontario
London, Ontario, Canada

Abstract

Lung cancer is the largest contributor to cancer-related mortality worldwide. Only 20% of stage III non-small cell lung cancer patients survive after 5-years post radiation therapy (RT). Although RT is an important treatment modality for lung cancer, it is limited by Radiation-Induced Lung Injury (RILI). RILI develops in two phases: (i) the early phase (days-weeks) referred to radiation pneumonitis (RP), and (ii) the late phase (months). There is a strong interest in early detection of RP using imaging to improve outcomes of RT for lung cancer. This thesis describes a promising approach based on ^{129}Xe gas as a contrast agent for Magnetic Resonance Imaging (MRI) of the lung airspace due to the large increase in signal possible by spin exchange optical pumping, or hyperpolarization (Hp). Additionally, ^{129}Xe provides unique functional information due to its relatively high solubility and significant chemical shift in pulmonary tissue (PT) and red blood cell (RBC) compartments. In this thesis, a specialized Hp ^{129}Xe MRI method was developed for detection of gas exchange abnormalities in the lungs associated with thoracic RT. In particular, the feasibility of quantifying the early phase of RILI is demonstrated in a rat model of RILI two weeks post-irradiation with a single fraction dose of 18 Gy. The challenge of low signal-to-noise ratio (SNR) in the dissolved phases was addressed in this work by development and construction of a Transmit-Only/Receive-Only radiofrequency coil. Another challenge addressed in the thesis was the lack of imaging techniques that provide sufficient spatial and temporal information for gas exchange. Therefore, a novel Hp ^{129}Xe MRI technique was developed based on the multi-point IDEAL pulse sequence. The combination of these two developments enabled investigation of regional gas exchange changes associated with RP in the rat lung two weeks post-irradiation to assess the feasibility of early detection of RILI. Theoretical analysis of the gas exchange curves enabled measurements of average PT thickness (L_{PT}) increases consistent with histology and relative blood volume (V_{RBC}) reductions in the irradiated animal cohort compared to a non-irradiated cohort, and between irradiated right lungs compared to unirradiated left lungs in the irradiated cohort.

Keywords

Radiation-induced lung injury, pneumonitis, Hyperpolarized ^{129}Xe, MRI, lung imaging, IDEAL, dissolved xenon, pulmonary tissue, red blood cell, gas exchange, spiral, point spread function, rat, radiofrequency coil.

Co-Authorship Statement

This thesis is based on work published in the following three manuscripts:

(1) Ozkan Doganay, Kundan Thind, Trevor Wade, Alexei Ouriadov, Giles E. Santyr, Transmit-only/receive-only radiofrequency coil configuration for hyperpolarized ^{129}Xe MRI of rat lungs, *Concepts in Magnetic Resonance Part B: Magnetic Resonance Engineering* 2015, DOI: 10.1002/cmr.b.21288.

For this manuscript, Ozkan Doganay was responsible for optimizing the sensitivity using the numerical COMSOL simulations as well as building both transmit and receive coils and corresponding electronic circuits, bench top measurements, experimental data acquisition and analysis of data including MATLAB coding. Dr. Kundan Thind provided meaningful discussion. Dr. Trevor Wade and Dr. Alexei Ouriadov helped with MRI calibration experiments and *in vivo* imaging. Dr. Giles Santyr provided guidance throughout the project and assistance with the manuscript preparation. Additionally, Elaine Hegarty helped with animal preparation and Krzysztof Wawrzyn helped with Hp ^{129}Xe gas production.

(2) Ozkan Doganay, Trevor Wade, Elaine Hegarty, Charles McKenzie, Rolf F. Schulte, Giles E. Santyr, Hyperpolarized Xenon-129 MR imaging of the rat lung using spiral IDEAL, *Magnetic Resonance in Medicine 2015,* DOI 10.1002/mrm.25911.

For this manuscript, Ozkan Doganay was responsible for the theoretical analysis and derivation of the corresponding equations as well as design and optimization of spiral trajectories and corresponding gradient waveforms, experiment design, data acquisition and analysis of data, including MATLAB coding. Dr. Trevor Wade, Dr. Charles McKenzie and Dr. Rolf F. Schulte provided meaningful discussion. Additionally, Elaine Hegarty assisted with animal preparation, Andrew Wheatley and Krzysztof Wawrzyn helped with Hp ^{129}Xe gas production. Dr. Giles Santyr provided guidance throughout the project and assistance with the manuscript preparation.

(3) Ozkan Doganay, Elaine Stirrat, Charles McKenzie, Rolf F. Schulte, Giles E. Santyr, Quantification of Regional Gas Exchange Changes using Hyperpolarized ^{129}Xe MRI in a Rat Model of Early Stage Radiation-induced Lung Injury, *Medical Physics* 2015 (in Revision).

For this manuscript, Ozkan Doganay was responsible for experiment design including installation and optimization of the insert gradient and RF coils, experimental data acquisition, and analysis of data including post-processing with MATLAB and segmentation. Elaine Stirrat assisted with animal preparation and performing histological preparation and interpretation. Dr. Charles McKenzie and Dr. Rolf F. Schulte provided meaningful discussion. Dr. Giles Santyr provided guidance throughout the project and assistance with the manuscript preparation.

Acknowledgments

I would like to gratefully acknowledge Dr. Giles Santyr for giving me the opportunity to conduct this research in his group. His supervision provided me a well-rounded educational experience. Although he moved to another institution mid-way through my PhD study, he was always available any time I needed support. I thank him for his expertise, guidance, encouragement, and patience throughout my research.

I also would like to thank the following people:
All of my fellow colleagues and past/present members of the Santyr lab. Specifically, Elaine Hegarty for assisting me with animal preparation and performing tissue histology, and Krzysztof Wawrzyn for the help with polarizing gas for my experiments as well as Dr. Trevor Wade, Dr. Alexei Ouriadov, and Dr. Kundan Thind.

Dr. Timothy Scholl and his group for assistance with RF coil. Specifically, Yonathan Araya for his supports, useful discussion related to research and revising my thesis.

Dr. Blaine Chronik, Dr. Carl Kumaradas, Yevgeniy Davletshin for providing access and useful discussion about Comsol.

Dr. Eugene Wong for contributing towards the rat irradiations.

My advisory committee, Dr. Paula J. Foster and Dr. Robert Bartha, for guidance and support throughout my graduate work.

Dr. Maria Drangova for giving me an RA position in her lab and her staff particularly Drs Junmin Liu and Ali Tavallaei for teaching me how to do image segmentation and for useful discussion related to research.

Finally, I would like to thank my wife for supporting me throughout my PhD. My wonderful babies: Batuhan and Berkay have hard time to understand the reason I have to go work on the weekends instead of playing games with them. I hope that one day they can read this thesis and understand why I had to go work on vacations. My wife has done a tremendous job keeping my sons happy and healthy while I am writing this thesis. I dedicated this thesis to my lovely wife and my sons.

Table of Contents

List of Tables

List of Figures

List of Appendices

List of Abbreviations and Symbols

^{129}Xe	Xenon-129
^{13}C	Carbon-13
ADC	Apparent Diffusion Coefficient
B_0	Main static magnetic field
B_1	Intensity of magnetic field of applied RF pulse
B_{1-}	Receive RF field obtained by the receive coil
B_{1+}	Transmit RF field created by the transmit coil
CSSR	Chemical Shift Saturation Recovery
CT	Computed Tomography
FGRE	Fast Gradient Recalled Echo
FID	Free Induction Decay
FOV	Field Of View
Gy	Gray
Hp	Hyperpolarized
IDEAL	Iterative Decomposition of water and fat with Echo Asymmetry and Least squares estimation
L_C	Capillary average thickness
L_{PT}	Pulmonary tissue average thickness
M_0	Equilibrium magnetization
MR	Magnetic Resonance
MRI	Magnetic Resonance Imaging
M_{xy}	Transverse magnetization
M_z	Longitudinal magnetization
NMR	Nuclear Magnetic Resonance
NSCLC	Non-Small Cell Lung Carcinoma
PET	Positron Emission Tomography
PFTs	Pulmonary Function Tests
PSF	Point Spread Function
PT	Pulmonary Tissue
PTA	Percent Tissue Area
RBC	Red Blood Cell
RF	Radiofrequency
RILI	Radiation-Induced Lung Injury
ROI	Region of interest
RP	Radiation Pneumonitis
RT	Radiation Therapy
SBRT	Stereotactic Body Radiotherapy
SCLC	Small Cell Lung Carcinoma
SPECT	Single-Photon Emission Computed Tomography
SRN	Signal-to-Noise Ratio
T	Tesla
T_1	Longitudinal relaxation time
T_2	Transverse relaxation time
T_2^*	Apparent transverse relaxation time

TE	Echo Time
TO/RO	Transmit-Only / Receive-Only
TR	Repetition Time
T_{read}	Read-out time
α	Flip angle
α_G	Flip angle (delivered to gas phase of ^{129}Xe)
α_{PT}	Flip angle (delivered to dissolved phase of ^{129}Xe in pulmonary tissue)
γ	Gyromagnetic ratio
V_{RBC}	Relative RBC Volume
ω	Carrier frequency of the RF pulse
ω_0	Larmor frequency

Chapter 1 : Introduction

This chapter is intended to provide the introduction and motivation for the work presented in chapters 2, 3 and 4. First, an overview of lung physiology, lung cancer, and radiation induced lung injury (RILI), including the importance of early detection, will be explained. Furthermore, the advantages and limitations of clinical imaging modalities, are discussed with respect to lung imaging and RILI. A brief description of the principles of hyperpolarized (Hp) Magnetic Resonance Imaging (MRI), radiofrequency (RF) coils, and pulse sequence developments will be given. Finally, the hypothesis and specific objectives of the thesis project will be presented.

1.1 Overview and Motivation

Lung cancer is the largest contributor to cancer related deaths worldwide due to its low survival rate. Over 26,000 new lung cancer patients were reported in 2014 within Canada alone (1). Most cases are diagnosed as non-small cell lung cancer (~85%), for which radiotherapy (RT) is the most prominent treatment method (2). Although RT is successful in treating the cancer, there are undesirable consequences to the quality of life of the patient due to inadvertent injury of the normal lung tissue, known as Radiation-Induced Lung Injury (RILI). Current methods for assessing the severity of RILI include pulmonary function tests (PFTs), computed tomography (CT), single-photon emission computed tomography (SPECT), and positron emission tomography (PET). Although great advances in these fields have been made, there is still a need for a non-ionizing imaging technique to assess regional functional (e.g. gas exchange) changes associated with RILI.

Novel Hp MRI techniques have been shown to be more sensitive to the early phase of RILI than other clinical imaging modalities and PFTs (3). Particularly, there is a strong interest in using Hp ^{129}Xe gas as a contrast agent for MRI of lung due to the large increase in signal possible by spin exchange optical pumping (factor up to 100,000), known as hyperpolarization. Hp ^{129}Xe has many applications in imaging of the lung airspace and in diagnosis of lung diseases, including chronic obstructive pulmonary disease, and asthma. In addition to imaging the lung airspace, ^{129}Xe promises to provide unique functional information due to its relatively high solubility and significant chemical shift in pulmonary tissue (PT) and red blood cell (RBC) compartments. Additionally, dynamic Hp ^{129}Xe MR spectroscopy has been shown to be sensitive in detection of RILI in a rat model as early as two weeks post-irradiation (4). The research described in this thesis is directed mainly to the development of hyperpolarized MR diagnostic tools and investigation of a pre-clinical models of RILI.

In this thesis, a novel Hp ^{129}Xe MRI technique of the dissolved phases (i.e. PT and RBC) is described and the feasibility of quantifying the early phase of RILI in a rat model two weeks post-irradiation is shown. Low Signal-to-Noise Ratio (SNR) was the largest limitation for imaging dissolved phases of Hp ^{129}Xe in the PT and RBC, therefore, a Transmit-Only/Receive-Only (TO/RO) RF coil is developed and constructed to increase the sensitivity. Another challenge of imaging the dissolved phases of ^{129}Xe, was the lack of fast imaging techniques that provide simultaneous spatial and spectral information to follow the gas exchange between alveolar air space and PT and RBC. Therefore, a novel rapid MR pulse sequence is developed to image the gas, PT, and RBC compartments, including temporal information about the gas exchange. Subsequently, the imaging approach is used to measure regional gas exchange changes in rat lung at two weeks post-irradiation using a single fraction dose of 18 Gy to assess the feasibility of early detection of RILI.

1.2 Healthy Lung Physiology

The lungs are the respiratory organ responsible for gas exchange, consisting primarily of (i) airways (trachea, bronchi and terminal airways) and (ii) gas-exchange units known as alveoli (5) as shown in Figure 1.1. The lung facilitates the gas exchange of oxygen and carbon dioxide between the bloodstream and air. The lung start with the trachea, which is composed of cartilage rings and divides into two main bronchi. Each bronchus sequentially branches up to 23 bronchioles until the alveoli are reached. Inhaled air travels through the trachea into the bronchi and finally into the alveoli, respectively. Human lungs have three right lobes and two left lobes, while rat lungs consist of four right lobes and one left lobe (6). Human lungs contain a collection of alveoli in the range of 400 to 500 million (7,8). The alveolus is the smallest subunit of the lungs, which facilitates the site of the gas exchange, encompassing a total gas exchange surface are of approximately 130 m^2 (9). Oxygen in the alveolus air sac diffuses into PT and finally into RBCs in the surrounding capillaries. Then, oxygenated blood is carried to the heart via the pulmonary veins. The total volume of the trachea, bronchi and alveolar air sacs encompasses approximately 80% of the lungs (i.e. gas space). The remaining 20% (i.e. non-gas space) includes PT and surrounding capillaries.

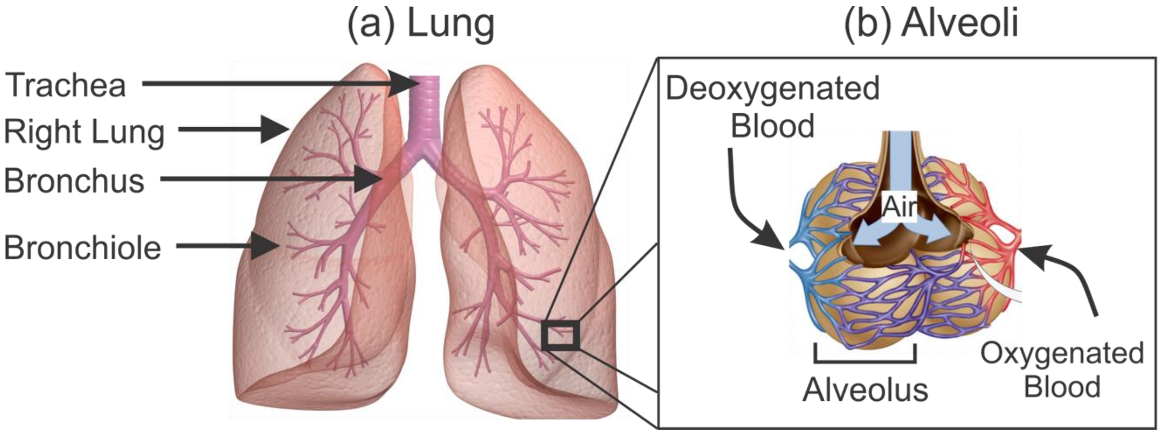

Figure 1.1: (a) Sketch of human lungs showing the trachea and major bronchi of the lungs (Lung rendering adapted from: http://www.londonlungcancer.co.uk/lungcancer/). (b) Sketch of alveoli showing the alveolus and capillaries (Alveoli rendering adapted from: Figure 44-19, Biological Science 2/e, Pulmonary system ©2005 Pearson Prentice Hall, Inc http://35.9.122.184/lecture-slides/LB145-lecture21-S2013.pdf).

1.3 Lung Cancer

Lung cancer remains the major leading cause of cancer related death in Canada and worldwide (1,10-12). The Canadian Cancer Society estimates 26100 new lung cancer cases in 2015, and reports by sex, one in 12 males and one in 14 females are expected to develop lung cancer in their life-times (13). According to the Ontario Lung Association, approximately 310,000 people in Canada will develop lung cancer over the next 30 years, resulting in a total health care cost of approximately $33.6 billion (14).

Based on the microscopic appearance of the tumor cell, lung cancer is classified into three major categories. Non-small cell lung carcinoma, NSCLC, is the most common type compromising 85-90% of incident rates (15). Small cell lung carcinoma, SCLC, and lung carcinoid tumor type account for the remaining 10-15% of all lung cancer (16). NSCLC is graded based on three criteria, known as TNM: (i) the size and location of tumor (T primary tumor), (ii) whether the tumor has spread to lymph nodes (N-regional lymph nodes) and (iii) tissues inside or outside the chest (M-distant metastasis) (17,18). After the TNM classification stage, a grouping is assigned using the numerical subset ranging from 0 to 4 to indicate the progressive extent of the malignant cancer (18). Together, the TNM classification and staging is used to select the most effective course of therapy and estimate the prognosis (19).

1.4 Advances in Treatment of Lung Cancer

The treatment options for lung cancer include chemotherapy, surgical resection, and RT (19). Chemotherapy has been the standard care of treatment in the clinic for patients with NSCLC and stage I-III, yielding a median overall survival of nine to twelve months (20-23). Platinum-based chemotherapy drugs (Cisplatin, Carboplatin, Oxaliplatin) are generally used for treatment of NSCLC patients. While the platinum-based chemotherapy drugs demonstrate substantial benefits for advanced NSCLC, the ideal number of therapy cycles still remains unclear, resulting in a dramatic change in the quality of life due to side effects (24).

Recent human trials using epidermal growth factor receptor tyrosine kinase (EGFR-TK) inhibitors have shown that the median overall survival for lung cancer has increased significantly, extending up to 30 months (25,26). The EGFR-TK molecular-based targeting agents (i.e., gefitinib, erlotinib) have been investigated as alternatives to chemotherapy owing to improved health outcomes while reducing previously observed toxic effects (27,28). The clinical use of molecular-based therapeutic strategies is limited by the increase in the cost of gene mutation screen tests (Bradbury et al., 2010). EGFR-TK inhibitors have been primarily restricted to specific patient groups who are female and/or who have no smoking history (26,28).

Surgical resection is also regarded as a treatment option for 20-30% of NSCLC and SCLC, particularly for stages I and II (29-31). However, surgical resection often results in pain, discomfort and decreased quality of life, including significant decline in physical, social and mental states (30). Surgery with adjuvant chemotherapy approaches have also been offered to patients with stage I NSCLC to provide additional therapeutic benefits, with a reported 4% improvement in 5-year survival to 29% (32). Recently, post-operative radiotherapy for patients with stage I NSCLC, after complete surgical resection with adjuvant chemotherapy, seems to confer an additional improvement in overall survival compared to adjuvant chemotherapy alone (33).

1.5 Radiation Therapy

Radiation therapy (RT) plays an important role for lung cancer treatment (19). RT has been recommended in approximately 75% of patients with NSCLC and 79% of patients with SCLC by Dalaney *et al.* in Australia (34) and 61% of all patients with lung cancer by Tyldesley *et al.* in Canada (35). However, only 16-43% of patients with SCLC and 40-51% of patients with NSCLC receive RT in the world (34). This discrepancy may be because the clinical use of radiation therapy is limited by many confounding factors, such as different health care policies, availability of RT units, low referral rates and limited information about toxic effects. However, the growing clinical interest in RT has led to more prominent guideline recommendations for RT as part of the treatment plan (36).

The primary goal of RT is to deliver a high radiation dose to the tumor while minimizing the damage to surrounding normal tissues. There are two types of radiation dosing schedules for lung cancer; (i) conventional fractionated radiation and (ii) stereotactic body radiotherapy (SBRT). Conventional radiation therapy involves the delivery of total dose of radiation (40-50 Gy) over many (25-30) small fractions within three to five weeks (37). Usually, these small fractions are administered every day with radiation doses of less than two Gy per fraction. Neoadjuvant RT followed by surgery has also improved the three-year survival rate to 45% for Stage III NSCLC (38). SBRT uses a high dose of radiotherapy to treat small gross tumor volumes (~60 Gy), based on using several radiation beams that intersect at the site of the tumor. Particularly, SRBT with 3D image guidance allows high precision with a relatively high fraction (20 Gy per fraction). A growing number of SBRT studies have demonstrated an improved 2-year survival for medically inoperable NSCLC patients (39,40). Although RT is mostly used for stage III NSCLC patients (40-66%), recent studies have also reported improved survival rates of stage IV NSCLC with SBRT and adjuvant chemotherapy treatment approaches (41). Early-phase toxic effects (i.e. RILI) are significantly worse for SBRT compared to conventional radiation therapy (19,42), though overall outcome is improved, for reasons that are not clear.

1.6 Radiation-Induced Lung Injury (RILI)

Irradiation of normal lung tissues during the course of RT results in RILI which includes a range of complications such as acute toxicities, chronic symptoms, and fibrosis that can all lead to organ failure. RILI is categorized into two phases: (i) early-phase and (ii) late-phase depending on the development of clinical symptoms, though one can occur without the other. The early-phase effect, also known as radiation pneumonitis (RP), is an acute inflammatory response that typically occurs within weeks following RT and is characterized with symptoms of dry cough and dyspnea (43). According to histopathology, RP includes extensive vasculature damage as well as tissue thickening (i.e. inflammation), alveolar edema and macrophage accumulation (44). After conventional RT, the overall incidence rates of moderate RP ranges from 15-50%, depending on the dose of the irradiated volume (45,46). While the incidence of severe RP is low, 5-35%, the mortality rates are high after SBRT (47,48). Vascular injury in the early-phase progresses with an extensive increase in collagen, which then transforms to fibrosis if the RP is not treated (49). Late-phase RILI represents collagen deposition and fibrosis after three months irradiation (43). Although radiation dosing strategies and adjuvant therapies have been developed to reduce short and long-term complications, RILI remains a significant problem for RT (50).

1.7 Diagnosis of Radiation-Induced Lung Injury

Monitoring of RP, during the course of RT, would allow for patient specific alterations to the therapy plan based on the severity of RILI. These alterations may include modification of radiation dose, or the use of adjuvant therapy, including chemotherapy and radio-protective and anti-inflammatory drugs (50,51). Detection of RP in its early phase would also help monitor the effectiveness of radio-protective changes. Minimizing normal tissue toxic effects after RT can increase the overall patient survival rate and improve the quality of life (50).

1.7.1 Pulmonary Function Tests

Pulmonary function tests (PFTs) are used to assess global lung function using measurements of forced expiratory volume (FEV), vital capacity, and carbon monoxide diffusing capacity (DLCO) (52). Changes induced in the lungs by thoracic irradiation are commonly evaluated by spirometry (53). Thoracic irradiation typically results in a reduction in the DLCO. However, FEV_1 (FEV measured at 1 second) may show inconsistently an increase or no changes in patients with centrally located lung lesions (54-56). Additionally, PFT measurements depends on the patients’ breathing efforts and need to be corrected for anemia (49). Furthermore, changes in whole lung function do not reveal regional information, limiting the ability of PFTs to resolve regional disease heterogeneities (57). Consequently, PFT can only detect RILI when a relatively large dose of 25 Gy is given and only three to six months post irradiation (54).

1.7.2 Chest Radiography / Computed Tomography

Computed tomography (CT) is an imaging modality that detects X-rays taken at different angles around the body to form cross-sectional images. Clinically, plane film chest X-ray and CT imaging are commonly utilized to assess RILI based on corresponding changes in lung density. Irreversible density gain and structural changes detected by X-rays in the lungs due to RILI occurs mainly in late phase due to the tissue remodeling. CT is capable of detecting late-phase fibrosis, two-three months following radiation doses of 40 Gy and above (53,58,59). CT perfusion is a relatively new technique which measure the perfusion by comparing the density changes in the region of interest during the intravenous injection of iodinated contrast material (60,61). Recent imaging developments in CT perfusion have shown that perfusion-based imaging techniques are more sensitive to early-phase RILI than conventional CT (62). Hu *et al.* reported that CT perfusion was a promising technique for detection of early-stage RILI after four weeks following a radiation dose of 60-62 Gy. However, both conventional RT and SBRT use treatment plans that are administered in two to three weeks, therefore detection of RILI four weeks post-radiation could be too late to adjust the therapy plan (e.g. radiation fractionation) or use pharmaceuticals (radio-protectors and anti-inflammatory drugs) (50,63,64).

1.7.3 SPECT

Single photon emission computed tomography (SPECT) is a nuclear imaging modality that images the distribution of gamma-emitting radionuclides in the body. SPECT is widely used to map both perfusion and ventilation changes due to RILI (53,65-67). SPECT ventilation is performed by inhaling radioactive tracers such as radioactive gas (e.g. ^{81m}Kr and ^{133}Xe), particulate aerosols labeled with radioactive compounds (i.e. ^{99m}Tc-DTPA) and ultrafine graphite particles labeled with ^{99m}Tc (i.e. Technegas) (68). One of the main concerns with detecting ventilation defects by means of ventilation SPECT is the inconsistency in intensity distribution of the radioactive gas when different radioactive gases are used within the same isogravitational planes (69). Particulate aerosols can diffuse to the alveolar capillary network and lead to ventilation image distortions. Furthermore, the clinical use of Technegas has not yet been approved by the US Food and Drug and Administration (69).

SPECT perfusion is a highly specialized lung perfusion imaging approach largely used in research settings and capable of assessing the reduction in lung perfusion associated with

RILI (70). SPECT perfusion lung imaging is accomplished by intravenous administration of albumin macroaggregates (MMA) labeled with ^{99m}Tc. Using SPECT perfusion imaging, Marks L.B. *et al.* demonstrated a 20-30% drop in blood perfusion in RT patients who received a radiation dose of 15-30 Gy (49). Despite SPECT perfusion imaging being more sensitive to RILI than CT, correction for attenuation, scatter, is required for quantitative imaging (71). Downscatter effects, which are caused from simultaneous ventilation and perfusion imaging using different radiotracers is also required to correct for interactions between ventilation and perfusion. Quantitative assessment of total blood volume is difficult since the sensitivity of SPECT scans significantly depends on patient positioning (69). SPECT is hampered by the poor spatial resolution (10-20 mm for 140 keV gamma rays from ^{99m}Tc) and long scan times (10-30 minutes).

1.7.4 PET

Positron emission tomography (PET) is a radionuclide imaging modality that images the distribution of intravenously injected positron emitting tracer in the region of interest. PET utilizes collinear 511 keV gamma rays offering a better spatial resolution (5-10 mm) than SPECT. PET with [^{18}F] fluorodeoxyglucose (FDG) provides functional information about metabolic activity due to the accumulation of FDG in inflamed tissue (72). Increased ^{18}F-FDG activity has been reported and correlated with clinical symptoms of RP in patients undergoing thoracic radiotherapy (3-12 weeks) receiving radiation doses of as low as 20 Gy (73). Hart *et al.* showed corelation between RP clinical symtoms and measured ^{18}F-FDG activity with an accuracy of approximately 50% (73). McCurdy *et al.* noted a linear relationship between post-RT ^{18}F-FDG uptake and radiation dose response 1-3 months after RT (74). Although high ^{18}F–FDG uptake corresponded to RP in these studies, the tumor growth was also associated with enhanced ^{18}F-FDG uptake restricting the sensitivity to detection of early-phase normal tissue changes (75,76). PET scans are limited by the lack anatomical references, therefore PET imaging frequently requires another imaging modality to provide anatomical images for the image registration such as CT (77). Another limitation with chest X-ray, CT, SPECT and PET are the radiation exposure of 2-3mSv for a typical ventilation and perfusion study.

1.7.5 Magnetic Resonance Imaging Methods

Conventional MRI provides images depicting the spatial distribution of hydrogen nuclei (i.e. proton) within water molecules in the body. MRI achieves high sensitivity due to the high molar concentration of water, which provides excellent soft tissue contrast with high temporal and spatial resolution without the need for ionizing radiation. However, lung imaging with MRI presents a challenge. The lungs have a low proton density and therefore low SNR since the pulmonary tissue (PT) volume comprises only ~ 20% of the total lung volume. Contrast-enhanced Gd-DTPA MRI techniques can provide perfusion characteristics of RILI (78). Ogasawara *et al.* investigated the time course of the contrast enhancement in the lungs using Gd-DTPA kinetics between irradiated- and non-irradiated lungs. This study showed altered Gd-DTPA kinetics one-month post irradiation with a single dose of 40 Gy in eight dogs compared to normal lungs due to a perfusion reduction. In this study, dynamic Gd-DTPA MRI was significantly affected by long scan times (~3 minutes) that affect the measurement due to blurring from respiratory motion. Gd-DTPA MRI lung perfusion and volume measurements are difficult to correct for quantitative measurement of perfusion (79). Conventional T_2^* MRI techniques are sensitive to the mobility of water molecules and therefore can assess RILI by monitoring changes in T_2^*decay (80). A prolongation of the T_2^* two-weeks post-irradiation (20 Gy) was observed in *ex vivo* rat lungs (80). Zhang *et al.* have demonstrated in a rabbit model that the apparent diffusion coefficient (ADC) in tumor lesions decreases 1-5 weeks post-irradiation of the lungs (81). However, in that study it was difficult to obtain ADC values from the normal PT due to low SNR and short T_2^* because of air/tissue magnetic susceptibility differences.

1.7.6 Hyperpolarized MRI

Hyperpolarized (Hp) MRI has the ability to assess the anatomical, functional and metabolic changes associated with RILI using ^{3}He, ^{129}Xe, and ^{13}C respectively (3). MR spectroscopic imaging can detect changes due to RILI with intravenous injection of Hp contrast agent labeled with [1-^{13}C] pyruvate (82). Thind *et al.* reported the lactate-to-pyruvate signal ratio (Lac/Pyr) in the irradiated rat lung with a radiation dose of 18.5 Gy was significantly different from the non-irradiated rat lung two-weeks post irradiation (83). The increase in the Lac/Pyr ratio was correlated with changes in macrophages density due to RP measured histologically. The Lac/Pyr measurements were not able to directly measure the anatomical and functional changes due to RP. Additionally, MR spectroscopic imaging using Hp [1-^{13}C] pyruvate was challenging due to low tissue concentration, requiring relatively large voxels.

Hp ^{3}He gas MRI has also been explored to quantify RILI. Hp ^{3}He gas MRI can provide Apparent Diffusion Coefficient (ADC) maps of lungs with high SNR, temporal and spatial resolution. The first study of RILI using a rat model has shown a significant increase in

ADC values of Hp ^{3}He associated with three months-post irradiation dose of 40 Gy (84). Increases in the regional lung ^{3}He ADC values have been associated with fibrosis in patient groups 8-months post-RT (85). Ireland *et al.* investigated the feasibility of detecting the ventilation changes in the lungs between pre- and post-RT using Hp ^{3}He gas (86). In this work, Ireland *et al.* correlated the degree of emphysema in the lungs using CT and Hp ^{3}He MRI in regions of RP three-months post-RT. Although Hp ^{3}He gas, particularly ADC, shows feasibility for detection of fibrosis. Hp ^{3}He gas MRI is restricted to ventilated regions of the lung since ^{3}He has negligible solubility. Furthermore, ^{3}He is an exceedingly rare gas with limited abundance and unlikely to develop into a clinical tool. ^{129}Xe on the other hand is plentiful and has relatively high tissue solubility and chemical shift. Hp ^{129}Xe diffusion-weighted MR imaging has been used to measure changes in lung morphometric parameters associated with RILI, specifically the mean airspace chord length (L_m) in a RILI rat model (87). In this work, Ouriadov *et al.*, measured a decrease in L_m two weeks post-irradiation with a radiation dose of 18 Gy and successfully correlated the changes to histology measurement of mean linear intercept.

1.7.7 Hp ^{129}Xe MR Spectroscopy

In addition to lung ventilation imaging, Hp ^{129}Xe solubility properties allow spectroscopy techniques to be used for the measurement of exchange from the alveolar air space to the PT and RBC compartments (88,89). There are two dissolved phase peaks relative to gas signal in MR spectra as shown in Figure 1.2. The largest peak occurs at -6950 Hz corresponds to Hp ^{129}Xe in the gas phase. The peak at the center of the MR spectrum (0 Hz) (in Figure 1.2) is due to PT which also includes a small and negligible fraction of blood plasma at approximately the same frequency (90). The peak at -520 Hz (19 ppm) is the xenon bound to hemoglobin inside the RBC (91,92). Dissolved phase signal is approximately 2% of the gas signal and saturates in the lungs very rapidly within a gas transfer time range of 50-150 ms. Therefore, the use of small RF excitation (i.e. flip angles) of the gas phase magnetization in the alveolar air pool, allows the dynamics of the dissolved phase signal (i.e. gas exchange curves) to be assessed using subsequent MR spectroscopy acquisitions. This can be done by changing the time delay between data acquisitions. This MR spectroscopy technique is called chemical shift saturation recovery (CSSR) (93,94). Gas transfer dynamics measured from the whole lung using CSSR technique can be translated into assessment of structural and functional information of lung by fitting with numerical gas exchange models (90,95,96).

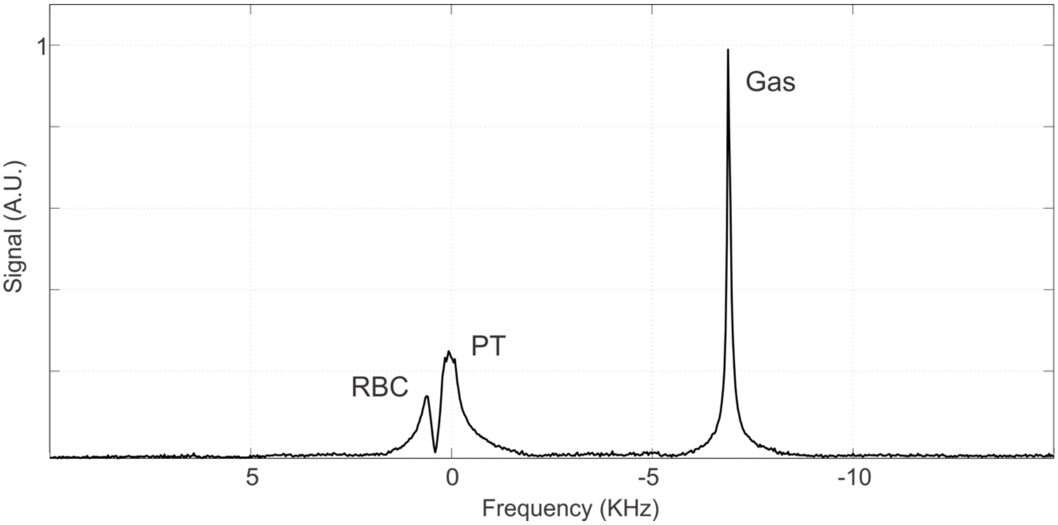

Figure 1.2**:** MR spectrum of rat lungs after inhaling Hp ^{129}Xe using a spectrally selective RF pulse that excites the gas phase with a low flip angle and the dissolved phases with a high flip angle.

Fox *et al.* have investigated early-phase RILI using the CSSR technique (4). In this study, average gas transfer time for PT was observed to be elevated significantly with a whole lung irradiated rat model two weeks following 16 Gy irradiation compared to a control group. In this study, correlation between early-phase RILI changes in whole-lung and RBC gas transfer curve was not significant. This was an unexpected finding as the vascular network is expected to be affected by RILI, and may have been due to the fact whole lung CSSR measurement cannot identify regional changes. Saturation of ^{129}Xe in the RBC compartment is expected to vary regionally and temporally due to perfusion and gas exchange of ^{29}Xe in RBC within the capillary network. Although the Hp ^{129}Xe gas MR spectroscopy CSSR technique provides functional information about the global lung physiology, regional information of the Hp ^{129}Xe gas exchange process is expected to increase the sensitivity for detection of RILI effects when using partial (or conformal) radiotherapy.

1.7.8 Hp ^{129}Xe Dissolved Phase imaging

Imaging the dissolved phases of ^{129}Xe (i.e. PT, RBC) has been explored using three-point Dixon approaches based on Cartesian k-space sampling (97), following a one-point Dixon approach based on radial k-space sampling fashion to address short T_2^* (98). Cleveland *et al.* extended the one-point Dixon approach to include 3D imaging (99). On the other hand, Qing *et al.* also developed a 3D imaging technique using hierarchical IDEAL (Iterative Decomposition of water and fat with Echo Asymmetry and Least-square estimation) reducing the breath-hold time down to approximately 11 s (99,100). However, the dissolved phase imaging techniques have yet to be explored for RILI.

1.8 Principles of MRI

The physical phenomenon called nuclear magnetic resonance (NMR) is concerned with the intrinsic angular momentum (spin) of nuclei that contain unpaired protons or neutron. The nuclei of ^{1}H in water (and fats) serve as the primary source at the signal in MRI since water is highly abundant in the body. The source of the NMR signal originates from the precession of the bulk spin system in the presence of a strong static magnetic field and subsequently excitation of spins by application of an externally applied radiofrequency (RF) field. The NMR signal is spatially localized by MR imaging using spatially-varying magnetic field gradients (i.e. frequency and phase encoding gradients). The type of RF excitation (i.e. the selection of flip angle); timing in regards to acquisition of data, and data acquisition (i.e. k-space) trajectory describe the MR pulse sequence strategy. In this section, basic concepts of MRI are introduced including conventional and Hp MRI relevant to the thesis. Interested readers are referred to Haacke *et al*. and Bernstein *et al*. for more details (101,102).

1.8.1 Magnetic Moment in the Presence of a Magnetic Field

On closer inspection, a nuclear spin, which has a magnetic moment, $\boldsymbol{\mu}$, experiences a torque when an external magnetic field, $\boldsymbol{B_o}$, is applied, resulting in the precession of spins about the direction of the magnetic field. The precession angular frequency, $\boldsymbol{\omega_0}$, is called the Larmor frequency and given by the following equation:

$$\boldsymbol{\omega} = \gamma \ \boldsymbol{B_o} \qquad [1.1]$$

;where γ is the gyromagnetic ratio which is usually expressed as $\gamma/2\pi$ in SI units of MHz/T. The gyromagnetic ratio for ^{129}Xe and ^{1}H are -11.78 MHz/T and 42.58 MHz/T respectively. Thus, the Larmor frequencies for ^{129}Xe and ^{1}H are -35.34 MHz and 127.7 MHz respectively at a field strength of 3T.

1.8.2 Conventional MR Magnetization

Application of an external magnetic field, $\boldsymbol{B_0}$, aligns the spins either parallel or anti-parallel to give a net magnetization of $\boldsymbol{M}$ as shown in Figure 1.3 (a). Conceptually, the conventional MR signal arises from $\boldsymbol{M}$, which aligns along the external magnetic fields as shown in Figure 1.3 (b). Application of an RF pulse, $\boldsymbol{B_1}$, at the Larmor frequency along the *x*-axis will provide a torque that tips $\boldsymbol{M}$ from the *z*-axis to the transverse plane (*xy*-plane) (Figure 1.3 (c)). Therefore, following RF pulse application, $\boldsymbol{M}$ can be decomposed into a longitudinal component $\boldsymbol{M_z}$ and a transverse component $\boldsymbol{M_{xy}}$. $\boldsymbol{M_{xy}}$ precesses at the Larmor frequency while inducing an exponentially decreasing time-varying voltage signal in the receiver RF coil (Figure 1.3 (d)), or Free Induction Decay (FID). The signal received by the RF coil resembles a damped oscillation, governed by an apparent transverse relaxation time (T_2^*). On the other hand, while the transverse magnetization decreases via transverse relaxation, the $\boldsymbol{M_z}$ re-grows via longitudinal relaxation, re-establishing the net magnetization to thermal equilibrium along the *z*-axis.

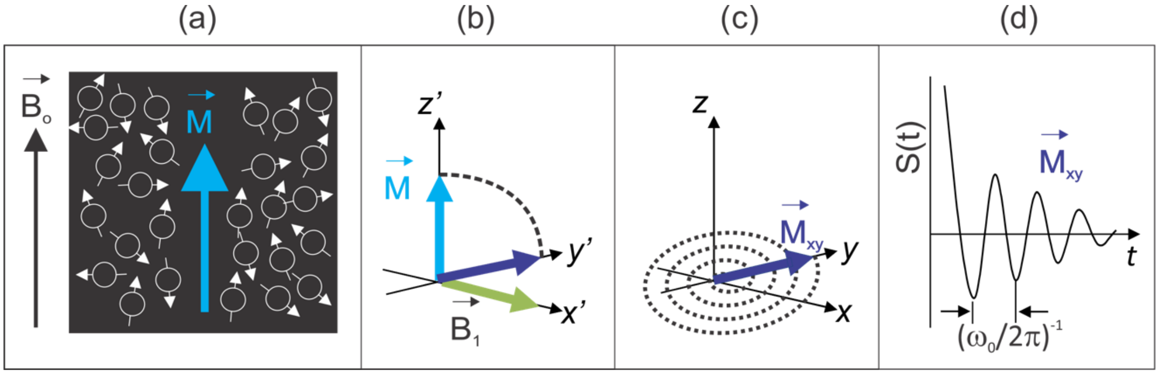

Figure 1.3: (a) Bulk magnetization vector, ***M***, of a spin population in the external magnetic field, $\boldsymbol{B}_o$; (b) Tipping the magnetization from *z'* direction to *xy* plane using an RF pulse, $\boldsymbol{B}_1$, applied in the *x'* direction; (c) Precession of transverse magnetization, $\boldsymbol{M}_{xy}$, in the laboratory frame (d) Time-varying voltage signal induced in the receive coil.

For a spin 1/2 system, magnetization in a spin population arises from two quantum states. In the presence of $\boldsymbol{B_o}$, the nuclear spins split into low energy, $S_{-1/2}$, and high energy, $S_{+1/2}$, states called Zeeman levels. The energy difference between these state is given by:

$$E = -\boldsymbol{\mu} \cdot \boldsymbol{B_o} \qquad [1.2]$$

;where, $\boldsymbol{\mu}$ is the magnetic moment of the spin, $1/2\gamma\hbar$ for the $S_{+1/2}$ and $-1/2\gamma\hbar$ for the $S_{-1/2}$. The number of spins in the $S_{+1/2}$ state which are aligned with $\boldsymbol{B_o}$, contributes to the net magnetization ***M***, and thereby the thermally-polarized signal for conventional MR. Therefore, the longitudinal magnetization M_z is given by:

$$M_Z = P \cdot N \cdot \frac{\gamma\hbar}{2} \qquad [1.3]$$

;where $\hbar$ is the Planck's constant ($\hbar$ = 1.054571800(13)× 10^{-34} (J s)), N is the total number of atoms, and P is the polarization. The magnetization, and thus the NMR signal depends on the polarization levels. The polarization, P, is given by:

$$P = \frac{N^{+} - N^{-}}{N} \qquad [1.4]$$

;where, N^{+} and N^{-} are the number of spins in the high and low Zeeman levels respectively.

Ideally, the condition of $N^{+} >> N^{-}$ corresponds to the highest possible polarization, $P \approx 1$, and therefore provides the highest signal. However, for thermal equilibrium, polarization is very low due to the small difference between the N^{+} and N^{-} states (Figure 1.4 (a)). Therefore, P can be re-written using the Boltzmann distribution as follows:

$$P_{thermal} \approx \frac{1}{2}\left[\frac{N^{+}}{N^{-}} - 1\right] \approx \frac{\gamma \hbar B_{o}}{2kT} \qquad [1.5]$$

;where, k is the Boltzmann constant (k = 8.6173324×10^{-5} (eV K^{-1})), and T is temperature (T=300 K at laboratory temperature). For a magnetic field strength of B_{o} = 3T, the achievable thermal polarization fraction for ^{129}Xe is approximately 2.8×10^{-6}. At room temperatures, the percentage polarization for ^{129}Xe is therefore very small, however this can still detected if there are a large number of ^{129}Xe nuclei within the volume. Therefore, thermally-polarized ^{129}Xe phantoms containing pressurized ^{129}Xe gas are generally used to achieve a measurable thermal MR signal.

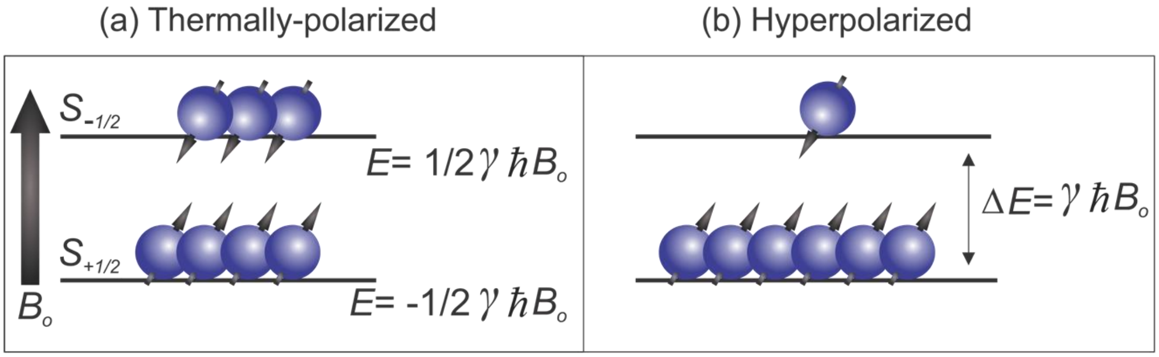

Figure 1.4: Zeeman energy levels at thermal equilibrium (a) and in the hyperpolarized state (b). $S_{-1/2}$ and $S_{+1/2}$ are low and high energy levels.

Substituting Eqn. [1.5] in Eqn. [1.3], the longitudinal magnetization for conventional MR can be re-written as follows:

$$M_z = \frac{N\gamma^2\hbar^2 B_o}{4kT}, \qquad [1.6]$$

Equation [1.6] provides the basis of the MR signal, once factors including relaxation time dependencies, and the RF coil sensitivity are considered. Conceptually, Eqn. [1.6] can also be related to the achievable conventional MR signal (^{1}H) from lung. Since *N* is low in the lungs due to high fraction of air space, the thermally-polarized conventional MR signal is very low. This signal can be artificially improved using hyperpolarized gas techniques as explained in the next section.

1.8.3 Hyperpolarized MR Magnetization

Hyperpolarization is a pre-magnetized form of MR in which the percentage polarization achievable is in a range of 10-40%, typically using a spin-exchange optical pumping (SEOP) polarization approach (103). The population of N^+ nuclei is artificially increased up to a factor of 10^5 compared to thermally polarized ^{129}Xe gas as shown in Figure 1.4 (b). While the initial magnetization is significantly higher, the Hp ^{129}Xe gas differs from conventional MR since the longitudinal magnetization is not renewable and the magnetization depends on the polarization from the SEOP approach. The following sections briefly explain the process of SEOP polarization.

1.8.4 Hyperpolarized ^{129}Xe Gas Production

Hyperpolarization is achieved by the combination of two different stages: (*i*) transfer of the angular momentum from the circularly polarized laser photons to the valence electrons of Rubidium-87 atoms (^{87}Rb) via optical pumping, and (*ii*) transfer of the electron polarization of ^{87}Rb atoms to ^{129}Xe atoms via spin exchange (Fermi-contact hyperfine) interactions (104). This is usually achieved in a continuous flow of ^{87}Rb vapour of a mixture of ^{129}Xe (1-2%) and other buffer gases (usually 97% N_2 and 1-2% ^{3}He) through a polarizer cell containing ^{87}Rb vapor as shown in Figure 1.5 (a) (105,106). The cell is placed in a weak magnetic field (60-70 Gauss) in order to split the valence electrons of ^{87}Rb into different Zeeman energy levels. A circularly polarized laser (σ^+, $\Delta m_j = +1$) with a wavelength of 795nm polarizes the ^{87}Rb valence electrons. The electrons in the $5S_{1/2}$ ($m_j = -1/2$) ground level is excited to the higher energy level $5P_{1/2}$ ($m_j = +1/2$) upon absorption of photons as shown in Figure 1.5 (b). Since the laser light is circularly polarized, the transition only allows jumps from $m_j = -1/2$ to $m_j = +1/2$ levels, which represents azimuthal spin quantum number. The ^{87}Rb electrons de-excite back to the ground state due to either the quenching by N_2 gas or radiatively (life time less than 30 ns). Finally, spin exchange takes place causing a transfer of the spin angular momentum of the ^{87}Rb valence electrons to the ^{129}Xe nucleus as shown Figure 1.5 (c). The achievable ^{129}Xe polarization is given by:

$$P_{Xe} = P_{Rb} \cdot \frac{\gamma_{SE}}{\gamma_{SE} + \Gamma}[1 - \exp(-\tau \cdot (\gamma_{SE} + \Gamma))] \qquad [1.7]$$

;where P_{Rb} is the polarization of ^{87}Rb, γ_{SE} is the spin exchange rate, Γ is the depolarization rate of the ^{129}Xe gas, and τ represents the time required for ^{129}Xe to reach maximum polarization due to the spin exchange interaction between the optically pumped ^{87}Rb and ^{129}Xe within the SEOP cell. The use of high power narrowed laser sources (60-150 W) provides significantly high polarization of ^{87}Rb along the SEOP cell. Maintaining the appropriate cell temperatures in the SEOP cell is one of the main criteria to reduce Γ. However, after extended use, temperature variations and cold spots on the SEOP cell due to the inappropriate thermal management of polarizer cell causes the ^{87}Rb vapour to condense on the cell surface. The ^{87}Rb buildup layer due to the cold spots on the cell diminishes the polarization of the ^{129}Xe gas. Another important limiting factor is the separation of the Hp ^{129}Xe gas from other gas mixtures. After polarization in the SEOP cell, the gas mixture flows into a trap submerged in liquid nitrogen at temperature of ~77 K. Hp ^{129}Xe is frozen and accumulated in the trap for approximately one hour (107). The frozen mixture is sublimated to the gas state for use during experiments. This transition from the frozen state to gas state is the major source polarization loss since the decay of polarization is rapid during the phase transition (on the order of 30-50%). Consequently, 10-40% is the typical level of polarization achievable; however this depends on a number of factors, including laser power, the geometry of the SEOP cell, the thermal management of the SEOP cell, the gas flow and fraction of the gas mixture, and the design of the xenon freeze out trap (108).

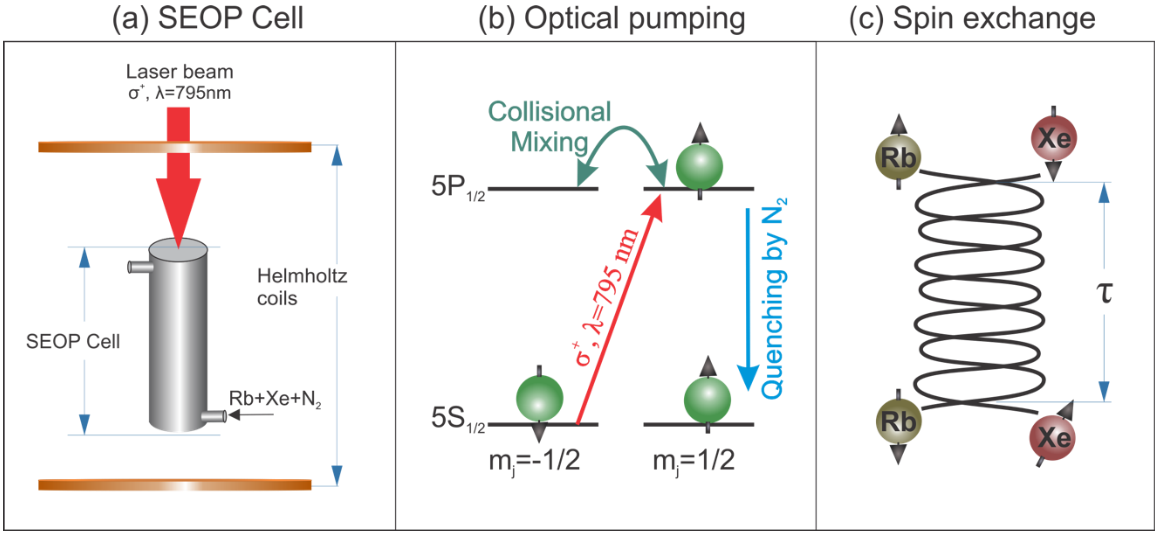

Figure 1.5: (a) SEOP cell is shown including the Helmholtz coils, cell, and circularly polarized (σ^+) laser beam. (b) Optical pumping for polarizing the valence electrons of ^{87}Rb. (c) The spin exchange interactions between the ^{87}Rb and ^{129}Xe. τ is the time required for ^{129}Xe to reach saturation due to the spin exchange interaction.

Substituting Eqn [1.7] in Eqn [1.3], the longitudinal magnetization is given by:

$$M_z = \frac{1}{2} N \cdot \gamma \cdot \hbar \cdot P_{Rb} \cdot \frac{\gamma_{SE}}{\gamma_{SE} + \Gamma} [1 - \exp(-\tau \cdot (\gamma_{SE} + \Gamma))] \qquad [1.8]$$

Another distinguishing feature of Hp MR can be seen by comparing Eqn. [1.8] to Eqn. [1.6]. The hyperpolarized magnetization does not depend on the main magnetic field and is approximately linearly proportional to gyromagnetic ratio of the nuclei. This feature has implications for low field MRI that are not described in this thesis.

1.8.5 Chemical Shift

Although the initial Hp signal strength is independent of the main magnetic field ($\boldsymbol{B_o}$), $\boldsymbol{B_o}$ still plays an important role in Hp ^{129}Xe MRI. The precession frequency of spins depends on B_o as already shown in Eqn [1.1] assuming the $\boldsymbol{B_o}$ is the same for all spins. In reality, the spins in different chemical environments experience different amounts of de-shielding resulting in variations of local $\boldsymbol{B_o}$. The local magnetic field, $\boldsymbol{B_{local}}$, experienced by the nuclear spin is given by:

$$\boldsymbol{B_{local}} = (1- \sigma)\, \boldsymbol{B_o} \qquad [1.9]$$

;where σ is the de-shielding constant that depend on the intrinsic chemical properties of the electron cloud on the nuclei and its environment. Therefore, Eqn. [1.1] can be rewritten as follows:

$$\boldsymbol{\omega} = \gamma\, \boldsymbol{B_{local}} \qquad [1.10]$$

The variation in $\boldsymbol{B_{local}}$ is referred to as the chemical shift of the Larmor frequency. Sufficiently high magnetic field strength permits separation of distinct chemical shifts of ^{129}Xe. The phenomenon of chemical shift is shown in Figure 1.2 from rat lungs at 3T. ^{129}Xe in the PT and RBC compartments experiences a different chemical environment and $\boldsymbol{B_{local}}$. The frequency differences due to the chemical shift between the ^{129}Xe gas and the dissolved ^{129}Xe phases in the PT and RBC compartments are approximately 6950 Hz and 7475 Hz at 3 T respectively.

1.8.6 RF Pulse

The concept of the radiofrequency (RF) magnetic field (***B*1**) was mentioned in section 1.8.2 and Figure 1.3 (c). The application of ***B*1** tips the magnetization vector into the transverse plane by an angle called the flip angle. The flip angle, α, is given by:

$$\alpha = \gamma \int_0^T B_1(\mathrm{t})\,\mathrm{dt} \qquad [1.11]$$

;where T is the pulse duration. A flip angle of 90° will produce the maximum MR signal by tipping all the available magnetization into the transverse plane. Since the Hp magnetization is non-renewable, a second RF pulse would result in no signal. Therefore, to optimize the available magnetization the selection of both the amplitude and duration of RF pulse are equally important. Another important concept is the spatial homogeneity of the applied $\boldsymbol{B}_1$ field. A homogenous $\boldsymbol{B}_1$ can be achieved by using a birdcage RF coil as described in Chapter 2.

RF pulses can be used to excite chemical shifts with different flip angles. The previously described CSSR technique (4) uses a frequency selective rectangular (or 'hard') RF pulse; with a low flip angle applied to the ^{129}Xe gas phase, and a large flip angle applied to the dissolved phases of ^{129}Xe. In RF pulse terminology, a hard pulse has the RF profile shape of a rect function in the time domain. The Fourier transform of a hard pulse leads to an RF profile with a sinc function in the frequency domain. Selective excitation of the gas and dissolved phases of ^{129}Xe can be achieved in the frequency domain with a sinc function. The central lobe of the sinc function provides the necessary high flip angle to the dissolved phase of ^{129}Xe and the side lobes provide the low flip angle excitation to the gas phase of ^{129}Xe.

The RF pulse and magnetic moment are analyzed in a rotating reference frame to simplify the mathematical analysis of the temporal progression of the magnetization. An effective magnetic field is derived to explain the interaction between the $\boldsymbol{B}_1$ and spin system in the rotating frame as follows:

$$\boldsymbol{B}_{\mathrm{eff}} = (B_o - \frac{\boldsymbol{\omega}}{\boldsymbol{\gamma}})\widehat{z'} + B_1\widehat{x'} \qquad [1.12]$$

;where, ω is the carrier frequency of the RF pulse. Thus, the effective magnetic field has two components in the rotating frame. On-resonance ($\omega = \omega_o$), $\boldsymbol{B}_{\mathbf{eff}}$ is in the same direction as $\boldsymbol{B}_{\mathbf{1}}$.

1.8.7 MR Signal

The phenomenological Bloch equations describe the behavior of the magnetization after the application of an RF pulse, including the relaxation terms as follows:

$$\frac{d\boldsymbol{M}}{dt} = \gamma\boldsymbol{M} \times \boldsymbol{B_{eff}} + \frac{1}{T_1}(\boldsymbol{M_o} - \boldsymbol{M_z}) - \frac{1}{T_2^*}\boldsymbol{M_{xy}} \qquad [1.13]$$

The first term in the Bloch equation represents the relationship between the application of the RF pulse and spin system including the off-resonance effects. The second term describes the relaxation of the longitudinal magnetization, characterized by the spin-lattice relaxation time (T_1). The third term describes the relaxation of the transverse magnetization, characterized by the apparent spin-spin relaxation time (T_2^*). The solution to the Bloch equation for thermally polarized signal has been discussed previously (101,102). In particular, the solution to the Bloch equation for Hp ^{129}Xe imaging after the application of an RF pulse of flip angle of α_1 is given by(109) :

$$M_z = M_i \cos(\alpha_1)\ (1- \exp(-t/T_1)) \quad [1.14]$$

$$M_{xy} = M_i \sin(\alpha_1)\ (1- \exp(-t/T_1))\ \exp(-t/T_2^*) \quad [1.15]$$

;where M_i is the initial magnetization that depends on the polarization of the ^{129}Xe gas. T_1 describes the exponential decay of the longitudinal magnetization toward thermal equilibrium. T_1 mechanisms include the interaction with paramagnetic molecules such as diatomic oxygen. However, the effects of T_1 are generally negligible since T_1 is on the order of ~30s for ^{129}Xe gas in the lungs and the MR acquisition is on the orders of a few seconds.

The spin-spin relaxation time (T_2^*) describes the exponential decay of the transverse magnetization. Among other factors, T_2^* depends on the uniformity of B_o, as such the T_2^* for Hp ^{129}Xe in the gas phase and dissolved phases are approximately 6 ms and 2 ms at 3T respectively. Apart from the non-renewable nature of Hp magnetization, M_{xy} and thereby the SNR of dissolved phases of ^{129}Xe strongly depends on T_2^*. To deal with the signal loss due to short T_2^*, the signal is optimally sampled in as short a read-out time as possible using a high flip angle. The selection of the flip angle and optimization of read-out time will be discussed in Chapter 3 in more detail.

1.8.8 RF Coils

As discussed in the previous section 1.8.6, ***B₁*** tips the longitudinal magnetization into the transverse plane initiating the MR signal. While the transverse magnetization is precessing in the *xy* plane, it induces an exponentially decaying voltage signal (i.e. FID) that is used to reconstruct the MR image. An RF coil is used to transmit the excitation RF field, $\boldsymbol{B_{1+}}$, and receive the RF field, $\boldsymbol{B_{1-}}$, radiated by the spin system. To achieve a homogenous flip angle distribution ($\boldsymbol{B_{1+}}$) over the imaging region, RF coils are often designed in shape of cylinder (e.g. birdcage coils). The $\boldsymbol{B_{1+}}$ homogeneity generated by the transmit coil can be derived using the Biot-Savart law for a unit current flowing in the coil elements. A receive coil that is placed close to the object is known as a surface coil which improves the sensitivity. The sensitivity of the receive coils can be determined using the principle of reciprocity, where $\boldsymbol{B_{1-}}$ for a unit current flow, *I*, in the receive coil element is considered to arise from a sample associated with the density of the spin population. The MR signal for a given volume of sample is expressed using the following equation:

$$S(t) = A\,\omega_o \int (B_{1-}(\vec{r})/I)_{xy} \cdot M_{xy}(\vec{r},t)\; dV \qquad [1.16]$$

;where *A* is a constant that depends on coil filling factor, gain, and frequency deviations due to $\boldsymbol{B_o}$ and $\boldsymbol{B_{1+}}$ inhomogeneities. A detailed discussion about optimization of the $\boldsymbol{B_{+}}$ and $\boldsymbol{B_{1-}}$ field and other technical details including the geometry and electrical components of transmit and receive RF coils can be found in the Chapter 2.

1.8.9 Spatial Localization of the MRI Signal

Imaging requires spatial localization of the precession frequencies as a function of position over the imaging region. A precise variation in precession frequencies is achieved by applying linearly changing magnetic field gradients using gradient coils. If the gradient coils are switched on, the net magnetic field is given by:

$$\boldsymbol{B}(x,y,x)= (B_o + G_x x+ G_y y+ G_z z)\hat{z} \qquad [1.17]$$

;where, G_x, G_y, and G_z are the gradient amplitudes produced by the x, y, and z gradient coils respectively. Typically, the maximum gradient amplitude for a clinical scanner is on the order of 50 mT/m. Additionally, the rate by which the achievable gradient amplitude can be obtained, is called the slew rate. Typical clinical values for slew rate are on the order of 200mT/m/ms for a clinical scanner. Both the slew rate and gradient amplitudes are significantly important for establishing the temporal and spatial resolution of MR imaging and will be discussed in detail in Chapter 3.

In this thesis, MR images were acquired in 2D projection fashion. 2D imaging is performed without slice-selection, using a phase encoding gradient applied in y direction and frequency encoding gradient applied in x direction. A hard pulse with a small duration (or large bandwidth) was used to excite the whole lung as a single slab in the z direction. Neglecting relaxation and off-resonance effects, the acquired 2D MR data is given by:

$$s(k_x, k_y) = \iint m(x, y)\exp(-i2\pi(xk_x + yk_y))dxdy \qquad [1.18]$$

;where $m(x, y)$ is the magnetization in the voxel in the imaging plane corresponding to the spin density, k_x and k_y are the location in the k-space along the frequency and phase encoding directions respectively. A 2D image is computed from the inverse Fourier transform ($\Im^{-1}$) of the data in k-space as:

$$m(x, y) = \Im^{-1}\{s(k_x, k_y)\} = \iint s(k_x, k_y)\exp(i2\pi(xk_x + yk_y))dk_x dk_y \qquad [1.19]$$

The sampled k-space points define the scan trajectory. The geometry of the scan trajectory has a first-order impact on the quality of the reconstructed image. The selection of optimum k-space trajectories must consider the trade-off between the signal dynamics and SNR considering the gradient performance of the imaging system. Procedures for sampling of k-space data and resulting SNR and resolution are investigated in Chapter 3 using a point spread function (PSF) analysis as shown in Figure 1.6. Briefly, calculation of the PSF allows for quantitative evaluation of image blurring, through the full-width at half maximum (FWHM), and SNR for a corresponding read-out time (T_{read}), field-of-view (FOV) and imaging matrix.

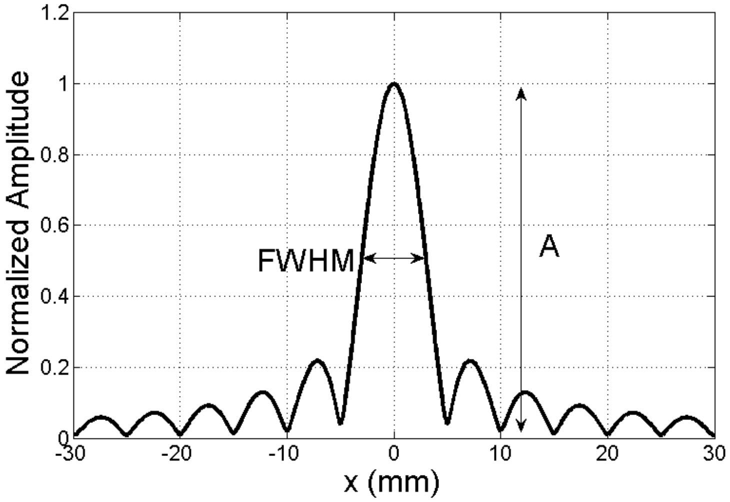

Figure 1.6: Full width at half-maximum (FWHM) and amplitude of a point spread function.

1.8.10 1D Gradient Echo

Gradient Echo is a common frequency encoding method and considered a 1D MR signal, which encodes spatial information in the FID signal by frequency encoding. A 1D MR gradient echo signal is accomplished by applying a magnetic field gradient during the FID signal. This gradient spatially encodes the FID signal by first de-phasing (with a negative gradient lobe) and re-phasing the transverse magnetization signal (with a positive polarity gradient) as shown in Figure 1.7. As already mentioned in the previous section, the transverse magnetization is produced after an RF pulse application. Following the RF pulse, the application of the negative lobe of the G_x gradient causes a very fast de-phasing of the FID signal. Then, the positive lobe of the G_x gradient reverses the FID signal known as re-focusing, thereby creating an ‘echo’ at the echo time (TE) Consequently, the associated FID (or 1D k-space) data consists of a range of frequencies along the frequency-encoding gradient direction. This can be translated to 2D k-space data using an additional phase encoding gradient as explained in the next section.

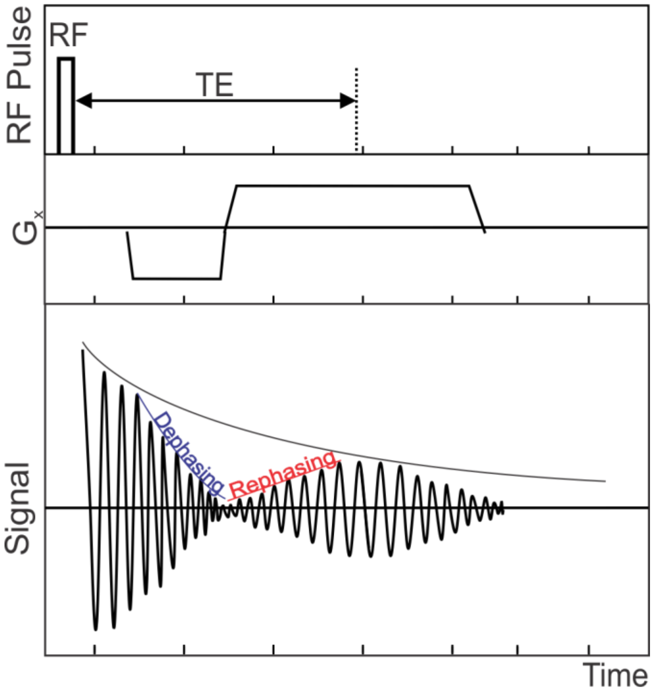

Figure 1.7: 1D gradient echo timing diagram. Transverse magnetization signal re-phasing and de-phasing is shown for the 1D frequency encoding process. *TE* is the echo time.

1.8.11 2D Cartesian k-space Sampling

Cartesian sampling (i.e. uniform grid) is the conventional way MR data is sampled in k-space. Fast gradient recalled echo (FGRE) imaging is the most commonly used pulse sequence based on Cartesian k-space sampling as shown in

Figure 1.8. A single line of k-space along the frequency encoding (G_x) direction is acquired after each RF excitation. The phase encoding gradient (G_y) and another RF pulses are than repeated to cover the next line of k-space in the y direction. The pulse repetition time (TR) is the time duration between the RF pulse applications between k-space lines. For 2D proton FGRE imaging, TR is often set to a value greater than 4 × T_1 for maximum signal

intensity. Thus, the total scan time for a 32 × 32 matrix size would be 32 × 4 × T_1, resulting in a long scan time (128× T_1 = 128 s for T_1= 1 s). Faster imaging is possible with Hp ^{129}Xe gas imaging since the time for recovery of the magnetization is not needed. Higher temporal resolution is achieved for Hp imaging: approximately 32 × TR with TR on the order of 10-20 ms. Thus the total scan time for Hp imaging is approximately 300 ms.

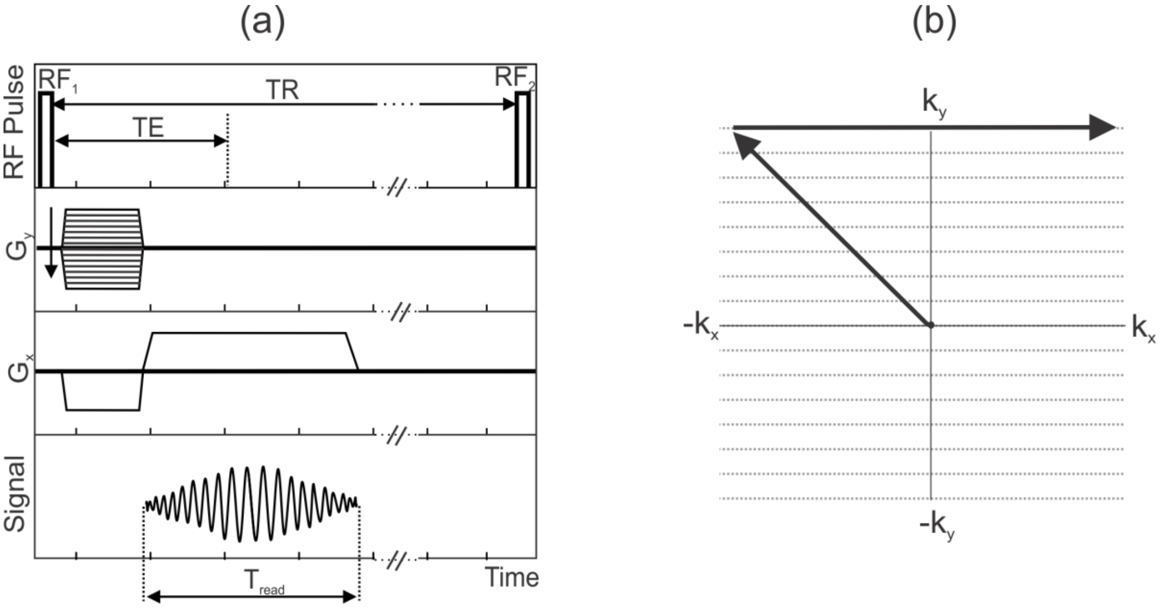

Figure 1.8: 2D Gradient echo pulse sequence timing diagram (a) and Cartesian k-space sampling trajectory (b). *TR* represents the pulse repetition time. *TE* is the echo time. G_x and G_y represent the frequency and phase encoding gradients respectively.

A representative coronal rat lung FGRE image obtained using 64 RF pulses is shown in Figure 1.9. The high number of RF pulse is a limitation for Hp imaging due to the non-renewable nature of hyperpolarized imaging. To deal with the problem of using a high number of RF pulses, each acquisition along the frequency encoding direction uses a small flip angle (α = ~10°). Alternatively, more efficient k-space trajectories (e.g. spiral) can substantially reduce the number of RF pulses, allowing for higher flip angles and hence increasing SNR. Additionally, faster k-space acquisition also allow for capturing of the gas exchange of ^{129}Xe.

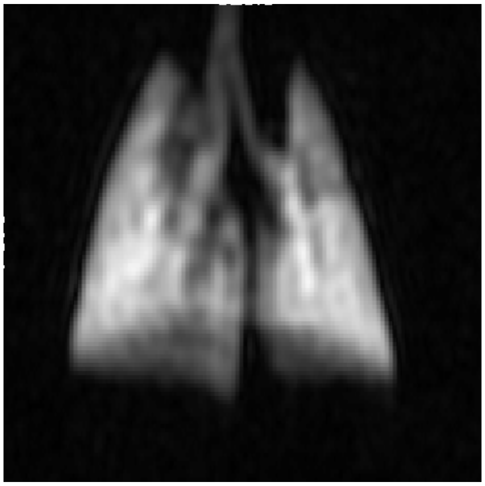

Figure 1.9: Coronal 2D MR FGRE gas phase image of *in vivo* rat lung. Acquisition parameters include: 64 × 64 matrix size, and 6 cm FOV.

1.8.12 Spiral k-space Sampling

An efficient approach for mapping the entire k-space following an RF excitation utilizes a single-shot spiral acquisition. Single-shot spiral is based on acquiring the k-space data in a spiral pattern using gradients (G_x and G_y) applied as an increasing sinusoidal function of time as shown in

Figure 1.10. The duration of the data acquisition window is called the read-out time, T_{read}. The selection of T_{read} on the order of T_2^* (~2 ms) is desirable for increasing SNR and reducing blurring artifacts. Short T_{read} is usually performed using high gradient amplitudes and slew rates. However, high gradient power can cause image artifacts including Eddy

current induced k-space distortions and time delay errors arising from gradient hardware for long T_{read}. Fortunately, these image artifacts can be corrected using k-space trajectory measurement methods (110). The single-shot k-space sampling provides a better tool for imaging pulmonary functions including perfusion and gas diffusion imaging (111,112). Additionally, *TR* values can be used to create functional images for detection of gas exchange dynamics. The build-up of dissolved ^{129}Xe signal between sequential images can be controlled by changing the TR values taking advantage of rapid single-shot imaging with short TE. Furthermore, obtaining TR-weighted rapid single-shot spiral images of PT, RBC and gas compartments separately can be achieved using advanced pulse sequence approaches such as Iterative Decomposition of water and fat with Echo Asymmetric and Least-squares estimation (IDEAL) described next.

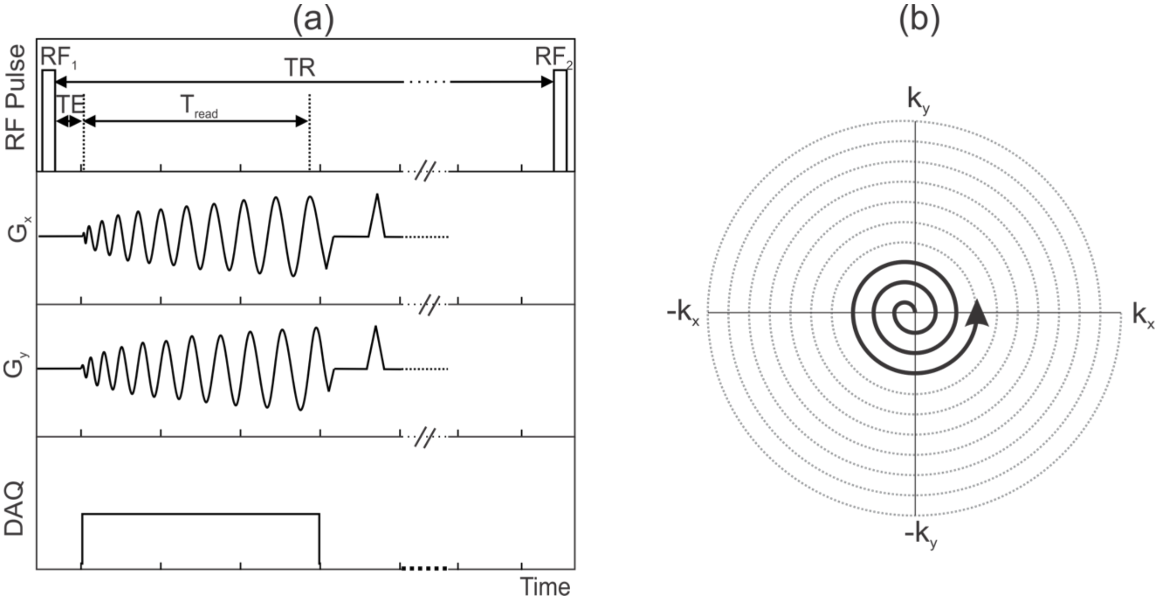

Figure 1.10: Single-shot spiral pulse sequence timing diagram, including the RF pulse, gradient and read-out window (a) and the spiral k-space sampling trajectory (b).

1.8.13 IDEAL Approach for Imaging Chemical Species

IDEAL is a Dixon-based imaging method commonly used to exploit the difference in chemical shifts between fat and water to separately image fat and water in conventional proton MRI (113). The three-point Dixon method is based on acquisition of three consecutive images with a phase difference of 0, π, 2π. The phase differences are achieved by selecting echo times based on the chemical shift between fat and water. Three echo images are acquired to estimate the B_o inhomogeneity, water and fat compartments (114,115). On closer inspection, the complex fat/water MR signal strength after Fourier transformation for a voxel at a chosen *TE* value can be expressed as follows:

$$S(TE_n) = [W + F\exp(i\Delta w_{FW} TE_n)]\exp(i\gamma\Delta B_o TE_n) \qquad [1.20]$$

;where, *W* and *F* are water and fat fraction respectively, and Δw_{FW} is the chemical shift difference between the fat and water. For each voxel, the signal is a mixture of signals from the fat and water as a function of echo time (*TE*). Because the chemical shift is known and *TE* is controlled by the timing of the data acquisition, the corresponding signal strength equations for each image can be simplified as follows:

$$S(TE_n) = [W + F \cdot C(TE_n)]H(TE_n) \qquad [1.21]$$

;where $C(TE_n)$ is a constant which depends on TE and $H(TE_n)$ is the B_o inhomogeneity factor. This equation contains three unknown contributions from *F, W* and $H(TE_n)$. Therefore, acquisition of three echo images with different echo shifts allows separation of these three unknowns to purposely-separate fat and water. Since the chemical shift depends on the B_o inhomogeneity, three-point Dixon method correct for the effect of B_o inhomogeneity. However, selection of echo shift with a phase difference of π causes image artifact, reducing the accuracy of three-point Dixon for separating the water and fat (113). Imperfect selection of echo shifts can result in inaccurate calculation of the fraction of water to fat within each voxel. IDEAL combines asymmetrically acquired echoes with an iterative least-squares decomposition algorithm to maximize noise performance and address the dependence of water/fat separation on echo shift. Asymmetrically acquired echoes helps to reduce the scan times for substances with large chemical shift. For example, to obtain a phase difference of π between compartments with small chemical shift (~10 ppm) requires a long echo time spacing (~340 ms) but large chemical shifts (~200 ppm) require a much shorter echo time spacing (50 ms). The iterative least-squares decomposition part of IDEAL stands for estimation of the fraction of each chemical shift compartments iteratively in multi steps (116). Additional improvement for estimation of fat/water decomposition has been achieved using phase difference of 2π /3 by analyzing the noise performance (113). The noise performance of the a water/fat separation has been shown to be proportional to the SNR performance of the pulse sequence which is estimated based on the effective number of signal averages (NSA) (117). NSA for three point Dixon is given by:

$$NSA = \frac{2(1-\cos\theta)^2}{1+2\cos^2\theta} \qquad [1.22]$$

;where θ is the phase encoding increment. Thus the maximum SNR can be achieved for NSA = 3 at θ of 2π /3 for three-point IDEAL. Therefore, the selection of echo times can be optimized using the NSA approach.

Optimization of NSA and other imaging parameters for IDEAL imaging will be discussed in detail in Chapter 3. To achieve the measurement of the gas exchange curves for PT and RBC compartments separately in this thesis, IDEAL is used in spiral k-space sampling fashion following a single RF pulse application. Four-point IDEAL is used to produce gas, PT and RBC images by varying *TR* which controls the build-up of the dissolved phase ^{129}Xe signal. Thereby, gas exchange curves have been calculated from the variation in the image intensity as a function of *TR*.

1.8.14 Gas Exchange Models of Hyperpolarized ^{129}Xe

Gas exchange curves represent the diffusion of ^{129}Xe from gas phase to the PT compartment and from the PT to the RBC compartment as a function of time respectively. A representative gas exchange curve is shown in Figure 1.11(a). The concentration of ^{129}Xe in each of the compartments is proportional to the build-up ^{129}Xe signal which is usually obtained from whole lungs using the CSSR technique (89). Gas exchange curves are usually analyzed by fitting CSSR experimental data points by the Mansson exponential function (95). In this study, the IDEAL imaging technique is used to obtain gas exchange curves, which have been fitted by the Mansson's gas exchange model to explore lung function regionally. The gas exchange curves provide information about the concentration of ^{129}Xe gas that diffuses from alveolar air space into the PT and RBC compartments. As a function of time the concentration of ^{129}Xe build-up in PT compartment increases exponentially giving rise to MR image intensity within approximately 100 ms (Figure 1.11 (a)). The linear slope after 100 ms corresponds to the linear slope (S_1) due to the saturation of ^{129}Xe concentration in the PT compartment. The dynamics of ^{129}Xe transfer from alveolar air space to the PT compartment is modelled using one-dimensional diffusion equations. The diffusion from the PT to RBC is also included in the blood perfusion with a constant flow as shown by the red color in Figure 1.11 (b).

The exponential fitting function from the Mansson model is given as follows:

$$S(TR) = S_o(1 - \exp(TR/\tau)) + S_1 TR \qquad [1.23]$$

;where, S_o is the y-intercept of the linear slope, τ, is the exponential gas transfer time constant corresponding to the fast exponential increase in the dissolved phase concentration due to the diffusion and S_1 is the linear slope corresponding to the accumulation of ^{129}Xe concentration after fast diffusion. S_o, S_1, and τ are subsequently used to calculate the average pulmonary tissue thickness, L_{PT}, and capillary thickness, L_C. Detailed information about the mathematical derivation can be found in Mansson *et al*. (95). Additionally, the relative blood volume, V_{RBC}, can be calculated by $L_C/(L_C + L_{PT})$.

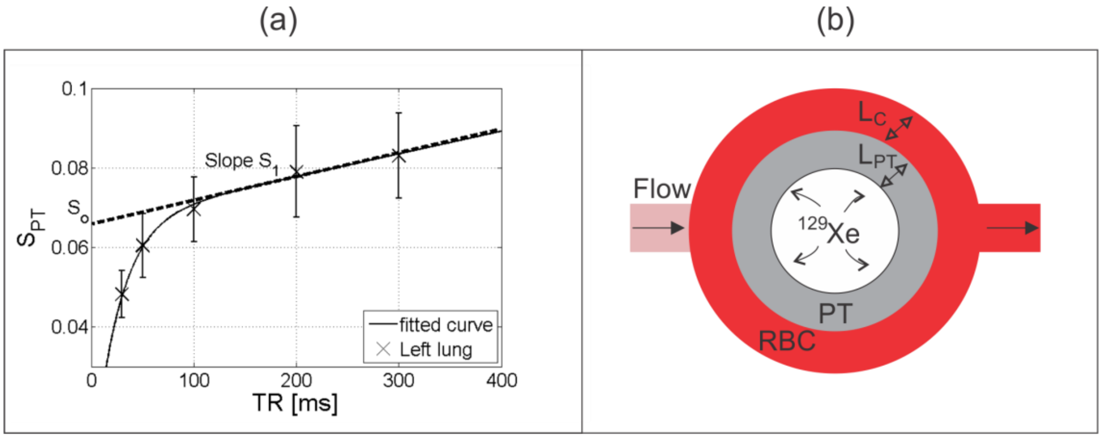

Figure 1.11: (a) A representative gas exchange curve is obtained by fitting experimental data points by the Mansson exponential function Eqn. [1.23]. S_o is the y-intercept of the linear slope, S_1 is the linear slope, *TR* represents the pulse repetition time. (b) Geometry of the Mansson's gas exchange model is shown. L_{PT} and L_C are the pulmonary tissue thickness and capillary thickness, respectively.

1.9 Thesis Hypothesis and Objectives

The hypothesis of this research is that hyperpolarized ^{129}Xe MRI will provide measurement of gas exchange changes, specifically L_{PT} and V_{RBC}, in an early-phase rat model of RILI which will correlate with histology. To address this hypothesis, new Hp ^{129}Xe approaches are required to increase signal-to-noise ratio (SNR), especially from the dissolved phases of ^{129}Xe in the PT and RBC compartments. The first specific goal of thesis was to increase the SNR of dissolved phase ^{129}Xe images by developing a Transmit-Only / Receive-Only (TO/RO) RF coil. The second specific goal was to develop an MRI technique with sufficient temporal and spatial resolution for quantification of the regional changes in the dynamics of the ^{129}Xe gas exchange in the RBC and PT compartments. Therefore, a 2D IDEAL MRI pulse sequence using single-shot spiral k-space sampling was optimized and implemented for simultaneous Hp ^{129}Xe imaging of gas, PT, and RBC compartments. Finally, the regional gas exchange abnormalities in a rat model of RILI associated with partial thorax irradiation was investigated and correlated with histology measurements.

1.10 Thesis Outline

Chapter 2 describes the design and construction of a novel TO/RO RF coil for rat imaging. Chapter 2 is a reproduction of the accepted manuscript by *Concepts in Magnetic Resonance Part B: Magnetic Resonance Engineering* 2014 (DOI: 10.1002/cmr.b.21288). The coil sensitivity was optimized through numerical simulations. Performance of the new TO/RO coil was investigated using a thermally-polarized phantom and *in vivo* experiments.

Chapter 3 describes the development and optimization of a novel imaging technique (IDEAL with spiral k-space sampling) that provides regional quantification of the dynamics of the gas exchange. Chapter 3 is a reproduction of the accepted manuscript by *Magnetic Resonance in Medicine* 2015, Manuscript ID: MRM-15-16025. A theoretical analysis was performed to optimize the spiral k-space read-out time, echo time, flip angles, spatial resolution and required gradient slew rate and amplitude respectively. The feasibility of imaging the ^{129}Xe gas, PT and RBC, and measuring the dynamics of the gas exchange was investigated *in vivo* in healthy rat lungs.

Chapter 4 is a reproduction of a submitted manuscript to *Medical Physics* 2015. Chapter 4 investigates the feasibility of detecting early RP in a rat model of RILI involving right lung irradiation 2-weeks post-irradiation. Taking advantages of developments made in Chapter 2 and 3, the gas exchange curves were measured separately for PT and RBC compartments for the left and right lungs. Average PT thickness, (L_{PT}) and RBC relative volumes (V_{RBC}) were measured from the left and right lungs separately. The average PT and RBC volumes were statistically compared between the irradiated and non-irradiated cohorts.

Chapter 5 includes a summary of discussion of the thesis, including the contribution of this work to the detection of RILI in its early stage. Additionally, future work is discussed including further improvements in polarization, modeling of gas exchange, and MR pulse sequence design for transition to clinical imaging.

1.11 References

1. Canadian Cancer Statistics 2014. Volume Toronto, ON. http://www.cancer.ca/statistics: Canadian Cancer Society, Statistics Canada, Public Health Agency of Canada, Provincial/Territorial Cancer Registries 2014. p. http://www.cancer.ca/~/media/cancer.ca/CW/cancer%20information/cancer%20101/Canadian%20120cancer%20120statistics/Canadian-Cancer-Statistics-22014-EN.pdf.

2. Gilad S, Lithwick-Yanai G, Barshack I, et al. Classification of the Four Main Types of Lung Cancer Using a MicroRNA-Based Diagnostic Assay. J Mol Diagn 2012;14(5):510-517.

3. Santyr G, Fox M, Thind K, et al. Anatomical, functional and metabolic imaging of radiation-induced lung injury using hyperpolarized MRI. Nmr Biomed 2014;27(12):1515-1524.

4. Fox MS, Ouriadov A, Thind K, et al. Detection of radiation induced lung injury in rats using dynamic hyperpolarized Xe-129 magnetic resonance spectroscopy. Med Phys 2014;41(7).

5. Schwartzstein RM, Parker MJ. Respiratory Physiology: A Clinical Approach: Lippincott Williams & Wilkins: 2006.

6. Krinke GJ, Bullock GR, Bunton T. The Laboratory Rat: Elsevier Science: 2000.

7. Angus GE, Thurlbeck WM. Number of alveoli in the human lung. J Appl Physiol 1972;32(4):483-485.

8. Ochs M, Nyengaard JR, Jung A, et al. The number of alveoli in the human lung. Am J Respir Crit Care Med 2004;169(1):120-124.

9. Weibel ER. What makes a good lung? The morphometric basis of lung function. Swiss Med Wkly 2009;139(27-28):375-386.

10. International Agency for Research in Cancer S, B. W., Wild, C. P. World Cancer Report 2014. Read IARC Press 2014. p. 630.

11. Torre LA, Bray F, Siegel RL, Ferlay J, Lortet-Tieulent J, Jemal A. Global cancer statistics, 2012. CA Cancer J Clin 2015;65(2):87-108.

12. Jemal A, Bray F, Center MM, Ferlay J, Ward E, Forman D. Global cancer statistics. CA Cancer J Clin 2011;61(2):69-90.

13. Canadian Cancer Statistics 2015. Volume Toronto, ON. http://www.cancer.ca/statistics: Canadian Cancer Society, Statistics Canada, Public

Health Agency of Canada, Provincial/Territorial Cancer Registries 2015. p. https://www.cancer.ca/~/media/cancer.ca/CW/cancer%20information/cancer%20101/Canadian%20120cancer%20120statistics/Canadian-Cancer-Statistics-22015-EN.pdf.

14. Ontario Lung Association. S, P., Stiff, D., Briante, C., Ahmad, S., Ler, A., Wong, L. Life and Economic Burden of Lung Disease in Ontario: 2011 to 2041. RiskAnalytica, on behalf of the Ontario Lung Association, 2011. Your Lungs, Your Life: Insights and Solutions to Lung Health in Ontario. http://www.on.lung.ca/yourlungsyourlife: the Ontario Lung Association; 2012. p. 1-24.

15. Peters S, Adjei AA, Gridelli C, et al. Metastatic non-small-cell lung cancer (NSCLC): ESMO Clinical Practice Guidelines for diagnosis, treatment and follow-up. Ann Oncol 2012;23 Suppl 7:vii56-64.

16. Sher T, Dy GK, Adjei AA. Small cell lung cancer. Mayo Clin Proc 2008;83(3):355-367.

17. Goldstraw P, Crowley J, Chanksy K, et al. The IASLC lung cancer staging project: Proposals for the revision of the TNM stage groupings in the forthcoming (Seventh) edition of the TNM classification of malignant tumors (vol 8, pg 706-714, 2007). Journal of Thoracic Oncology 2007;2(10):985-985.

18. Edge S, Byrd DR, Compton CC, Fritz AG, Greene FL, Trotti A. AJCC Cancer Staging Manual. New York: Springer-Verlag: 2010.

19. Goldstraw P, Ball D, Jett JR, et al. Non-small-cell lung cancer. Lancet 2011;378(9804):1727-1740.

20. Group NM-AC. Chemotherapy in addition to supportive care improves survival in advanced non-small-cell lung cancer: a systematic review and meta-analysis of individual patient data from 16 randomized controlled trials. J Clin Oncol 2008;26(28):4617-4625.

21. Kelly K, Crowley J, Bunn PA, Jr., et al. Randomized phase III trial of paclitaxel plus carboplatin versus vinorelbine plus cisplatin in the treatment of patients with advanced non--small-cell lung cancer: a Southwest Oncology Group trial. J Clin Oncol 2001;19(13):3210-3218.

22. Soria JC, Mauguen A, Reck M, et al. Systematic review and meta-analysis of randomised, phase II/III trials adding bevacizumab to platinum-based chemotherapy as first-line treatment in patients with advanced non-small-cell lung cancer. Annals of Oncology 2013;24(1):20-30.

23. Burdett S, Rydzewska LHM, Tierney JF, et al. Preoperative chemotherapy for non-small-cell lung cancer: a systematic review and meta-analysis of individual participant data. Lancet 2014;383(9928):1561-1571.

24. Peters S, Adjei AA. LUNG CANCER How much platinum-based chemotherapy is enough in NSCLC? Nat Rev Clin Oncol 2015;12(1):8-9.

25. Shepherd FA, Rodrigues Pereira J, Ciuleanu T, et al. Erlotinib in previously treated non-small-cell lung cancer. N Engl J Med 2005;353(2):123-132.

26. Bradbury PA, Tu D, Seymour L, et al. Economic analysis: randomized placebo-controlled clinical trial of erlotinib in advanced non-small cell lung cancer. J Natl Cancer Inst 2010;102(5):298-306.

27. Herbst RS, Fukuoka M, Baselga J. Gefitinib--a novel targeted approach to treating cancer. Nat Rev Cancer 2004;4(12):956-965.

28. Rosell R, Carcereny E, Gervais R, et al. Erlotinib versus standard chemotherapy as first-line treatment for European patients with advanced EGFR mutation-positive non-small-cell lung cancer (EURTAC): a multicentre, open-label, randomised phase 3 trial. Lancet Oncol 2012;13(3):239-246.

29. Kantarjian HM, Wolff RA, Koller CA. The MD Anderson Manual of Medical Oncology, Second Edition: McGraw-Hill Education: 2011.

30. Handy JR, Asaph JW, Skokan L, et al. What happens to patients undergoing lung cancer surgery? Outcomes and quality of life before and after surgery. Chest 2002;122(1):21-30.

31. Datta D, Lahiri B. Preoperative evaluation of patients undergoing lung resection surgery. Chest 2003;123(6):2096-2103.

32. Auperin A, Le Chevalier T, Le Pechoux C, et al. Adjuvant chemotherapy, with or without postoperative radiotherapy, in operable non-small-cell lung cancer: two meta-analyses of individual patient data. Lancet 2010;375(9722):1267-1277.

33. Robinson CG, Patel AP, Bradley JD, et al. Postoperative Radiotherapy for Pathologic N2 Non-Small-Cell Lung Cancer Treated With Adjuvant Chemotherapy: A Review of the National Cancer Data Base. J Clin Oncol 2015;33(8):870.

34. Delaney G, Barton M, Jacob S, Jalaludin B. A model for decision making for the use of radiotherapy in lung cancer. Lancet Oncol 2003;4(2):120-128.

35. Tyldesley S, Boyd C, Schulze K, Walker H, Mackillop WJ. Estimating the need for radiotherapy for lung cancer: An evidence-based, epidemiologic approach. Int J Radiat Oncol 2001;49(4):973-985.

36. Reck M, Popat S, Reinmuth N, et al. Metastatic non-small-cell lung cancer (NSCLC): ESMO Clinical Practice Guidelines for diagnosis, treatment and follow-up. Ann Oncol 2014;25 Suppl 3:iii27-39.

37. Fairchild A, Harris K, Barnes E, et al. Palliative thoracic radiotherapy for lung cancer: a systematic review. J Clin Oncol 2008;26(24):4001-4011.

38. Koshy M, Goloubeva O, Suntharalingam M. Impact of Neoadjuvant Radiation on Survival in Stage Iii Non-Small-Cell Lung Cancer. Int J Radiat Oncol 2011;79(5):1388-1394.

39. Brock J, Ashley S, Bedford J, Nioutsikou E, Partridge M, Brada M. Review of hypofractionated small volume radiotherapy for early-stage non-small cell lung cancer. Clin Oncol (R Coll Radiol) 2008;20(9):666-676.

40. Timmerman R, Paulus R, Galvin J, et al. Stereotactic body radiation therapy for inoperable early stage lung cancer. JAMA 2010;303(11):1070-1076.

41. Iyengar P, Kavanagh BD, Wardak Z, et al. Phase II trial of stereotactic body radiation therapy combined with erlotinib for patients with limited but progressive metastatic non-small-cell lung cancer. J Clin Oncol 2014;32(34):3824-3830.

42. Hurkmans CW, Cuijpers JP, Lagerwaard FJ, et al. Recommendations for implementing stereotactic radiotherapy in peripheral stage IA non-small cell lung cancer: report from the Quality Assurance Working Party of the randomised phase III ROSEL study. Radiat Oncol 2009;4:1.

43. Ghafoori P, Marks LB, Vujaskovic Z, Kelsey CR. Radiation-induced lung injury. Assessment, management, and prevention. Oncology (Williston Park) 2008;22(1):37-47; discussion 52-33.

44. Yarnold J, Brotons MC. Pathogenetic mechanisms in radiation fibrosis. Radiotherapy and oncology 2010;97(1):149-161.

45. Palma DA, Senan S, Tsujino K, et al. Predicting Symptomatic Radiation Pneumonitis after Concurrent Chemoradiotherapy for Non-Small Cell Lung Cancer: Results of an International Individual Patient Data Meta-analysis. Journal of Thoracic Oncology 2012;7(9):S267-S267.

46. Rodrigues G, Lock M, D'Souza D, Yu E, Van Dyk J. Prediction of radiation pneumonitis by dose - volume histogram parameters in lung cancer--a systematic review. Radiotherapy and oncology 2004;71(2):127-138.

47. Ueki N, Matsuo Y, Togashi Y, et al. Impact of pretreatment interstitial lung disease on radiation pneumonitis and survival after stereotactic body radiation therapy for lung cancer. J Thorac Oncol 2015;10(1):116-125.

48. Yamashita H, Takahashi W, Haga A, Nakagawa K. Radiation pneumonitis after stereotactic radiation therapy for lung cancer. World J Radiol 2014;6(9):708-715.

49. Marks LB, Yu X, Vujaskovic Z, Small W, Jr., Folz R, Anscher MS. Radiation-induced lung injury. Semin Radiat Oncol 2003;13(3):333-345.

50. Citrin D, Cotrim AP, Hyodo F, Baum BJ, Krishna MC, Mitchell JB. Radioprotectors and Mitigators of Radiation-Induced Normal Tissue Injury. Oncologist 2010;15(4):360-371.

51. Dang J, Li G, Zang S, Zhang S, Yao L. Risk and predictors for early radiation pneumonitis in patients with stage III non-small cell lung cancer treated with concurrent or sequential chemoradiotherapy. Radiat Oncol 2014;9:172.

52. Miller MR, Hankinson J, Brusasco V, et al. Standardisation of spirometry. Eur Respir J 2005;26(2):319-338.

53. Marks LB, Munley MT, Spencer DP, et al. Quantification of radiation-induced regional lung injury with perfusion imaging. International journal of radiation oncology, biology, physics 1997;38(2):399-409.

54. Gergel TJ, Leichman L, Nava HR, et al. Effect of concurrent radiation therapy and chemotherapy on pulmonary function in patients with esophageal cancer: dose-volume histogram analysis. Cancer J 2002;8(6):451-460.

55. Curran WJ, Jr., Moldofsky PJ, Solin LJ. Observations on the predictive value of perfusion lung scans on post-irradiation pulmonary function among 210 patients with bronchogenic carcinoma. International journal of radiation oncology, biology, physics 1992;24(1):31-36.

56. Choi NC, Kanarek DJ. Toxicity of thoracic radiotherapy on pulmonary function in lung cancer. Lung Cancer 1994;10 Suppl 1:S219-230.

57. Rabe KF, Hurd S, Anzueto A, et al. Global strategy for the diagnosis, management, and prevention of chronic obstructive pulmonary disease: GOLD executive summary. Am J Respir Crit Care Med 2007;176(6):532-555.

58. Movsas B, Raffin TA, Epstein AH, Link CJ, Jr. Pulmonary radiation injury. Chest 1997;111(4):1061-1076.

59. Palma DA, de Koste JRV, Verbakel WFAR, Senan S. A new approach to quantifying lung damage after stereotactic body radiation therapy. Acta Oncologica 2011;50(4):509-517.

60. Konstas AA, Goldmakher GV, Lee TY, Lev MH. Theoretic basis and technical implementations of CT perfusion in acute ischemic stroke, part 2: technical implementations. AJNR Am J Neuroradiol 2009;30(5):885-892.

61. Konstas AA, Goldmakher GV, Lee TY, Lev MH. Theoretic basis and technical implementations of CT perfusion in acute ischemic stroke, part 1: Theoretic basis. AJNR Am J Neuroradiol 2009;30(4):662-668.

62. Hu XY, Fang XM, Chen HW, et al. Early detection of acute radiation-induced lung injury with multi-section CT perfusion imaging: An initial experience. Clin Radiol 2014;69(8):853-860.

63. Tahamtan R, Shabestani Monfared A, Tahamtani Y, et al. Radioprotective effect of melatonin on radiation-induced lung injury and lipid peroxidation in rats. Cell J 2015;17(1):111-120.

64. Serin M, Gulbas H, Gurses I, Erkal HS, Yucel N. The histopathological evaluation of the effectiveness of melatonin as a protectant against acute lung injury induced by radiation therapy in a rat model. International Journal of Radiation Biology 2007;83(3):187-193.

65. Woel RT, Munley MT, Hollis D, et al. The time course of radiation therapy-induced reductions in regional perfusion: a prospective study with >5 years of follow-up. International journal of radiation oncology, biology, physics 2002;52(1):58-67.

66. Mah K, Van Dyk J, Keane T, Poon PY. Acute radiation-induced pulmonary damage: a clinical study on the response to fractionated radiation therapy. International journal of radiation oncology, biology, physics 1987;13(2):179-188.

67. Damen EM, Muller SH, Boersma LJ, de Boer RW, Lebesque JV. Quantifying local lung perfusion and ventilation using correlated SPECT and CT data. Journal of nuclear medicine 1994;35(5):784-792.

68. Bajc M, Neilly B, Miniati M, Mortensen J, Jonson B. Methodology for ventilation/perfusion SPECT. Semin Nucl Med 2010;40(6):415-425.

69. Petersson J, Sanchez-Crespo A, Larsson SA, Mure M. Physiological imaging of the lung: single-photon-emission computed tomography (SPECT). Journal of applied physiology 2007;102(1):468-476.

70. Hoover DA, Reid RH, Wong E, et al. SPECT-based functional lung imaging for the prediction of radiation pneumonitis: a clinical and dosimetric correlation. J Med Imaging Radiat Oncol 2014;58(2):214-222.

71. Petersson J, Sanchez-Crespo A, Rohdin M, et al. Physiological evaluation of a new quantitative SPECT method measuring regional ventilation and perfusion. Journal of applied physiology 2004;96(3):1127-1136.

72. Ishimori T, Saga T, Nagata Y, et al. 18F-FDG and 11C-methionine PET for evaluation of treatment response of lung cancer after stereotactic radiotherapy. Ann Nucl Med 2004;18(8):669-674.

73. Hart JP, McCurdy MR, Ezhil M, et al. Radiation pneumonitis: correlation of toxicity with pulmonary metabolic radiation response. International journal of radiation oncology, biology, physics 2008;71(4):967-971.

74. McCurdy MR, Castillo R, Martinez J, et al. [18F]-FDG uptake dose-response correlates with radiation pneumonitis in lung cancer patients. Radiotherapy and oncology 2012;104(1):52-57.

75. Moon DH, Maddahi J, Silverman DH, Glaspy JA, Phelps ME, Hoh CK. Accuracy of whole-body fluorine-18-FDG PET for the detection of recurrent or metastatic breast carcinoma. Journal of nuclear medicine 1998;39(3):431-435.

76. Hicks RJ, Mac Manus MP, Matthews JP, et al. Early FDG-PET imaging after radical radiotherapy for non-small-cell lung cancer: inflammatory changes in normal tissues correlate with tumor response and do not confound therapeutic response evaluation. International journal of radiation oncology, biology, physics 2004;60(2):412-418.

77. Siva S, Callahan J, Kron T, et al. A prospective observational study of Gallium-68 ventilation and perfusion PET/CT during and after radiotherapy in patients with non-small cell lung cancer. BMC Cancer 2014;14:740.

78. Ogasawara N, Suga K, Karino Y, Matsunaga N. Perfusion characteristics of radiation-injured lung on Gd-DTPA-enhanced dynamic magnetic resonance imaging. Invest Radiol 2002;37(8):448-457.

79. Hatabu H, Tadamura E, Levin DL, et al. Quantitative assessment of pulmonary perfusion with dynamic contrast-enhanced MRI. Magnet Reson Med 1999;42(6):1033-1038.

80. Shioya S, Tsuji C, Kurita D, et al. Early damage to lung tissue after irradiation detected by the magnetic resonance T2 relaxation time. Radiat Res 1997;148(4):359-364.

81. Zhang Q, Zhang M, Liu Z, et al. Role of MR-DWI and MR-PWI in the radiotherapy of implanted pulmonary VX-2 carcinoma in rabbits. Chin J Cancer Res 2014;26(5):532-542.

82. Thind K, Chen A, Friesen-Waldner L, et al. Detection of radiation-induced lung injury using hyperpolarized C-13 magnetic resonance spectroscopy and imaging. Magnet Reson Med 2013;70(3):601-609.

83. Thind K, Jensen MD, Hegarty E, et al. Mapping metabolic changes associated with early Radiation Induced Lung Injury post conformal radiotherapy using hyperpolarized (13)C-pyruvate Magnetic Resonance Spectroscopic Imaging. Radiotherapy and oncology 2014;110(2):317-322.

84. Ward ER, Hedlund LW, Kurylo WC, et al. Proton and hyperpolarized helium magnetic resonance imaging of radiation-induced lung injury in rats. International journal of radiation oncology, biology, physics 2004;58(5):1562-1569.

85. Mathew L, Gaede S, Wheatley A, Etemad-Rezai R, Rodrigues GB, Parraga G. Detection of longitudinal lung structural and functional changes after diagnosis of radiation-induced lung injury using hyperpolarized He-3 magnetic resonance imaging. Med Phys 2010;37(1):22-31.

86. Ireland RH, Din OS, Swinscoe JA, et al. Detection of radiation-induced lung injury in non-small cell lung cancer patients using hyperpolarized helium-3 magnetic resonance imaging. Radiotherapy and oncology : journal of the European Society for Therapeutic Radiology and Oncology 2010;97(2):244-248.

87. Ouriadov A, Fox M, Hegarty E, Parraga G, Wong E, Santyr EG. Early Stage Radiation-Induced Lung Injury Detected Using Hyperpolarized 129Xe Morphometry: Proof-of-Concept Demonstration in a Rat Model. Mag Reson Med 2015;in press.

88. Stewart NJ, Leung G, Norquay G, et al. Experimental validation of the hyperpolarized Xe chemical shift saturation recovery technique in healthy volunteers and subjects with interstitial lung disease. Mag Reson Med 2014.

89. Ruppert K, Altes TA, Mata JF, Ruset IC, Hersman FW, Mugler JP, 3rd. Detecting pulmonary capillary blood pulsations using hyperpolarized xenon-129 chemical shift saturation recovery (CSSR) MR spectroscopy. Mag Reson Med 2015.

90. Chang YV. MOXE: a model of gas exchange for hyperpolarized 129Xe magnetic resonance of the lung. Mag Reson Med 2013;69(3):884-890.

91. Mugler JP, 3rd, Driehuys B, Brookeman JR, et al. MR imaging and spectroscopy using hyperpolarized 129Xe gas: preliminary human results. Magn Reson Med 1997;37(6):809-815.

92. Wolber J, Cherubini A, Leach MO, Bifone A. Hyperpolarized Xe-129 NMR as a probe for blood oxygenation. Magnet Reson Med 2000;43(4):491-496.

93. Patz S, Hersman FW, Muradian I, et al. Hyperpolarized (129)Xe MRI: a viable functional lung imaging modality? Eur J Radiol 2007;64(3):335-344.

94. Patz S, Muradian I, Hrovat MI, et al. Human pulmonary imaging and spectroscopy with hyperpolarized 129Xe at 0.2T. Acad Radiol 2008;15(6):713-727.

95. Mansson S, Wolber J, Driehuys B, Wollmer P, Golman K. Characterization of diffusing capacity and perfusion of the rat lung in a lipopolysaccaride disease model using hyperpolarized Xe-129. Mag Reson Med 2003;50(6):1170-1179.

96. Patz S, Muradyan I, Hrovat MI, et al. Diffusion of hyperpolarized Xe-129 in the lung: a simplified model of Xe-129 septal uptake and experimental results. New J Phys 2011;13.

97. Muradian I, Patz S, Butler JP, et al. Hyperpolarized 129Xe human pulmonary gas exchange with 3-point Dixon technique. Proceedings of the 14th Annual Meeting of ISMRM 2006;Seattle(Washington):abstract 1297.

98. Driehuys B, Cofer GP, Pollaro J, Mackel JB, Hedlund LW, Johnson GA. Imaging alveolar-capillary gas transfer using hyperpolarized Xe-129 MRI. Proceedings of the National Academy of Sciences of the United States of America 2006;103(48):18278-18283.

99. Cleveland ZI, Virgincar RS, Qi Y, Robertson SH, Degan S, Driehuys B. 3D MRI of impaired hyperpolarized 129Xe uptake in a rat model of pulmonary fibrosis. Nmr Biomed 2014;27(12):1502-1514.

100. Qing K, Ruppert K, Jiang Y, et al. Regional mapping of gas uptake by blood and tissue in the human lung using hyperpolarized xenon-129 MRI. J Magn Reson Imaging 2014;39(2):346-359.

101. Haacke EM, Brown RW, Thompson MR, Venkatesan R. Magnetic Resonance Imaging: Physical Principles and Sequence Design: Wiley: 1999.

102. Bernstein MA, King KF, Zhou XJ. Handbook of MRI Pulse Sequences: Elsevier Science: 2004.

103. Walker TG, Happer W. Spin-exchange optical pumping of noble-gas nuclei. Reviews of Modern Physics 1997;69(2):629-642.

104. Driehuys B, Cates GD, Miron E, Sauer K, Walter DK, Happer W. High-volume production of laser-polarized Xe-129. Appl Phys Lett 1996;69(12):1668-1670.

105. Bauer C, Raich H, Jeschke G, Blumler P. Design of a permanent magnet with a mechanical sweep suitable for variable-temperature continuous-wave and pulsed EPR spectroscopy. Journal of magnetic resonance 2009;198(2):222-227.

106. Chann B, Nelson IA, Anderson LW, Driehuys B, Walker TG. Xe-129-Xe molecular spin relaxation. Physical Review Letters 2002;88(11).

107. Ruset IC, Ketel S, Hersman FW. Optical pumping system design for large production of hyperpolarized. Phys Rev Lett 2006;96(5):053002.

108. Hersman FW, Ruset IC, Ketel S, et al. Large production system for hyperpolarized 129Xe for human lung imaging studies. Acad Radiol 2008;15(6):683-692.

109. Zhao L, Mulkern R, Tseng CH, et al. Gradient-Echo Imaging Considerations for Hyperpolarized 129Xe MR. Journal of magnetic resonance Series B 1996;113(2):179-183.

110. Tan H, Meyer CH. Estimation of k-space trajectories in spiral MRI. Mag Reson Med 2009;61(6):1396-1404.

111. Viallon M, Berthezene Y, Callot V, et al. Dynamic imaging of hyperpolarized He-3 distribution in rat lungs using interleaved-spiral scans. Nmr Biomed 2000;13(4):207-213.

112. Mayer D, Yen YF, Takahashi A, et al. Dynamic and High-Resolution Metabolic Imaging of Hyperpolarized [1-C-13]-Pyruvate in the Rat Brain Using a High-Performance Gradient Insert. Magn Reson Med 2011;65(5):1228-1233.

113. Reeder SB, Pineda AR, Wen Z, et al. Iterative decomposition of water and fat with echo asymmetry and least-squares estimation (IDEAL): application with fast spin-echo imaging. Magn Reson Med 2005;54(3):636-644.

114. Dixon WT. Simple proton spectroscopic imaging. Radiology 1984;153(1):189-194.

115. Hardy PA, Hinks RS, Tkach JA. Separation of fat and water in fast spin-echo MR imaging with the three-point Dixon technique. J Magn Reson Imaging 1995;5(2):181-185.

116. Reeder SB, Wen Z, Yu H, et al. Multicoil Dixon chemical species separation with an iterative least-squares estimation method. Magn Reson Med 2004;51(1):35-45.

117. Glover GH. Multipoint Dixon technique for water and fat proton and susceptibility imaging. J Magn Reson Imaging 1991;1(5):521-530.

Chapter 2 : RF Coil Configuration for Hyperpolarized ^{129}Xe

This chapter is adapted from the published paper: Doganay O, Thind K, Wade T, Ouriadov A, Santyr GE. Transmit-Only/Receive-Only Radiofrequency Coil Configuration for Hyperpolarized ^{129}Xe MRI of Rat Lungs. *Concepts Magn Reson*. doi:10.1002/cmr.b.21288

2.1 Introduction

Hyperpolarized ^{129}Xe is a useful inhaled contrast agent for Magnetic Resonance Imaging (MRI) of the lung air space and promises to provide unique functional information due to its solubility and significant chemical shift (200 ppm) when dissolved in lung tissues (1). In particular, MRI of the gas and dissolved phases of ^{129}Xe can be used to quantify the rate of transfer of xenon between the air space and the lung tissue and the red blood cells (RBC), providing regional information about pulmonary gas exchange (2). Hyperpolarized ^{129}Xe MRI has been useful for development of biomarkers in rodent (i.e. rat and mouse) models of lung injury and disease, including emphysema (3,4). Rodent models provide a powerful approach for modeling of lung diseases and developing new therapeutic targets (5), but the tools are only beginning to be established.

Imaging of ^{129}Xe dissolved in lung tissues is challenging due to modest solubility and relatively low tissue density in the lung, resulting in a relatively low signal, which is approximately two percent of the hyperpolarized ^{129}Xe gas signal (6-8). Furthermore, lung volumes in rats are typically small (~ 5 to 10 mL) (9), requiring sensitive radiofrequency (RF) receiver coils for detection. Another important consideration is that hyperpolarized

MRI benefits by the use of accurate flip angles (i.e. transmit $\mathbf{B}_{1+}$ field) delivered uniformly over the imaging volume, particularly to exploit variable flip angle approaches which make most efficient use of the non-renewable magnetization (10,11). Hyperpolarized ^{129}Xe MRI of the rat lung therefore would benefit from an RF coil configuration which combines high sensitivity in receive mode with a uniform transmit field ($\mathbf{B}_{1+}$) over the entire lung volume. RF sensitivity can be improved by using a surface coil to maximize sensitivity ($\mathbf{B}_{1-}$) over a smaller region of interest (12-14). However, when using this same coil to transmit, surface coil sensitivity decreases with increasing distance from the coil elements leading to an inhomogeneous $\mathbf{B}_{1+}$ field (15,16). A potential solution to this problem, is to use a surface coil for receive and a birdcage transmit coil for transmission of the RF pulse, the latter providing a homogeneous transmit field across the lungs. Such transmit-only/receive-only (TO/RO) coil configurations have been demonstrated for clinical hyperpolarized ^{129}Xe and ^{3}He gas MRI of human lungs (17-19). Additionally, the use of TO/RO coil configurations has been motivated by the desire to improve SNR or reduce image acquisition time as previously shown for other nuclei including ^{13}C (20) and ^{23}Na (21) for small animal imaging.

Despite the significant interest in hyperpolarized ^{129}Xe MR imaging of rat lungs, the literature mostly describes the use of birdcage transmit/receive (T/R) volume coils (9,22), with little attention to TO/RO approaches. A custom-made TO/RO coil configuration was developed for hyperpolarized ^{129}Xe imaging of rat lungs at low field (0.07T) and optimized by reducing the noise using Litz wire and geometric de-coupling between saddle-shaped transmit coils and multi-turn saddle-shaped receive coils (23,24). Another TO/RO design has been proposed at high field based on the use of two volumetric birdcage coils for imaging of dissolved phase hyperpolarized ^{129}Xe in rat brain (25). In this study, we present a novel RF transmit-only/receive-only (TO/RO) coil configuration providing excellent transmit uniformity as well as high SNR for hyperpolarized ^{129}Xe MR lung imaging of rat lungs at 3T (35.34 MHz). Transmission is accomplished by a birdcage coil with uniform $\mathbf{B}_{1+}$ field uniformity and reception is performed by a closely-coupled saddle-shaped surface coil conforming to the rat lung and accommodating ventilation, surgical access and drug delivery. SNR and $\mathbf{B}_{1-}$ uniformity improvement of the TO/RO coil configuration compared to a commercially-made transmit/receive (T/R) birdcage volume coil are demonstrated theoretically and verified experimentally in ^{129}Xe gas phantoms.

2.2 Methods

A TO/RO coil configuration was designed and constructed consisting of three components: (i) a high-pass birdcage transmit coil that produced a homogeneous $\mathbf{B}_{1+}$ magnetic field which could also be used in T/R mode, (ii) a saddle-shaped receive-only surface coil that couples closely to the rat lung, (iii) a fast switching circuit and RF shielding as shown in Figure 2.1 (a). Switching between transmit and receive modes was achieved as previously described (20). Briefly, a fast MOSFET switch circuit was gated using the DC (5 V) component of the transmit signal from the MRI system. Since the gate threshold voltage of the MOSFET circuit (FDP8030L, Fairchild corp., California, USA) was 2V, the 5 V bias was more than adequate to switch between the transmit and receive modes. On transmit, the MOSFET switch circuit was DC biased, and a fast switch power supply (U8002A, Agilent Technologies, Malaysia) provided a 5V DC bias to activate PIN diodes in order to switch on the transmit coil and de-tune the receive coil using a de-tuning circuit. On receive (no MOSFET bias), the receive coil was returned to resonance (35.34 MHz) and the transmit coil was deactivated through the use of PIN diodes (um9415, Microsemi corp., Watertown, MA), located in each rung element. DC bias from the constant current power supply to the PIN diodes passed through two chokes (Axial RF choke 3.9 µH, Bourns Inc., Riverside, CA) to isolate the high frequency noise of the power supply as shown in a simplified circuit diagram in Figure 2.1 (b).

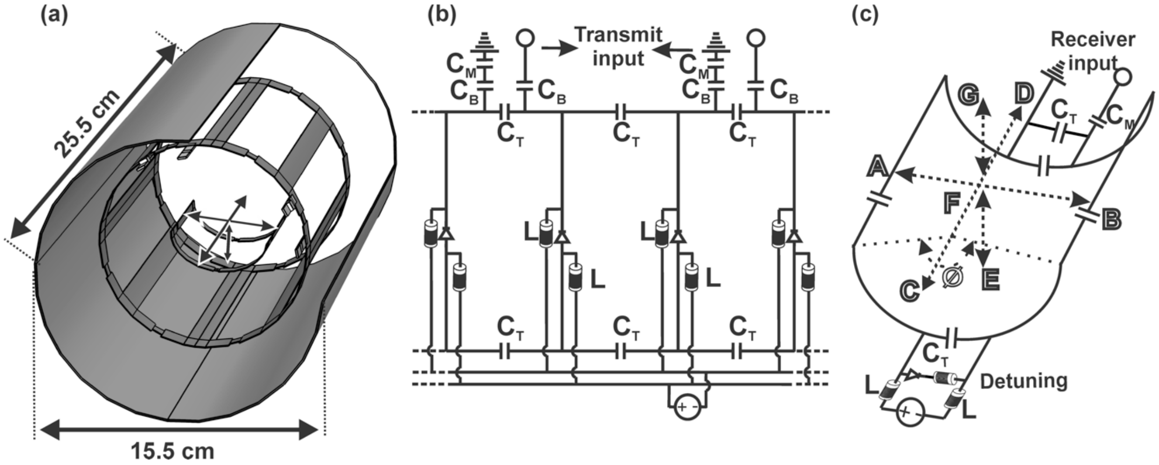

Figure 2.1: Schematic view of the TO/RO configuration (a) consisting of: (i) high-pass birdcage transmit coil, comprised of two end-rings of 12 cm diameter and eight rungs with a length of 16.5 cm each, (ii) saddle-shaped surface coil, and (iii) RF shielding. Tuning capacitors are placed in the end-rings. Simplified circuit diagram of transmit coil (b). CB denotes blocking capacitor to block DC component of the transmit signal, C_M and C_T are tuning and matching capacitors, respectively. Simplified circuit diagram of saddle-shaped, receive surface coil (c). U denotes the aperture angle. The distance from points A to B is 55 mm, from C to D is 60 mm and from E to F is 23 mm.

For comparison purposes, the transmit birdcage coil dimensions were chosen to be similar to a commercially-made rat T/R birdcage coil (Morris Instruments, Ottawa, Canada) with a similar RF shield for both coil configurations. The constructed birdcage transmit coil consisted of two end-rings of 120 mm diameter and eight rungs with a length of 165 mm. The tuning capacitor, $C_T \approx 400$ pFa (100B11160FT500X, American Technical Ceramics corp, Jacksonville, FL) values were roughly estimated using a birdcage builder program (Birdcage Builder Version 1.0 Software, Penn State Hershey Medical Center, Hershey, PA). A network analyzer (Agilent E5061B, Agilent, Santa Clara, CA) and a pickup coil were used to measure the resonance properties of each rung separately, as well as the entire transmit coil. Fine tuning was done by adding smaller (a few pF) capacitors until each rung resonated exactly at 35.34 MHz. The Smith chart on the network analyzer was used to perform impedance matching to a 50 ± 2 ohm transmission line, and S-parameters after the coil was loaded with 300 mL 50 mM NaCl solution (26). The Q factor values were measured from the S_{12} response curve at the -3dB level from the TO/RO coil in both transmit and receive modes and compared to the commercial T/R coil (26-28). Two pick up coils, each with diameter of 3cm were placed 4cm away from either side of the RF coils. Loading factors factor (*Lf*) were calculated within measurement uncertainty of ±10% as previously described (23,27).

A saddle-shaped, receive-only surface coil was designed and constructed around a half cylinder acrylic tube with a diameter of 55 mm as shown in Figure 2.1 (c). Based on measurements of the rat lung and thorax anatomy (diameter and length), fixed lengths of 60 mm (points C to D in Figure 2.1 (c)) and 55 mm (points A to B in Figure 2.1 (c)) were chosen to conform to the rat lungs. The aperture angle, Φ, of the saddle coil was optimized through numerical simulations to maximize SNR and $\mathbf{B}_{1-}$ uniformity across the lungs (from point A to B in Figure 2.1 (a)) as described in the next section. The coil was built from 5 mm-wide copper foil and attached to the acrylic tube with adhesive. Tuning was accomplished using capacitors connected in series as shown in the simplified circuit diagram in Figure 2.1 (c). The receive coil was actively de-tuned during transmission using the same DC bias used to de-couple the transmit coil on receive. A capacitance circuit was used for fine-tuning and matching when the coil was loaded with a rat.

The mechanical ventilation of the rat lungs has been described previously (29,30). A large surgical incision area was required across the neck for intubating the trachea and to secure the intubation catheter. The choice of a saddle-shaped surface coil was determined based on accommodating ventilation, surgical access and drug delivery. Due to the complexity of acquiring forced-ventilation hyperpolarized ^{129}Xe MRI (i.e. dislocation of the catheter, localization of the rat lungs, bleeding), imaging of the rat in the supine position using a saddle-shaped RF coil provides the necessary access to the surgical area during extensive imaging time.

2.2.1 Numerical Modeling

SNR improvement was achieved by maximizing the $\mathbf{B}_{1-}$ magnetic field for a unit current flow through the receiving coil and computing sensitivity maps, according to the reciprocity theorem. In order to estimate the sensitivity maps, the $\mathbf{B}_{1-}$ magnetic field was computed by solving the Biot-Savart equation in 3D using finite element modeling (Comsol Multiphysics, COMSOL 4.2a) for both the T/R (shown in Figure 2.3 (a)) and TO/RO geometries shown in Figure 2.1 (a). The model geometries including birdcage coil, receive coil and shielding were meshed using a free tetrahedral mesh with a minimum element size of 0.01 mm. The shielding was modelled as a magnetic shielding boundary condition with the relative permeability of 7000 and thickness of 1 mm (based on shielding material). Rungs and rings were modeled corresponding to copper foil's electrical properties. The model was solved in the magnetic field interface under the AC/DC branch (31). Next, sensitivity maps were calculated by normalizing $\mathbf{B_{1-}}$ by the surface area of each receiver coil in order to: (i) compare coil performances and (ii) calculate the image uniformity. A percentage uniformity, U, was calculated from simulations and axial images for both coil configurations for four identical circular regions-of-interest (ROIs) to approximate the coverage of the lungs as shown in Figure 2.4(b) (32). The percentage uniformity was calculated for each ROI as:

$$U = 100 \times (1- [(S_{max} - S_{min}) / (S_{max}+S_{min})]) \qquad [2.1]$$

;where S_{max} and S_{min} are the maximum and minimum signal intensities within the ROI.

Considering that the rat lung occupies a volume at the center of the transmit coil with dimensions of 4cm x 4cm x 4cm, the geometry of the saddle-shaped coil was optimized for a body weight up to 400 g (33). $\mathbf{B_{1-}}$ field profiles from point A to B, C to D and E to F were investigated as a function of aperture angle (Φ). The total sensitivity was quantified as a function of aperture angle using of the area under simulated $\mathbf{B_{1-}}$ field profiles from point A to B as shown in Figure 2.2 (b). The SNR was expected to be proportional to the area under the sensitivity profiles as shown in Figure 2.2 (c) for the same RF shielding and the phantom. The noise variations including conductivity, radiation, and sample inductive loses, for each aperture angle was considered by scaling the area under the sensitivity profiles to the coil surface area (34). Finally, the uniformity was maximized to determine the best aperture angle.

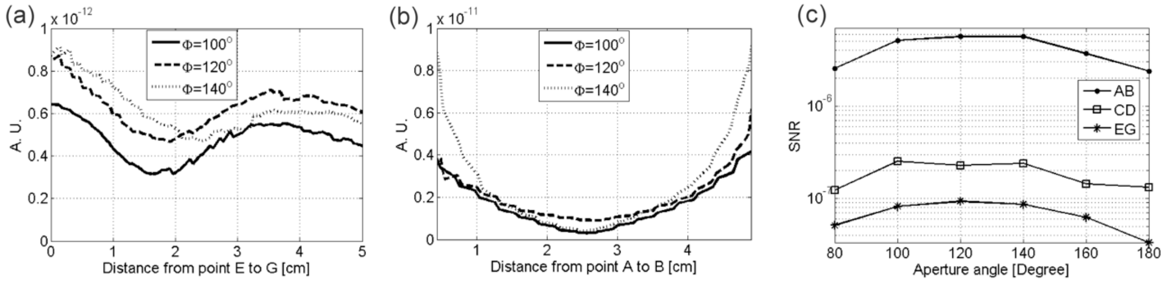

Figure 2.2: Plot of theoretical B_{1-} (a) from point E to G (in Figure 2.1), and (b) from point A to B (in Figure 2.1) for the receive coil at aperture angles of 100°, 120°, and 140°, respectively. Plot of the area under the simulated B_{1-} field profiles from point A to B as a function of aperture angle (b). The SNR profile from A to B, from C to D, and from E to G as a function of aperture angle in log scale (c).

2.2.2 Experimental measurements

A thermally-polarized ^{129}Xe gas phantom was used to compare the signal-to-noise ratios of the TO/RO coil configuration and the T/R coil since the signal from thermal phantom did not depend on differences in polarization and relaxation time effects between measurements. The thermally-polarized phantom consisted of a glass cylinder of length 52 mm and diameter 35 mm, with a volume of approximately 50 ml. The glass phantom was filled with 200 ml of ^{129}Xe gas (80% enriched) and 200 ml O_2 gas (to reduce T_1 relaxation time down to ~1 s) at room temperature in order to provide a measurable ^{129}Xe gas phase axial image. 2D projection images of the thermally-polarized phantom in the axial view were obtained for both coil configurations at 3T (MR750, GEHC) using a 2D fast gradient-recalled echo (FGRE) pulse sequence (TR = 4.0 s, TE = 6 ms, FOV = 10 cm × 10 cm, matrix of 64 × 64, BW = 2.0 kHz, number of averages = 16, flip angle = 90 ± 1 degrees).

A free induction decay (FID) was used to find the 90° flip angle by adjusting the transmit gain to achieve a maximum signal. Image SNR was calculated using the dual acquisition technique (35). The mean value of a circular region of interest (15 pixel diameter) covering most of the axial image was divided by the standard deviation from the same ROI with in within a subtraction image. A B_{1+} map was obtained from the TO/RO coil using the thermally-polarized phantom and a non-inverted double angle Look-Locker (niDALL) technique with nominal flip angles of $\alpha_1 = 60\pm1^o$ and $\alpha_2 = 2\alpha_1$ sequence (TR = 5.0 s, FOV = 8 cm × 8 cm, matrix of 32 × 32, BW = 2.0 kHz, number of averages = 8) (36-38).

For uniformity measurements, a 2D fast gradient-recalled echo sequence (FGRE) pulse sequence implementing a variable flip angle (39) used to acquire projection images of a hyperpolarized ^{129}Xe gas phantom in the axial view for both coil configurations (TR = 100 ms, TE = 4 ms, FOV = 10 cm × 10 cm, matrix of 64 × 64, BW = 5.0 kHz). The hyperpolarized ^{129}Xe gas phantom consisted of a 125 mL plastic bottle (2401-0250 Wash bottles, Thermo Scientific Nalgene, Rochester, NY) of diameter 55 mm filled with hyperpolarized, naturally-abundant ^{129}Xe gas (polarized to approximately 5%) using a home-built polarizer described previously (11).

Imaging of a healthy Sprague Dawley rat (380 g, Charles River Laboratories, Saint-Constant, Canada) was performed using a MRI-compatible mechanical ventilator (GE Healthcare, Malmo, Sweden) for delivery of Hp ^{129}Xe to the lung following an animal care protocol approved by the Animal Care and Veterinary Service of Western University (30). 2D projection MR images were obtained from the same rat in the supine position following five breaths of Hp ^{129}Xe. The FGRE pulse sequence parameters were as follows: TR = 20 ms, TE = 4 ms, FOV = 7 cm × 7 cm, matrix of 48 × 48, BW = 4.0 kHz. Coronal images were repeated six times in intervals of two minutes. A fresh bag of Hp ^{129}Xe was used for each coil within 15 minutes following the preparation of polarized gas to ensure that the polarization (approximately 5%) was the same for each coil.

2.3 Results

The electrical properties of the TO/RO in both transmit and receive modes and the commercial T/R birdcage coils using the network analyzer with a span of 5 MHz are shown in Table **2.1**. The reflected power, S_{11}, measurements showed that the variations in resonance frequencies for both transmit and receive modes (loaded) were less than 20 kHz at the MR scanner (3 T) for the TO/RO coil. The loading factors were 0.27 and 0.24 for the TO/RO in receive mode and transmit mode respectively. For comparison, the loading factor for the commercial T/R birdcage coil was 0.23. Isolation between quadrature channels, S_{12}, was measured to be greater than 20 dB for the phantom and rat loading. This indicates that there is adequate decoupling between quadrature channels in transmit. To minimize the coupling between birdcage coil and saddle-shaped receive coil for the TO/RO configuration, the resonance frequency for the saddle-shaped surface coil was detuned to 5 MHz away from the resonance frequency of transmit coil during the transmit mode.

Table 2.1: Network analyzer measurement of the electrical properties of the TO/RO coil in receive mode and transmit mode respectively and the commercial T/R birdcage coil configurations.

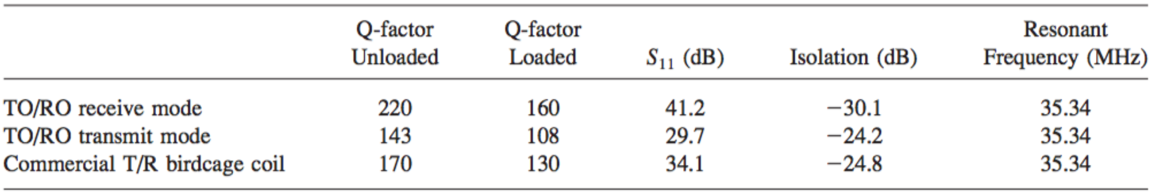

	Q-factor Unloaded	Q-factor Loaded	S_{11} (dB)	Isolation (dB)	Resonant Frequency (MHz)
TO/RO receive mode	220	160	41.2	−30.1	35.34
TO/RO transmit mode	143	108	29.7	−24.2	35.34
Commercial T/R birdcage coil	170	130	34.1	−24.8	35.34

The effect of varying the aperture angle, Φ, on the simulated uniformity of the saddle coil is shown in Figure 2.2 (a) and (b) where $\mathbf{B}_{1-}$ field profiles from point A to B and E to G are compared for different aperture angle values of the TO/RO receive coil as well as the T/R coil configuration. The SNR profiles as a function of aperture angle in Figure 2.2 (c) from C to D and E to F are negligible compared to profile A to B since the SNR is dominated by the rungs of the saddle shaped coil at the ROI. Optimization the aperture angle to achieve the highest SNR is dominated by the choice of AB profile. The optimum aperture angle was determined to be approximately 120^{o} from Figure 2.2 (c) for the highest $\mathbf{B}_{1-}$ sensitivity and uniformity in agreement with a previous study (40).

Table 2.2: Comparison of SNR measured in the thermally-polarized gas phantom using the TO/RO and commercial T/R birdcage coil configurations respectively.

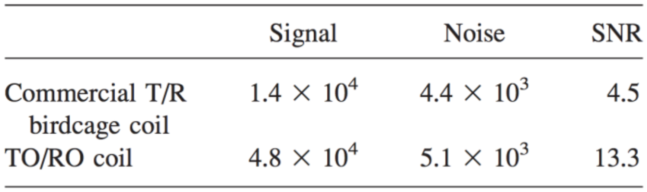

	Signal	Noise	SNR
Commercial T/R birdcage coil	1.4×10^4	4.4×10^3	4.5
TO/RO coil	4.8×10^4	5.1×10^3	13.3

Figure 2.3 shows a schematic of commercial T/R birdcage and TO/RO coil set-up and corresponding FGRE axial images from the thermal gas phantom. The corresponding SNR values are shown in Table 2.2. The TO/RO coil design provided an SNR improvement of a factor of three compared to the commercial T/R birdcage coil configuration. Table 2.3 shows the simulated and experimental uniformity values for four ROIs, U, obtained from the axial images of hyperpolarized gas phantom shown in Figure 2.4 (a) and (d), and the simulated $\mathbf{B}_{1-}$ field in Figure 2.4 (b) and (e) for both the TO/RO coil and commercial T/R birdcage coil. Figure 2.4 (c) and (f) show coronal MR images of rat lungs obtained from the same rat using TO/RO and commercial T/R birdcage coil configurations. Although the image SNR is not optimal due to low polarization, the improvement in the SNR with the TO/RO coil is apparent. In particular, the SNR improvement provided by the TO/RO coil allows visualization of the right lobe of lungs otherwise not apparent using the commercial T/R birdcage coil. SNR values were 19.7/0.63 and 7.5/0.62 for the TO/RO and T/R coil configurations respectively.

Table 2.3: Experimental and Simulated Axial Percentage B1- ROI Uniformity (U) for the Hyperpolarized Gas Phantom for both TO/RO and Commercial T/R Birdcage Coil Configurations [as shown in Fig. 2.4(b)].

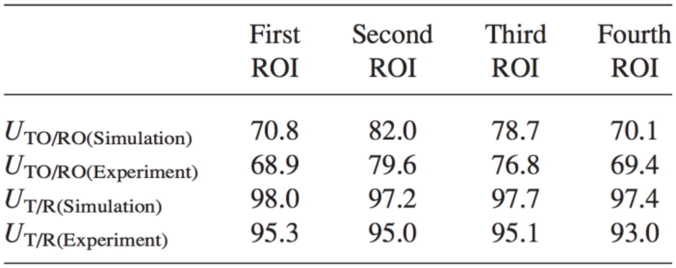

	First ROI	Second ROI	Third ROI	Fourth ROI
$U_{\text{TO/RO(Simulation)}}$	70.8	82.0	78.7	70.1
$U_{\text{TO/RO(Experiment)}}$	68.9	79.6	76.8	69.4
$U_{\text{T/R(Simulation)}}$	98.0	97.2	97.7	97.4
$U_{\text{T/R(Experiment)}}$	95.3	95.0	95.1	93.0

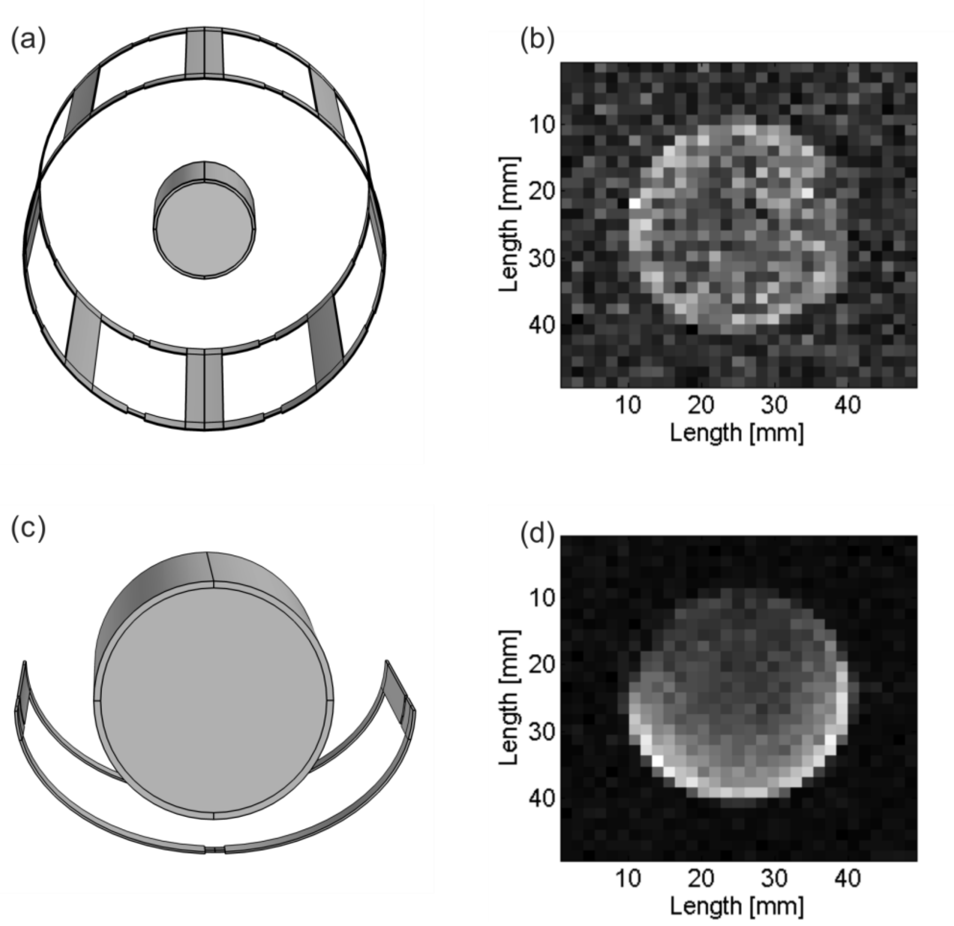

Figure 2.3: Schematic of thermal gas phantom and commercial T/R birdcage coil configuration (a) consisting of two end- rings of 12 cm diameter and eight rungs of length 18.0 cm each. Also shown is the corresponding axial image from the phantom (b). The saddle-shaped surface coil is shown schematically in (c) (transmit coil has been omitted) along with the phantom. Also shown is the corresponding axial image from the phantom (d).

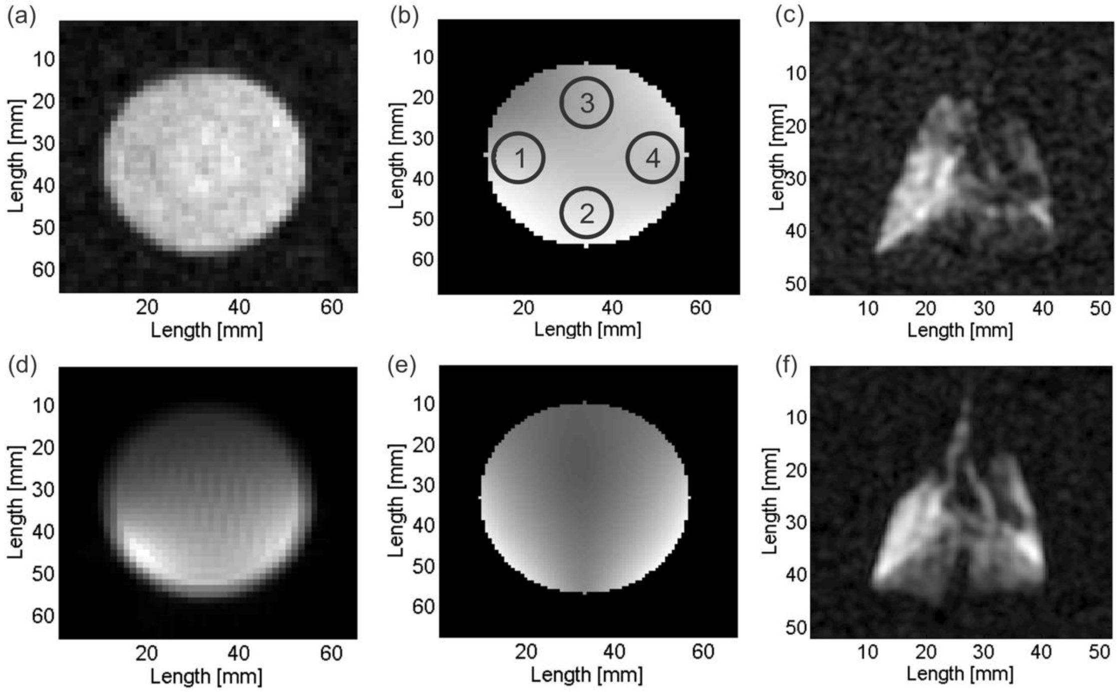

Figure 2.4: Axial images of hyperpolarized gas phantom using the commercial T/R birdcage coil (a) and the corresponding simulated B1- sensitivity map (b). Coronal image of rat lungs using the commercial T/R birdcage coil (c). Axial image of the hyperpolarized gas phantom using the TO/RO coil configuration (d) and the corresponding simulated B1- sensitivity map (e). Coronal image of rat lungs using the TO/RO coil (f).

The calculated B_{1+} map and flip angle profile for the TO/RO coil is shown in Figure 2.5 (a) and (b) respectively. The flip angle distribution was relatively homogenous with a mean flip angle of 60.2 ± 1.6^{o}. As expected, the mean flip angle was approximately the same as the prescribed nominal flip angle $\alpha_1 = 60 \pm 1^{o}$.

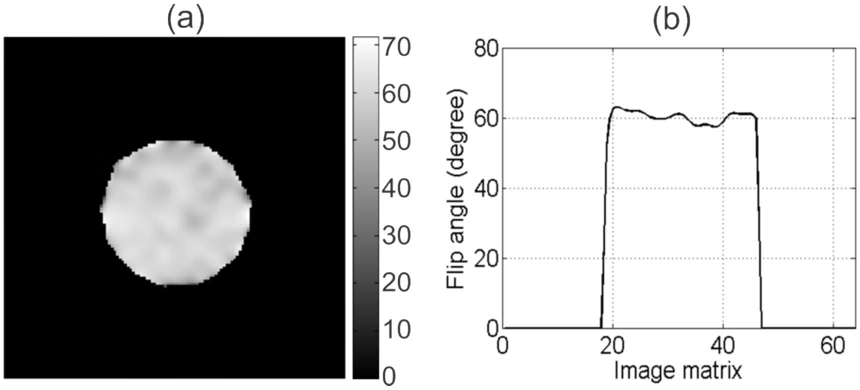

Figure 2.5: (a) B_1 map and (b) the flip angle profile (from A to B as shown in Figure 2.1) obtained from the TO/RO coil using the thermally polarized phantom.

2.4 Discussion

The TO/RO coil configuration provides a homogeneous excitation field and a high sensitivity for ^{129}Xe MRI of the rat lung. MR images from a thermally- polarized phantom confirm that a novel TO/RO configuration provides an improvement in SNR of up to a factor of approximately three compared to a commercial T/R birdcage coil of comparable geometry. The Q factor measurements allow a preliminary evaluation of the coil sensitivity depending on the various conditions including the coil dimensions (i.e. the $\mathbf{B_{1-}}$ sensitivity and inductance), shielding, resonance frequency and loading conditions. As expected, the Q factor of the TO/RO coil in transmit mode was 20% that of the commercial T/R birdcage coil due to the additional required pin diodes and chokes (as shown in Figure 2.1 (b)) for the switch circuits. We also noticed that the SNR performance of the TO/RO coil in T/R mode reduced after adding the necessary components and receive coil. Considering the same birdcage coil dimension used in our TO/RO and the commercial T/R coil configurations, the SNR of TO/RO coil in T/R mode was expected to be lower than the commercial T/R coil proportional to the square root of the Q factor (23). Although the quality factors between the commercial T/R birdcage coil and our saddle-shaped receive TO/RO coil cannot be directly compared due to the difference in dimensions, the loading factors can be compared to estimate the ohmic and electromagnetic losses. Based on the benchtop experiments, Lf was approximately the same for both coil configurations confirming that the coil is operating in the coil noise dominated regime and loading the coil with a rat-sized conductor (300 gr, 0.48S/m) does not significantly affect the SNR.

The transmit coil of the TO/RO configuration used here was designed to take advantage of the highly homogeneous transmit field of the birdcage geometry for imaging of hyperpolarized ^{129}Xe gas and dissolved phases, known to be sensitive to flip angle variations. Therefore, investigation of the TO/RO configuration in a “T/R” mode was not considered in the imaging and SNR comparison due to the expected lower efficiency compared to the purpose-built commercial birdcage T/R coil. The commercial T/R birdcage coil used here did not require the additional switch circuits but had the same birdcage coil dimensions as the TO/RO configuration. Therefore, it was considered a reasonable gold standard for the purposes of comparison between the TO/RO mode and a best-case T/R mode. Nonetheless, one of the limitations of the TO/RO design used here was the lower efficiency in T/R mode which could presumably be improved in future if required.

When the aperture angles of receive coils are compared, both 120^o and 140^o showed a high sensitivity (Figure 2.2 (c)). However, the $\mathbf{B_{1-}}$ sensitivity profile at 120^o is much more uniform compared to 140^o with a strong increasing signal toward the edges and decreasing at the center. This confirms that the choice of receive aperture angle of 120^o was a good trade-off between overall $\mathbf{B_{1-}}$ sensitivity and uniformity. Further SNR improvements with the TO/RO approach should be possible using a multichannel receiver coil design (17,19,41).

The numerical simulations of $\mathbf{B_{1+}}$ uniformity for the TO/RO configuration shows reasonable agreement with the experimental values (Table 3). Simulated $\mathbf{B_{1+}}$ uniformity was approximately 70% at ROI one and four, and approximately 80% at ROI three and four for the axial images (Figure 2.4 (e) and Table 2.3). As expected, the T/R coil had better uniformity (~95%) for the same ROIs (Fig 4 (b)). The difference between experiments and simulated uniformity (~3%) are likely due to the small variations in excitation flip angle. The percentage variation in the simulated $\mathbf{B_{1+}}$ uniformity is less than 3% at each of the ROIs, which was in agreement with the early experimental measurement of $\mathbf{B_{1+}}$ for the commercial T/R coil (39). Although the $\mathbf{B_{1+}}$ maps of the TO/RO in T/R mode were not measured in this work, they are expected to be better than $\mathbf{B_{1+}}$ maps of the TO/RO since it includes the $\mathbf{B_{1+}}$ inhomogeneity due to the receive coil. $\mathbf{B_{1+}}$ profile obtained using TO/RO coil exhibited a uniform flip angle distribution with flip angle variations less than 3% of the nominal flip angle which was similar to the previously published study (20).

The thermally-polarized phantom experiments were more consistent for comparing the SNR between TO/RO and T/R coil configurations since the *in vivo* signal strongly depends on animal ventilation conditions, including polarized bag pressure, ventilation or surgical related defects of the lungs while transferring from one coil to another, and the amount of polarization. Although the signal is sensitive to the experimental conditions, similar noise values were observed when the coils were loaded with rat and thermally-polarized phantoms. The results show the SNR improvement corresponds to an increased sensitivity for the surface coil for both the thermal phantom and *in vivo (*loaded) configurations.

2.5 Conclusion

The use of a TO/RO radiofrequency coil configuration is advantageous for MRI of hyperpolarized ^{129}Xe providing an approximate three-fold SNR improvement, with a $\mathbf{B}_{1+}$ transmit field variation of less than three percent. Although the $\mathbf{B}_{1-}$ reception sensitivity is less uniform (approximately 30 %) compared to a T/R (i.e. birdcage) coil, this can be corrected by post-processing based on the simulated or measured reception sensitivity profile of the receive coil.

2.6 References

1. Mugler JP, 3rd, Altes TA, Ruset IC, et al. Simultaneous magnetic resonance imaging of ventilation distribution and gas uptake in the human lung using hyperpolarized xenon-129. Proceedings of the National Academy of Sciences of the United States of America 2010;107(50):21707-21712.

2. Freeman MS, Cleveland ZI, Qi Y, Driehuys B. Enabling hyperpolarized (129) Xe MR spectroscopy and imaging of pulmonary gas transfer to the red blood cells in transgenic mice expressing human hemoglobin. Magn Reson Med 2013 ;70(5): 1192-1199.

3. Boudreau M, Xu X, Santyr GE. Measurement of 129Xe gas apparent diffusion coefficient anisotropy in an elastase-instilled rat model of emphysema. Mag Reson in Med 2013;69(1):211-220.

4. Mansson S, Wolber J, Driehuys B, Wollmer P, Golman K. Characterization of diffusing capacity and perfusion of the rat lung in a lipopolysaccaride disease model using hyperpolarized Xe-129. Magn Reson Med 2003;50(6):1170-1179.

5. Santyr GE, Lam WW, Parra-Robles JM, Taves TM, Ouriadov AV. Hyperpolarized noble gas magnetic resonance imaging of the animal lung: Approaches and applications. J Appl Phys 2009;105(10).

6. Driehuys B, Cofer GP, Pollaro J, Mackel JB, Hedlund LW, Johnson GA. Imaging alveolar-capillary gas transfer using hyperpolarized Xe-129 MRI. Proceedings of the National Academy of Sciences of the United States of America 2006;103(48):18278-18283.

7. Patz S, Muradian I, Hrovat MI, et al. Human pulmonary imaging and spectroscopy with hyperpolarized Xe-129 at 0.2T. Acad Radiol 2008;15(6):713-727.

8. Fox MS, Ouriadov A, Thind K, et al. Detection of radiation induced lung injury in rats using dynamic hyperpolarized Xe-129 magnetic resonance spectroscopy. Med Phys 2014;41(7).

9. Fox MS, Ouriadov A, Santyr GE. Comparison of Hyperpolarized He-3 and Xe-129 MRI for the Measurement of Absolute Ventilated Lung Volume in Rats. Magn Reson Med 2014;71(3):1130-1136.

10. Couch MJ, Ouriadov A, Santyr GE. Regional ventilation mapping of the rat lung using hyperpolarized 129Xe magnetic resonance imaging. Magn Reson Med 2012;68(5):1623-1631.

11. Ouriadov AV, Lam WW, Santyr GE. Rapid 3-D mapping of hyperpolarized He-3 spin-lattice relaxation times using variable flip angle gradient echo imaging with

application to alveolar oxygen partial pressure measurement in rat lungs. Magn Reson Mater Phy 2009;22(5):309-318.

12. Wild JM, Paley MNJ, Viallon M, Schreiber WG, van Beek EJR, Griffiths PD. k-space filtering in 2D gradient-echo breath-hold hyperpolarized He-3 MRI: Spatial resolution and signal-to-noise ratio considerations. Magn Reson Med 2002;47(4):687-695.

13. Doty FD, Entzminger G, Kulkarni J, Pamarthy K, Staab JP. Radio frequency coil technology for small-animal MRI. Nmr Biomed 2007;20(3):304-325.

14. Dominguez-Viqueira W, Lau AZ, Chen AP, Cunningham CH. Multichannel receiver coils for improved coverage in cardiac metabolic imaging using prepolarized 13C substrates. Mag Reson Med 2013;70(1):295-300.

15. Barberi EA, Gati JS, Rutt BK, Menon RS. A transmit-only/receive-only (TORO) RF system for high-field MRI/MRS applications. Magn Reson Med 2000;43(2):284-289.

16. Jin J. Electromagnetic Analysis and Design in Magnetic Resonance Imaging: CRC Press: 1998.

17. Dregely I, Ruset IC, Wiggins G, et al. 32-channel phased-array receive with asymmetric birdcage transmit coil for hyperpolarized xenon-129 lung imaging. Magn Reson Med 2013;70(2):576-583.

18. Deppe MH, Teh K, Parra-Robles J, Lee KJ, Wild JM. Slice profile effects in 2D slice-selective MRI of hyperpolarized nuclei. Journal of magnetic resonance 2010;202(2):180-189.

19. Lee RF, Johnson G, Grossman RI, Stoeckel B, Trampel R, McGuinness G. Advantages of parallel imaging in conjunction with hyperpolarized helium- A new approach to MRI of the lung. Magn Reson Med 2006;55(5):1132-1141.

20. Lim H, Thind K, Martinez-Santiesteban FM, Scholl TJ. Construction and Evaluation of a Switch-Tuned C-13 - H-1 Birdcage Radiofrequency Coil for Imaging the Metabolism of Hyperpolarized C-13-Enriched Compounds. J Magn Reson Imaging 2014;40(5):1082-1090.

21. Wetterling F, Tabbert M, Junge S, Gallagher L, Macrae IM, Fagan AJ. A double-tuned H-1/Na-23 dual resonator system for tissue sodium concentration measurements in the rat brain via Na-MRI. Phys Med Biol 2010;55(24):7681-7695.

22. Cleveland ZI, Moller HE, Hedlund LW, et al. In Vivo MR Imaging of Pulmonary Perfusion and Gas Exchange in Rats via Continuous Extracorporeal Infusion of Hyperpolarized Xe-129. PloS one 2012;7(2).

23. Dominguez-Viqueira W, Berger W, Parra-Robles J, Santyr GE. Litz Wire Radiofrequency Receive Coils for Hyperpolarized Noble Gas MR Imaging of Rodent Lungs at 73.5 mT. Concept Magn Reson B 2010;37b(2):75-85.

24. Carias MF, Dominguez-Viqueira W, Santyr GE. Improving Signal-to-Noise Ratio of Hyperpolarized Noble Gas MR Imaging at 73.5 mT Using Multiturn Litz Wire Radiofrequency Receive Coils. Concept Magn Reson B 2011;39b(1):37-42.

25. Asfour A. A three-coil RF probe-head at 2.35 T: potential applications to the Na-23 and to the hyperpolarized Xe-129 MRI in small animals. Ieee Eng Med Bio 2010:5693-5699.

26. Mispelter J, Lupu M, Briguet A. NMR Probeheads for Biophysical and Biomedical Experiments: Theoretical Principles & Practical Guidelines: Imperial College Press: 2006.

27. Gilbert KM, Scholl TJ, Chronik BA. RF coil loading measurements between 1 and 50 MHz to guide field-cycled MRI system design. Concept Magn Reson B 2008;33b(3):177-191.

28. Hoult DI. The NMR receiver: A description and analysis of design. Progress in Nuclear Magnetic Resonance Spectroscopy 1978;12(1):41-77.

29. Fox MS, Welch I, Hobson D, Santyr GE. A novel intubation technique for minimally invasive longitudinal studies of rat lungs using hyperpolarized 3He magnetic resonance imaging. Laboratory animals 2012;46(4):311-317.

30. Santyr GE, Lam WW, Ouriadov A. Rapid and efficient mapping of regional ventilation in the rat lung using hyperpolarized 3He with Flip Angle Variation for Offset of RF and Relaxation (FAVOR). Magn Reson Med 2008;59(6):1304-1310.

31. Multiphysics C. MRI Birdcage Coil: Comsol Model Library Version. 3.5

32. Association NEM. Determination of image uniformity in diagnostic magnetic resonance images. Rosslyn, VA: NEMA Standards Publication MS 6-2008 2008. p. 1-21.

33. Krinke GJ, Bullock GR, Bunton T. The Laboratory Rat: Elsevier Science: 2000.

34. Vaughan JT, Adriany G, Garwood M, et al. Detunable transverse electromagnetic (TEM) volume coil for high-field NMR. Magn Reson Med 2002;47(5):990-1000.

35. Firbank MJ, Coulthard A, Harrison RM, Williams ED. A comparison of two methods for measuring the signal to noise ratio on MR images. Phys Med Biol 1999;44(12):N261-N264.

36. Wade TP, McKenzie C, Rutt B. Theoretical and Experimental Efficiency and Optimization of Flip Angle Mapping Techniques Proceedings of the 19th Annual Meeting of ISMRM 2011;Montréal(Québec):(abstract 4425).

37. Stollberger R, Wach P. Imaging of the active B1 field in vivo. Magn Reson Med 1996;35(2):246-251.

38. Insko EK, Bolinger L. Mapping of the Radiofrequency Field. J Magn Reson Ser A 1993;103(1):82-85.

39. Ouriadov AV, Lam WW, Santyr GE. Rapid 3-D mapping of hyperpolarized 3He spin-lattice relaxation times using variable flip angle gradient echo imaging with application to alveolar oxygen partial pressure measurement in rat lungs. Magma 2009;22(5):309-318.

40. Ginsberg DM, Melchner MJ. Optimum Geometry of Saddle Shaped Coils for Generating a Uniform Magnetic Field. Rev Sci Instrum 1970;41(1):122-123.

41. Deppe MH, Parra-Robles J, Marshall H, Lanz T, Wild JM. A Flexible 32-channel Receive Array Combined With a Homogeneous Transmit Coil for Human Lung Imaging With Hyperpolarized He-3 at 1.5 T. Magn Reson Med 2011;66(6):1788-1797.

Chapter 3 : Hyperpolarized Dissolved ^{129}Xe MRI of the Rat Lung

This chapter is adapted from the published paper: Doganay O, Wade T, Hegarty E, McKenzie C, Schulte RF, Santyr GE. Hyperpolarized ^{129}Xe Imaging of the Rat Lung using Spiral IDEAL. *Magn. Reson. Med*. doi:10.1002/mrm.25911.

3.1 Introduction

Hyperpolarized (Hp) ^{129}Xe gas can provide an increase in NMR signal of up to a factor of 100,000 compared to thermally polarized ^{129}Xe gas. MRI of Hp ^{129}Xe gas following inhalation enables unique functional and microanatomical lung imaging measurements, including ventilation defects (1) and apparent diffusion coefficient (ADC) (2). Although most of the inhaled Hp ^{129}Xe lung signal originates from the gas phase, approximately 2% of the signal originates from ^{129}Xe dissolved in the pulmonary tissue (PT, or barrier tissues) and red blood cell (RBC) compartments (3). These dissolved phase ^{129}Xe signals can be separated using MR spectroscopy approaches, taking advantage of the significant chemical shifts, relative to the gas phase, of ^{129}Xe dissolved in PT (197 ppm) and RBC (217 ppm) compartments, with respect to the gas phase (4). Furthermore, by measuring the time course of the lung RBC and PT ^{129}Xe signals following spectrally-selective RF saturation (e.g. chemical shift saturation recovery, CSSR), measures of perfusion (5) and pulmonary gas exchange (6) respectively can be derived. Pulmonary gas exchange measured with Hp ^{129}Xe CSSR spectroscopy in whole lungs has been shown to be sensitive to alveolar tissue thickening, which is associated with early pneumonitis (i.e. inflammation) in radiation-induced lung injury (RILI) (7) and in idiopathic pulmonary fibrosis (8).

MRI pulse sequences for imaging dissolved phases of Hp ^{129}Xe in the lung need to address the following specific challenges: (i) low lung ^{129}Xe T_2^* (~2 ms at 2 T (9)) leading to rapid signal loss and image blurring, (ii) poor SNR due to low density of ^{129}Xe in the RBC and PT compartments and (iii) short breath-hold time (~ 10 s). An image acquisition scheme that acquires k-space with the fewest number of RF pulses, and a read-out time on the order of T_2^* would enable high flip angles to be used, thus significantly increasing the SNR, spatial and temporal resolution. Improved temporal resolution would also allow improved SNR via increased replenishment by the gas phase within a short breath-hold interval, as well as quantification of the exchange between gas, PT and RBC compartments.

A 3-point Dixon approach has been reported for separation of gas and dissolved phases within a single breath-hold at both 0.2 T (10) and 3 T (11); however, dissolved phase SNR was limited in that study by the use of relatively long echo times and low flip angles. PT and RBC ^{129}Xe signals have been spectrally resolved using a one-point variant of the Dixon technique for 2D imaging of both rats (9) and humans (12). This approach has also been extended to 3D rat imaging within a breath-hold time of approximately 16 seconds by using the replenishment of xenon from the gas phase between k-space acquisitions (13). A recent study by Qing et. al. took advantage of the use of hierarchical IDEAL (Iterative Decomposition of water and fat with Echo Asymmetry and Least-square estimation) to image the gas, PT and RBC phases simultaneously within a scan time of a single breath-hold (approximately 11 s) based on the independent excitation of the gas and dissolved phase compartments using a 3D radial pulse sequence (14). In this work, however, the dissolved phase magnetization was excited with a relatively low flip angle and without substantial replenishment of the dissolved phase compartments by the gas phase.

A robust and efficient IDEAL imaging technique based on a single-shot spiral acquisition and echo-time shifting in between excitations has been reported for Hp ^{13}C-pyruvate metabolic imaging (15). Additionally, Hp [1-^{13}C] pyruvate metabolic imaging using a single-shot spiral acquisition within the T_2^* relaxation time (~40 ms) and a 90^{o} selective RF pulse to maximize SNR has been demonstrated in phantoms and *in vivo* (16).

In this study, a single-shot spiral IDEAL approach was designed and implemented for rapid imaging of Hp ^{129}Xe gas, PT and RBC compartments in the rat lung. The spiral read-out time was optimized to maximize both the spatial resolution and SNR of the dissolved phase Hp ^{129}Xe images. The echo time spacing was also optimized using the effective number of averages (NSA) approach. The optimal flip angles were calculated through a theoretical Bloch equation analysis including the effect of gas exchange. The feasibility of the method was demonstrated for three-point IDEAL imaging of gas/PT compartments and four-point IDEAL imaging of gas/PT/RBC compartments in rat lungs. Two-dimensional IDEAL images using separate breath-holds at different TR values were acquired to demonstrate the feasibility of regional measurement of gas exchange.

3.2 Theory

3.2.1 Point Spread Function (PSF) Analysis

The PSF was calculated to investigate the effects of read-out time, T_{read}, (as shown in Figure 3.1) on image SNR and spatial resolution. For spiral k-space sampling, the PSF was calculated using the inverse Fourier transform of the modulation transfer function in Matlab (R2013a, The Mathworks Inc., Massachusetts), which incorporates the effects of sampling, truncation, and T_2^* (17) as described in detail in Appendix A (see Calculation of Spiral PSF) (18) and (19). For comparison, the PSF for conventional Cartesian k-space sampling was calculated analytically along the frequency encoding direction as described in Appendix B (Calculation of Cartesian PSF). Spatial resolution was approximated using the FWHM of the calculated PSF function as a function of T_{read}/T_2^* to demonstrate the effects of T_2^* blurring on resolution. SNR was approximated from the corresponding PSF amplitude, $A(T_{read}/T_2^*)$ using the following expression:

$$SNR_N \propto A(T_{read}/T_2^*) \times \sqrt{\mathrm{N/BW}} \times \sin(\alpha) \qquad [3.1]$$

;where, α is the flip angle, N is number of points in k-space and BW is the read-out bandwidth. The $\sin(\alpha)$ term accounts for the difference in the flip angle used for Cartesian and spiral, depending on the number of RF pulses and/or views. The N/BW term accounts for the effect of bandwidth on image noise. The BW was varied to change the read-out time, $T_{read} = N/BW$ for a fixed N. The effect of varying the BW on the noise was proportional to the square root of the BW.

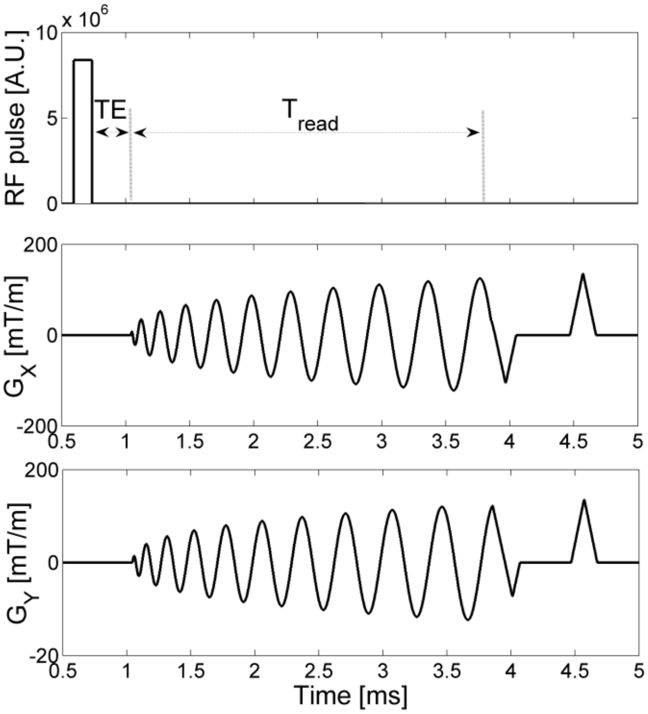

Figure 3.1: Pulse sequence timing diagram for the spiral acquisition of a single echo. A hard pulse is followed by read-out gradients (G_x and G_y) during which data acquisition occurs. The echo time $TE = \Delta TE \times m$ is defined as the echo time spacing multiplied by the number of echoes. Following the data acquisition, transverse magnetization is spoiled with gradients prior to the next acquisition at an echo time shifted according to the IDEAL approach.

Eqn. [3.1] was used for optimization of SNR with respect to T_{read} for the spiral k-space sampling. It was also used to predict the SNR of the single-shot spiral k-space sampling in comparison to Cartesian. For fair comparison, the $A(T_{read}/T_2^*)$ were calculated using the same nominal resolution for both the Cartesian and spiral k-space sampling. Thus, for the Cartesian sampling, a matrix size of 32 × 32, *FOV* of 10 cm and *BW* = 16 kHz was chosen similar to that used previously for *in vivo* Hp ^{129}Xe rat lung imaging (11). A constant flip angle of 15° was used for the corresponding matrix size of the Cartesian sampling scheme to achieve the maximum SNR (20,21). A flip angle of 90° was used for the spiral SNR calculation for thermally-polarized gas phantom experiments (as described in the Phantom MRI Experiments section below).

3.2.2 Spiral Gradient Waveform Design

Spiral k-space trajectory and gradient waveforms $(G_x(t), G_y(t))$ required to achieve a given T_{read} were calculated using an algorithm similar to that described by Lee *et al.* (22). A surface plot of T_{read} as a function of both maximum gradient amplitude (G_{max}) and gradient slew rate (SR) was generated for a FOV = 70 mm and in plane voxel size of 3 mm corresponding to typical rat imaging parameters. For the calculation, G_{max} was varied between 0 and 500 mT/m in steps of 20 mT/m and SR was varied between 0 to 3000 T/m/s in steps of 100 T/m/s, corresponding to the capabilities of the high performance gradient coil used in the study (23). This was also compared to a trajectory optimized for the performance of the conventional clinical gradient system ($\mathrm{G_{max}}$ = 50 mT/m, SR = 200 mT/m) to investigate the feasibility of human imaging.

3.2.3 Optimization of Echo-Time spacing

The optimal echo times, TE, for IDEAL were determined theoretically using the effective number of signal averages (NSA) approach by including the short T_2^* effect as previously described for C-13 metabolites (16,24). This approach accounts for the noise performance as a function of echo time spacing, ΔTE, and chemical shift (24). From these analyses, the optimal TE for each echo image, m, were calculated with $TE = \Delta TE \times m$ for the corresponding ΔTE from Figure 3.4. ΔTE was 50 us for 3-point IDEAL (m = 1, 2, 3) gas-PT imaging and 340 us for 4-point IDEAL (m = 1, 2, 3, 4) gas-PT-RBC imaging based on the known chemical shift differences ($\Delta f_{G\text{-}PT}$ = 6950 Hz, $\Delta f_{PT\text{-}RBC}$ = 525 Hz at a field strength of 3 T). This choice of *TE* was based on measured T_2^* values of gas and dissolved phases as described in the results section.

3.2.4 Calibration of Flip Angles

In delivering the RF excitation to each phase (e.g., gas versus dissolved phase), it was desirable to apply a sufficiently large flip angle (e.g. 10-20 degrees) to the gas phase to achieve reasonable gas phase image SNR without exhausting the gas phase pool, while at the same time applying a large flip angle (i.e. 90°) to the dissolved phases. This provided the additional benefit of improved dissolved phase SNR via replenishment from the gas phase between each image acquisition. The dependence of Hp ^{3}He gas image SNR on flip angle for different varying RF pulse number (i.e., phase-encoding step) has been discussed by Miller *et al*. (20). Using a similar approach, gas signal strength, S_G, and PT signal strength, S_{PT}, equations were derived from the analytic solutions to the Bloch equations including the effect of exchange of magnetization between the PT and gas compartments (Appendix). The gas and PT signal dependence following the n^{th} RF pulse are respectively given by the following two equations:

$$S_G = M_G\,[cos(\alpha_G)]^{n-1}\,sin(\alpha_G) \qquad [3.2]$$

$$S_{PT} = M_{PT}\,[\,M(TR)\,[\cos(\alpha_G)]^{n-1}\,sin(\alpha_{PT}) + [cos(\alpha_{PT})]^{n-1}\,sin(\alpha_{PT})] \qquad [3.3]$$

;where α_G and α_{PT} are the flip angles applied to the gas phase and PT phase respectively. M_G is a scaling factor based on the gas phase image, which accounts for differences in polarization and ventilation conditions between scans, $M(TR)$ represents the percentage replenishment of dissolved phase magnetization by the gas phase as a function of the time between RF pulses (TR). $M(TR)$ was calculated by fitting the Mansson gas exchange model to CSSR experimental data previously published by Fox *et al.* (7). $M(TR)$ was approximately 0.5 for the TR used in this study (30 ms) (see Appendix [C.6] for more details). M_{PT} is a scaling factor based on the dissolved phase image, which accounts for solubility, tissue density and M_G. T_1 relaxation of ^{129}Xe in both the gas and dissolved phases (25) is ignored in Eqn. [3.2] as it was assumed to be much longer than the total imaging time. Eqn. [3.3] shows that S_{PT} is reduced with the use of larger α_G and increased with the use of larger α_{PT} and larger TR, the latter due to replenishment. The SNR of the gas image, SNR_G, and SNR of the PT image, SNR_{PT}, were optimized as a function of α_G and α_{PT}, including the SNR improvement due to the number of averages.

3.3 Methods

All images were acquired using a 3 Tesla MRI system (MR750, GEHC, Wisconsin, USA), a custom-built transmit-only/receive-only birdcage coil (26) and high performance insertable gradient system (23). Images were reconstructed in Matlab as described in Schulte *et al.* (15,16).

3.3.1 Phantom MRI Experiments

A thermally-polarized phantom, containing 200 ml of ^{129}Xe gas (80% enriched) and 200 ml O_2 gas (to reduce T_1 relaxation to ~1 s) at a pressure of 8 atmosphere at room temperature, was used to experimentally confirm the theoretical dependence of spatial resolution on T_{read}/T_2^*. T_2^* for the thermal phantom was measured to be 28±1 ms. 2D projection images of the thermally-polarized phantom in the axial view were obtained with the following eight values of T_{read}/T_2^* = 0.5, 1.0, 1.5, 2.0, 2.5, 3.0, 3.5, 4.0 using a 3-point IDEAL spiral approach with the following parameters: TR = 1.0 s, ΔTE = 50 us, FOV = 10 cm × 10 cm, with a real pixel size of 32, BW = 62.5 kHz, number of averages = 8, flip angle = 90^o. T_{read} was adjusted experimentally by changing the SR of the spiral gradient waveforms $(G_x(t), G_y(t))$. Experimentally measured resolution including T_2^* blurring were calculated from thermal phantom images by the FWHM of the PSF as described in Appendix (19).

3.3.2 *In vivo* MRI experiments

All procedures followed animal use protocols approved by Western University’s Animal Use Subcommittee and were consistent with the guidelines written by the Canadian Council on Animal Care (CCAC) (27). Five Sprague Dawley rats (390±7 g, Charles River Laboratories, Saint-Constant, Canada) were imaged in the supine position following three breaths of Hp ^{129}Xe using a MRI-compatible mechanical ventilator (GE Healthcare, Malmo, Sweden) for delivery of Hp ^{129}Xe to the lung. Hp ^{129}Xe gas (approximately 80% enriched with 10% polarization) was obtained from a commercial xenon polarizer system (Polarean 9800, Durham, NH) yielding polarizations of ~10%. *In vivo* images were acquired with a three-point IDEAL approach for imaging of gas-PT and four-point IDEAL approach for imaging of gas-PT-RBC using the spiral pulse sequence as shown in Figure 3.1. A set of IDEAL coronal projection gas-PT images were obtained using a single-shot spiral three-point IDEAL technique and three RF pulses (n = 3) and echo images with echo-times of 50 us × m, (m = 1, 2, 3, resulting in a total scan time of 90 ms for TR =30 ms). IDEAL images of gas, PT and RBC were obtained with a single-shot four-point IDEAL technique using four RF pulses (n = 4) and four echo images with echo-times of 340 us × m, (m = 1, 2, 3, 4 resulting in a total scan time of 120 ms for TR = 30 ms). Other pulse sequence parameters included: FOV = 70 mm, BW = 125 kHz, a nominal matrix resolution of 22, number of points in the k-space equal to 660 and spiral trajectories consisting of 11 turns.

To validate Eqns. [3.2] and [3.3], multiple IDEAL gas and PT images (21 pairs) were acquired using 63 RF pulses (n = 63) with TR fixed at 30 ms within a total scan time of 1.92 s during a single breath-hold interval. A mask that corresponded to the left lung of each rat was created from the first gas phase image and applied to the all proceeding tissue images. $S_G(j)$ and $S_{PT}(j)$ were determined by the mean values of regions of interest placed on the gas and PT images as a function of image number (j = 1, ..., $n/3$ = 21). For comparison between rats, the multiple Hp ^{129}Xe IDEAL images were normalizing by $S_{PT}(j = 1{:}21)$ with $S_G(j = 1)$,since the absolute values of $S_{PT}(j)$ depend on experiment conditions (e.g., polarization, ventilation) through the scaling factor M_{PT} (as explained in Eqn. [3.3]). The mean of $S_G(j)$ and normalized $S_{PT}(j)$ and their standard deviations were also calculated to investigate the reproducibility of the IDEAL images.

Ten sets of coronal IDEAL gas, PT, RBC images (j = 1:10, n = 40) were obtained using a four-point IDEAL approach within a total scan time of approximately 4 s in a single-breath hold (with a TR of 100 ms) in the rat lung. IDEAL gas, PT, RBC images were reconstructed in Matlab. The ten reconstructed gas, PT, and RBC images were then averaged in Matlab to generate a final IDEAL gas, PT, and RBC images. Similarly, representative average coronal *in vivo* IDEAL gas and PT images were obtained using three-point spiral IDEAL (j = 1:10, n = 30) within a total scan time of approximately 3 s.

3.3.3 RF pulse calibration

To achieve the optimum α_{PT} and α_G, a hard pulse was centered at the PT resonance in order to maximize the signal from the tissue phase. The gas signal was excited using the side band of a rectangular (i.e., hard) RF pulse (28). When α_{PT}= 90^o, the side band excitation, α_G was much higher than the optimal. Therefore, the transmit power was decreased so that α_{PT} = 75^o resulting in α_G = 18^o. These flip angles were achieved using a pulse width of 0.18 ms to minimize the side band excitation of the gas phase and T_2^*amplitude loss. The actual α_{PT} and α_G values were calibrated be observing the free induction decay (FID) signal following the RF pulse. For this purpose, the hard pulse was centered on the gas phase and required power was adjusted to generate a 90^o excitation. Based on the power used to generate a 90^o excitation, the actual α_{PT} and α_G were calibrated to be approximately 75^o and 18^o respectively. For comparison, α_{PT} and α_G were calculated from multiple three-point IDEAL images *in vivo* using Eqns. [3.2] and [3.3].

As a proof-of-concept demonstration of the ability of the spiral IDEAL approach to measure gas exchange. four-point IDEAL images of gas, PT, RBC were obtained at five different TR values (30, 50, 100, 200, 300 ms) using five separate breath-holds respectively. Signal from PT images, $S_{PT}(j$ = 2:5, $TR)$ and RBC images $S_{RBC}(j$ = 2:5, $TR)$ were normalized with $S_G(j$ = 2:5, $TR)$. Dissolved phase signal from the first image (j =1) was ignored since it was not weighted by the TR. $S_{PT}(TR)$ and $S_{RBC}(TR)$ were calculated for the left and right lungs of five healthy rats and averaged to provide mean signals as a function of increasing TR.

3.4 Results

Theoretical and experimental dissolved phase spatial resolution from the PSF analysis and the thermal phantom for the eight T_{read}/T_2^* values respectively are shown in Figure 3.2 (a). As expected, measured blurring was diminished as read-out time was reduced and plateaued for $T_{read} \sim 1.5 \times T_2^*$ in good agreement with theory. Theoretical SNR from Eqn. [3.1] is shown in Figure 3.2 (b) over a similar range of T_{read}/T_2^* as in Figure 3.2 (a). The maximum SNR was obtained for T_{read} values between approximately T_2^* and $2 \times T_2^*$. The optimum value of T_{read}/T_2^* was chosen to be 1.8 to achieve the maximum SNR for the dissolved phase image while maintaining acceptable spatial resolution. $T_{read}/T_2^*= 1.8$ corresponded to a 33% decrease in resolution from the nominal pixel size. In particular, for a nominal pixel size of 3.1 mm, the spatial resolution was expected to be 4.1 mm due to T_2^* blurring. The theoretical maximum Cartesian SNR_N was found to occur at $T_{read}/T_2^* = 0.9$ similar to that previously reported (18). Compared to the Cartesian data acquisition with the use of flip angle of 15^o, the single-shot spiral showed a theoretical improvement in the SNR of 3.3 fold. It should be noted that this SNR improvement was expected to be less than 3.3-fold due to the dissolved signal replenishment between phase encoding steps (i.e. TR) of the Cartesian k-space sampling. The Cartesian acquisition with a TR time of 4 ms, would allow replenishment of dissolved phase signal of approximately 10 % (see Appendix Eqn. [C.5]. Therefore, considering the replenishment of the dissolved phase signal, the SNR improvement would be expected to be approximately 3-fold.

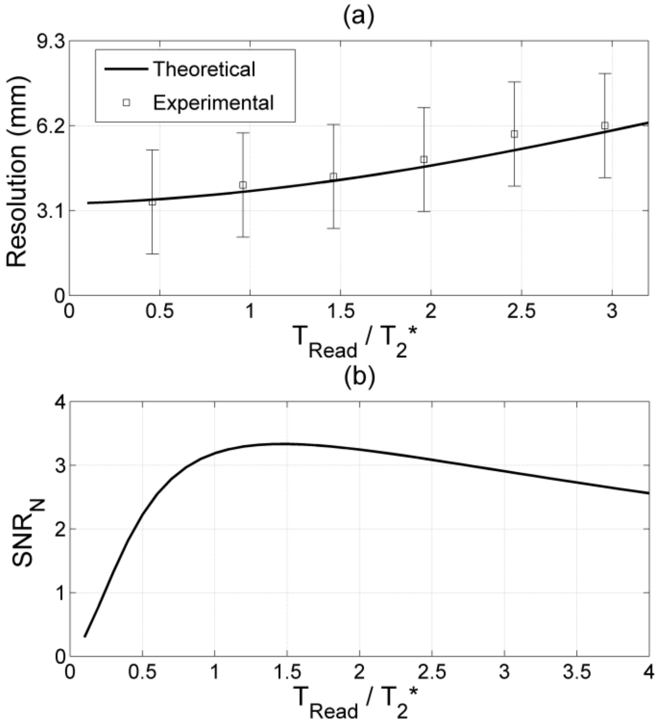

Figure 3.2: Theoretical spatial resolution (a) and normalized SNR_N (b) as a function of T_{read} / T_2^* spiral k-space trajectories. Experimental results are also shown for the measurement of FWHM in (a).

Figure 3.3 (a) shows the gradient amplitude and slew rate required to achieve a given T_{read} as well as the resulting spatial resolution for a given T_{read} at the optimal gradient amplitude and slew rate for *in vivo* imaging. For T_{read} of 2.8 ms, corresponding to T_{read}/T_2^* = 1.8 and the measured T_2^* values of 1.6±0.1 ms and 1.6±0.2 ms for PT and RBC respectively, the required G_{max} and SR were estimated from Figure 3.3 (a) to be 300 mT/m and 3000 T/m/s for fixed pixel size of 3 mm. It was noted that for T_{read} values less than 3.4 ms (G_{max} = 200 mT/m and SR = 3000 T/m/s), the gradient requirements did not change significantly. Repeating this process with the high-performance gradient parameters fixed at the optimum values G_{max} = 200 mT/m, SR = 3000 T/m/s, and FOV = 70 mm, the relationship between spatial resolution and T_{read} is shown in Figure 3.3 (b) (circle symbols). A read-out time of

2.8 ms was obtained for the nominal pixel size of 3.3 mm. The corresponding relationship for the conventional clinical gradient coil configuration with parameters fixed at the maximum values (G_{max} = 50 mT/m, SR = 200 T/m/s and FOV = 40 cm) for a six interleaved spiral acquisition is also shown in Figure 3.3 (b) (square symbols).

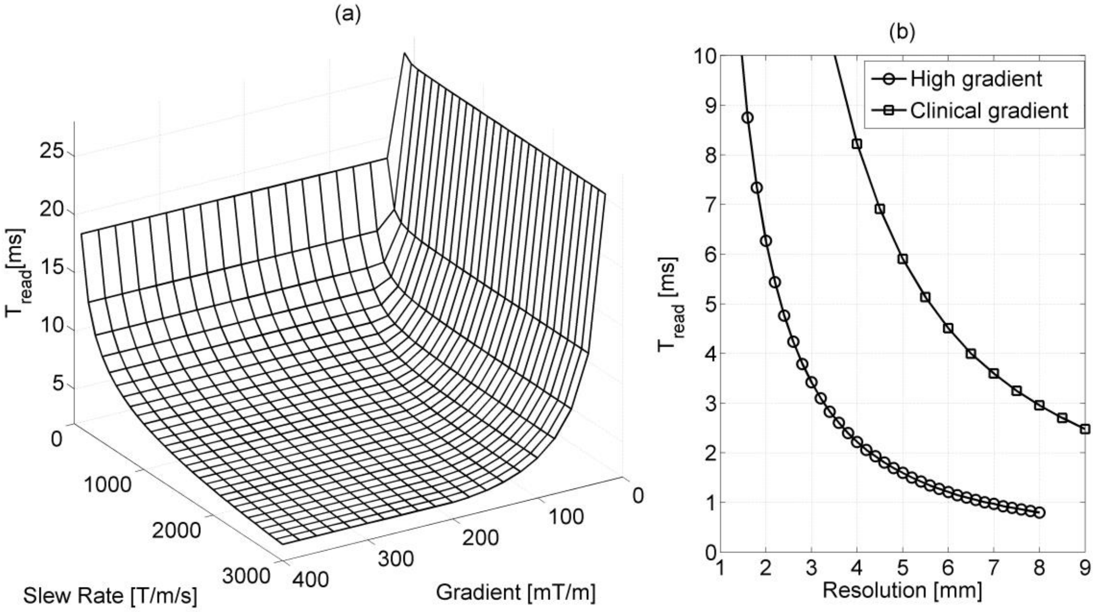

Figure 3.3: (a) A surface plot of T_{read} as a function of both maximum gradient amplitude (G_{max}) and gradient slew rate (SR) generated for a FOV = 70 mm and resolution of 3 mm. In (b) the read-out time as a function of resolution is shown for two gradient performance scenarios: (i) the high performance gradient for rat imaging (G_{max} = 300 mT/m, SR = 3000 T/m/s, FOV = 70 mm) and (ii) the clinical gradient performance for human imaging (G_{max} = 50 mT/m, SR = 200 T/m/s, FOV = 400 mm and six interleaves).

Figure 3.4 (a) shows NSA values as a function of ΔTE for 3-point and 4-point IDEAL approaches. Ignoring the effects of T_2^* amplitude loss, the maximum theoretical NSA was three and four for three-point and four-point IDEAL respectively. The optimum ΔTE values were found to be 50 us for the three-point IDEAL gas-PT imaging in Figure 3.4 (a). The corresponding NSA was found to be 2.8 due to T_2^* amplitude loss. Thus, it is reasonable to expect that the T_2^* amplitude loss was negligible for the three-point IDEAL approach. For four-point IDEAL, the optimum ΔTE that maximized NSA of all components and allowed separation of PT and RBC signals was found to be relatively long (340 us) in Figure 3.4 (b). These relatively long echo times are required due to the relatively smaller chemical shift difference between PT and RBC ($\Delta f_{PT\text{-}RBC}$= 525 Hz) leading to drop in the SNR of a factor of approximately two compared to the scheme without the T_2^* amplitude loss. Conceptually, the SNR performance of PT images from three-point IDEAL (Figure 3.4 (a)) is better than four-point IDEAL by a factor of 1.4 owing to relatively short echo times.

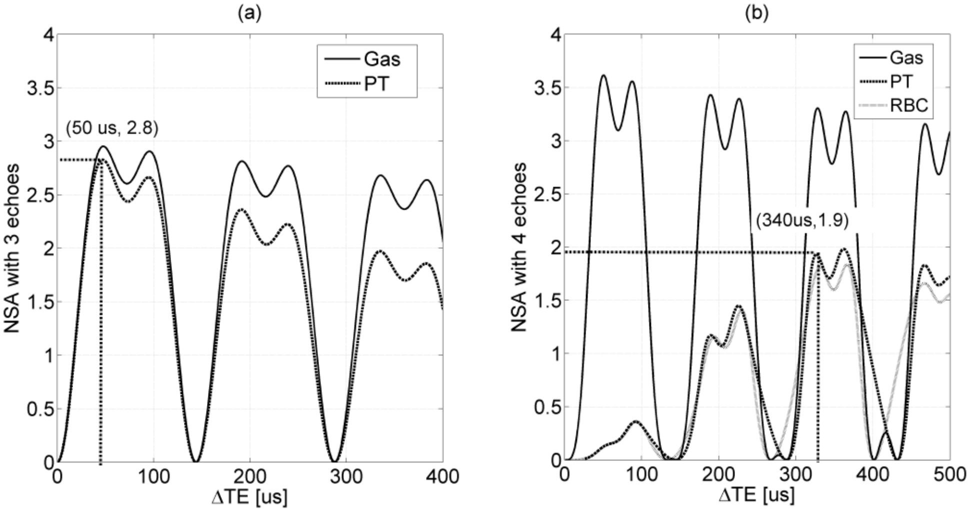

Figure 3.4: The NSA as a function of ΔTE for (a) 3-point IDEAL and (b) 4-point IDEAL.

Figure 3.5 (a) shows the measured mean $S_G(j)$ including standard deviation from the five healthy rats as well as the best fit to the data based on Eqn. [3.2] yielding estimated flip angles of $18^o \pm 0.4^o$ and R^2 value of 0.998. Figure 3.5 (b) shows the PT signal (i.e. normalized $S_{PT}(j)$) as a function of pulse number and the fit of function given by Eqn. [**3.3**] including gas exchange, yielding an R^2 value of 0.997. In the first PT image (j=1), the percentage gas exchange percentage rate (*M(TR)*) was determined to be 0.1 (7) since the first PT image (*TR* = 30 ms) is not weighted by gas exchange. *M(TR)* = 0.5 was used for fitting the remaining 20 images. The flip angle delivered to the PT phase was determined to be $75^{o}\pm2^{o}$ using Eqn. [3.3], in good agreement with the calibrated value. Normalized S_G and S_{PT} as a function of pulse number were highly reproducible for the five healthy rats with the maximum standard deviation value of 2.6%.

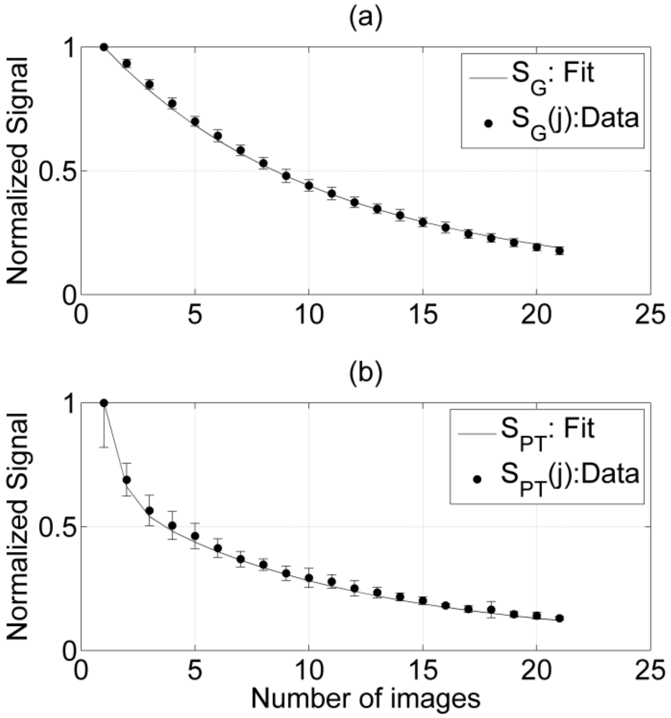

Figure 3.5: Experimentally measured gas (a) and pulmonary tissue (b) signals as a function of image number. The solid line shows the theoretical fit to the data from Eqns. [3.2] and [3.3].

Figure 3.6 shows the theoretical SNR performance of the gas and PT images as a function of both α_{PT} and α_G, after averaging 10 sets of IDEAL images. Figure 3.6 (a) shows that the use of α_G between 15° and 20° provides sufficiently high SNR for the gas phase image, but results in a reduction in the SNR of the tissue phase image in Figure 3.6 (b). This is because the Hp ^{129}Xe gas in the alveolar air space acts as a reservoir to replenish the dissolved phase image signal in the time between averages. Notably, $\alpha_G = 18^o$ was used to obtain a sufficiently high SNR for the gas phase of approximately 23 as shown in Figure 3.6 (a) and SNR_{PT} was approximately 5.8 as shown in Figure 3.6 (b). The theoretical dependences of SNR_{PT} on α_{PT} for TR = 30ms (circles) and TR = 100ms (square) are shown in Figure 3.6 (c), for α_G fixed at 18°. SNR_{PT} increases with α_{PT} but displays no significant increase beyond $\alpha_{PT}=75^o$ which corresponds to the use of 99% of available PT signal with a TR = 30 ms. Furthermore, Figure 3.6 (b) shows an SNR improvement of a factor of approximately 2 for TR = 100 ms due to the increased time for gas exchange.

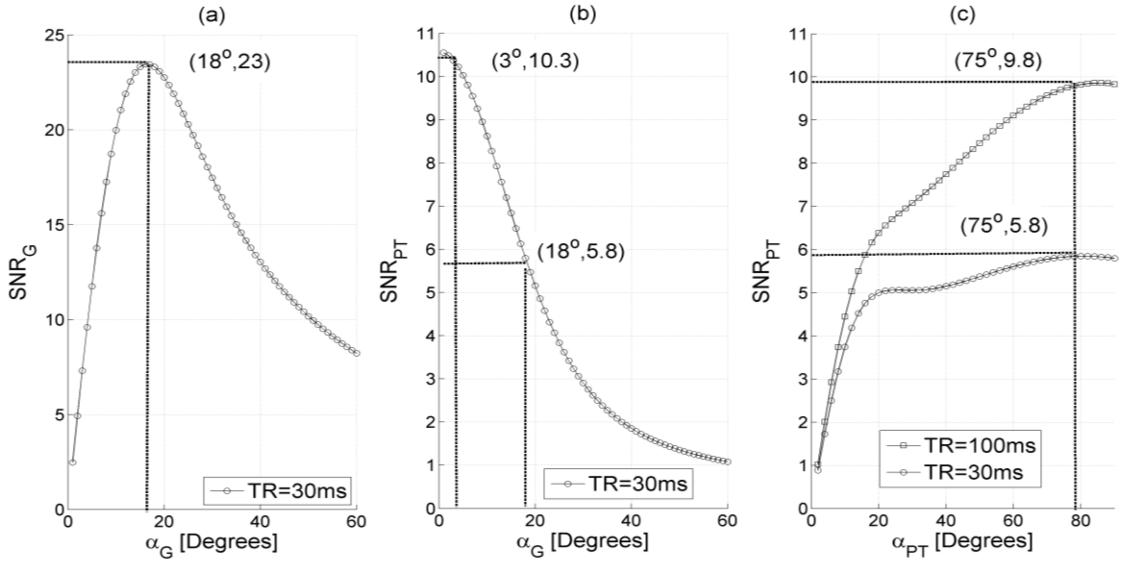

Figure 3.6: Theoretical SNR_G (a) and SNR_{PT} (b) as a function of α_G for α_{PT} fixed at 90^o. SNR_{PT} as a function of α_{PT} (c) for the α_G fixed at 18^o is also shown for TR = 30 ms (circles) and TR = 100ms (squares).

Figure 3.7 shows representative coronal *in vivo* IDEAL gas and PT images obtained using three-point spiral IDEAL with a *TR* of 100 ms in the rat lung within a total scan time of 3 s. The SNR of the gas and PT images were 22.8 and 10.2 respectively and satisfactory given the polarization of ~10%. Figure 3.8 shows representative coronal *in vivo* IDEAL gas, PT, and RBC images obtained using four-point spiral IDEAL with a *TR* of 100 ms in the rat lung within a total scan time of 4 s. The SNR of the gas image ($SNR_{Gas} = 23.0$) was similar to the gas image from three-point IDEAL. The SNR of the PT image ($SNR_{PT} = 8.6$) was higher than the RBC image ($SNR_{RBC} = 4.7$) due to the tissue-blood partition based on the different of xenon solubility and density in the dissolved compartments (5).

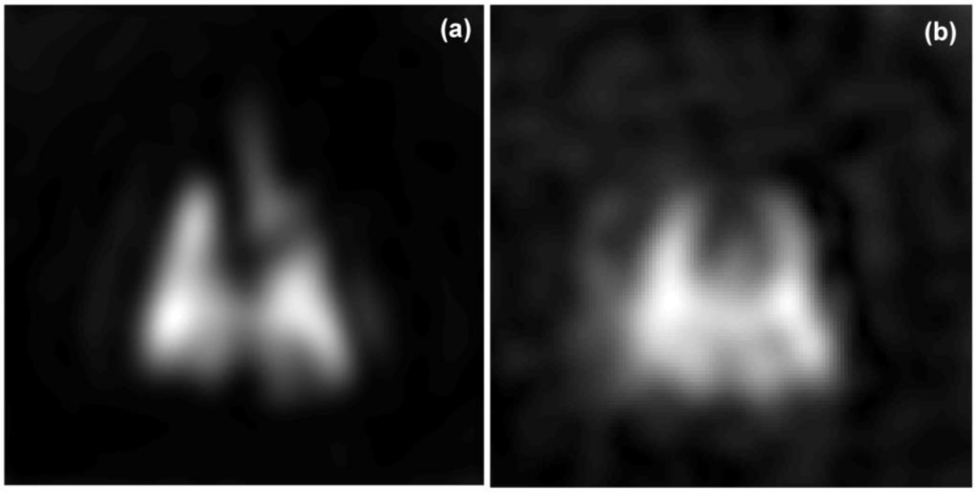

Figure 3.7: Coronal gas (a) and PT (b) images of a representative rat lung obtained using the three-point spiral IDEAL approach.

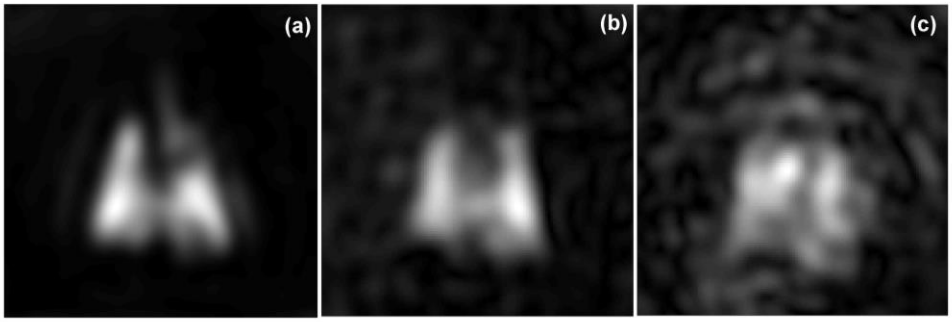

Figure 3.8: Coronal gas (a), PT (b), and RBC (c) images obtained using the four-point spiral IDEAL approach.

Figure 3.9 shows mean PT (a) and RBC signals (b) from the left and right lungs as a function of TR. A strong correlation was observed in xenon gas exchange between the left and right lungs (Pearson's correlation statistics: r = 0.98 and P = 0.0023 from PT image; r = 0.997 and P = 0.0002 from RBC image) showing that repeated acquisitions in five healthy rats were regionally consistent between the left and right lungs.

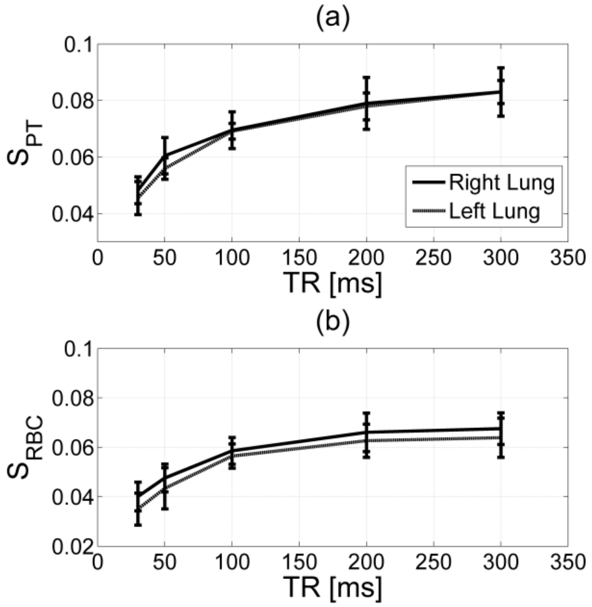

Figure 3.9: Mean signals measured from all rats for PT (a) and RBC images (b) as a function of TR values: 30, 50, 100, 200, and 300 ms.

3.5 Discussion

In this work, a single-shot spiral k-space encoding strategy was applied to IDEAL imaging for separation of hyperpolarized ^{129}Xe signals originating from gas, PT and RBC compartments in the rat lung within a breath-hold interval (4 s). To achieve the necessary spatial resolution (3.3 mm) with minimal T_2^* blurring, a relatively short spiral read-out time, T_{read}, (2.8 ms) on the order of T_2^* was found to be important and was facilitated in this study using a high performance insertable gradient system to achieve the required G_{max} and SR. Although the theoretical PSF is an approximation, good agreement was shown with experimental spatial resolution data obtained with thermally-polarized ^{129}Xe phantom experiments. The single-shot spiral read-out also permitted the use of fewer, larger flip angle pulses to improve SNR compared to Cartesian approaches. Based on the theoretical

PSF analysis, spiral IDEAL approaches that utilize the entire dissolved phase magnetization should give an SNR improvement of a factor of approximately 3.3 for $\alpha_G = 90^o$ compared to Cartesian approaches with similar spatial resolution ($\alpha_G = 15^o$).

For *in vivo* imaging, SNR_{PT} depends significantly on the choice of both α_G with α_{PT} and polarization. The optimum value for α_G was found to be between 15^o to 20^o for the use of 10% polarization. Although the optimum value for α_{PT} was found to be 90^o, a 75^o pulse was used to reduce the side band excitation of the gas phase. In future, the use of spectrally-selective RF pulses (28) that provide $\alpha_G = 3^o$ and $\alpha_{PT} = 90^o$ with higher polarization on the order of 30% would significantly improve the SNR of the dissolved phases. Less consumption of Hp ^{129}Xe gas magnetization with $\alpha_G = 3^o$ would be sufficient to generate an SNR_G value of approximately 23 due to the three-fold improvement of polarization Figure 3.6 (a)). The use of $\alpha_G = 3^o$ and a 3-fold improvement in polarization would also result in an improvement of SNR_{PT} from 5.8 (for $\alpha_G = 18^o$) to $10.3 \times 3 = 30.9$ (for $\alpha_G = 3^o$) based on Figure 3.6 (b).

Obtaining gas images in concert with dissolved phase images is expected to be helpful for identification of corresponding ventilation defects. Gas images from both 3-point and 4-point IDEAL match well from the same rat. The reproducibility was significantly high between five healthy rats. Gas phase images are also useful for optimization of flip angle (Eqn.[3.2]) from multiple IDEAL images and for normalization purposes (e.g. to account for polarization differences) for quantitative dynamic Hp ^{129}Xe gas exchange imaging.

In comparison to the three-point IDEAL PT image, four-point IDEAL PT has lower SNR (by a factor of 1.2) and temporal resolution performance (by a factor of 1.3) owing to the use of longer echo time spacing and more RF pulses and fewer images in the reconstruction. In principle, four-point IDEAL has the advantage of separating the PT compartment from the RBC compartment. RBC signal intensity was strong in the region of left atrium and ventricle due to the relatively high density of blood compared to other parts of the thorax.

The effect of short T_2^* and differences in T_2^* between the dissolved phases of Hp ^{129}Xe (~1.6 ms) and gas phase of Hp ^{129}Xe (~6.0 ms) requires further discussion. On the IDEAL acquisition side, the appropriate T_2^* values for the different species is explicitly accounted for in the NSA plot (Figure 3.4) when choosing the echo times which gives the optimum separation of the IDEAL signal between the gas and dissolved phases. The relatively large chemical shift between the gas phase and the dissolved phases (~ 200 ppm) means the echo times can be quite short (~ 50 us), thereby reducing T_2^* amplitude losses, since a separate excitation is used for each IDEAL echo signal. However, the longer echo time spacing (~ 340 us) required for the 4-point IDEAL approach results in a more significant drop in SNR due to T_2^* amplitude losses compared to the 3-point IDEAL approach. To address the smaller chemical shift between the dissolved phases and short echo time, an unequally spaced short echo approach could be used in future (29). On the reconstruction side, the respective T_2^* values are not explicitly considered in this work which could affect the separation of the PT and RBC images from the gas phase images (30).

The use of the high gradient amplitude and slew rate, timing delays in the gradient waveforms, and eddy currents associated with the high performance gradient insert used in this study may lead to characteristic spiral image artifacts, including streaking and ghosting (31,32). The accuracy of the gradient encoding fields (G_X and G_Y in Figure 3.1), and corresponding geometric distortions and image quality have not been explicitly evaluated in this study. However, hyperpolarized phantom experiments showed good agreement with the geometry of the phantom and images suggesting that the k-space distortions were negligible in our previous studies (33). Image distortion and ghosting were likely minimized in the present study owing to the use of a relatively larger field-of-view. While there was some streaking artifact visible, this was only apparent at the edge of the gas phase images since the gas signal was much higher than the signal from dissolved phases. Some spiral artifacts were visible in the RBC images, likely due to the low SNR owing to the low polarization.

In this work, we have demonstrated the feasibility of measuring regional gas exchange curves for the left and right rat lungs separately. The ability to image ^{129}Xe gas exchange at various TR values (e.g. from 30 ms to 300 ms) in separate breath-holds may permit quantitative measurement of gas exchange similar to that obtained using the conventional CSSR technique but with the advantage of regional information. In particular, the slopes and intercepts of gas exchange curves (8,34-36) such as shown in Figure 3.9, allow mapping of alterations in lung structure and function associated with pulmonary disease. In particular, four-point IDEAL may provide quantitative measures of both the vascular damage and tissue thickening (i.e. pneumonitis) corresponding to the early stages of RILI following thoracic irradiation (7). By choosing smaller regions-of-interest instead of the whole left and right lungs, the gas exchange curves could be mapped using higher polarization (e.g. 50%) in future.

For *in vivo* imaging of rat lungs with the single-shot spiral IDEAL approach, high SR (3000 T/m/s) and G_{max} (300 mT/m) were used to increase the spatial resolution within an optimum read-out time. IDEAL spiral imaging could be potentially translatable to human imaging with the use of an interleaved spiral approach. Conceptually, the imaging of Hp ^{129}Xe gas exchange at TR values (e.g. 15, 30, 50, 100, 250 ms) in a single breath-hold of 10.7 s should be possible using six interleaved spirals. Figure 3.3 (b) shows the relationship between the spatial resolution and read-out time with the use of clinical gradient for six RF pulses and interleaved spiral with *FOV* of 40 cm. Furthermore, at lower field strength (e.g. 1.5 T) the spatial resolution could be improved, even at longer read-out times due to the increase in T_2^*(12). In future, 2D imaging can also be extended to multi-slice imaging using parallel imaging approaches (37) and a short duration slice-selective pulse (28). Although, five TR values would be achievable for 2D human imaging, the total scan time required for obtaining the gas exchange curves would be challenging for the case of multi-slice imaging. However, the total scan time for multi-slice human imaging might be reduced by using lower TR values to obtain the gas exchange curves. Furthermore, 2D imaging can be extended to an isotropic 3D MR imaging using an additional phase encoding gradient, undersampling approach (38) and cylindrical (39) or radial (40) k-space sampling techniques.

3.6 Conclusion

Single-shot spiral IDEAL imaging for separation of Hp ^{129}Xe gas and dissolved phase images is feasible in the rat lung. The spiral approach offers the benefits of fewer, higher flip angle RF pulses to increase the signal from the dissolved phases of Hp ^{129}Xe. An SNR improvement of approximately 3 times is expected from spiral IDEAL compared to the conventional Cartesian k-space sampling IDEAL approach. The read-out time of approximately 1.8 time T_2^* was found to be optimal based on a point spread function analysis to minimize T_2^* blurring and maximize the SNR. The rapid acquisition times of spiral IDEAL permits multiple gas/PT and gas/PT/RBC images to be acquired within a breath-hold time of a few seconds. This allows flip angle calibration and optimization and permits imaging of exchange between the gas, PT and RBC compartments for regional characterization of lung microstructure and pulmonary and vascular function. Although, the imaging approach use here was optimized for rat imaging, it could be translated for human imaging using an interleaved spiral approach in future.

3.7 Reference

1. Santyr GE, Lam WW, Ouriadov A. Rapid and efficient mapping of regional ventilation in the rat lung using hyperpolarized 3He with Flip Angle Variation for Offset of RF and Relaxation (FAVOR). Magn Reson Med 2008;59(6):1304-1310.

2. Ouriadov A, Farag A, Kirby M, McCormack DG, Parraga G, Santyr GE. Pulmonary hyperpolarized Xe morphometry for mapping xenon gas concentrations and alveolar oxygen partial pressure: Proof-of-concept demonstration in healthy and COPD subjects. Magn Reson Med 2014.

3. Mugler JP, 3rd, Altes TA, Ruset IC, et al. Simultaneous magnetic resonance imaging of ventilation distribution and gas uptake in the human lung using hyperpolarized xenon-129. Proceedings of the National Academy of Sciences of the United States of America 2010;107(50):21707-21712.

4. Qing K, Mugler JP, Altes TA, et al. Assessment of lung function in asthma and COPD using hyperpolarized Xe-129 chemical shift saturation recovery spectroscopy and dissolved-phase MRI. Nmr Biomed 2014;27(12):1490-1501.

5. Mansson S, Wolber J, Driehuys B, Wollmer P, Golman K. Characterization of diffusing capacity and perfusion of the rat lung in a lipopolysaccaride disease model using hyperpolarized Xe-129. Magn Reson Med 2003;50(6):1170-1179.

6. Abdeen N, Cross A, Cron G, et al. Measurement of xenon diffusing capacity in the rat lung by hyperpolarized 129Xe MRI and dynamic spectroscopy in a single breath-hold. Magn Reson Med 2006;56(2):255-264.

7. Fox MS, Ouriadov A, Thind K, et al. Detection of radiation induced lung injury in rats using dynamic hyperpolarized Xe-129 magnetic resonance spectroscopy. Med Phys 2014;41(7).

8. Stewart NJ, Leung G, Norquay G, et al. Experimental validation of the hyperpolarized Xe chemical shift saturation recovery technique in healthy volunteers and subjects with interstitial lung disease. Magn Reson Med 2014.

9. Driehuys B, Cofer GP, Pollaro J, Mackel JB, Hedlund LW, Johnson GA. Imaging alveolar-capillary gas transfer using hyperpolarized Xe-129 MRI. Proceedings of the National Academy of Sciences of the United States of America 2006;103(48) :18278-18283.

10. Muradian I, Patz S, Butler JP, et al. Hyperpolarized 129Xe human pulmonary gas exchange with 3-point Dixon technique. Proceedings of the 14th Annual Meeting of ISMRM 2006;Seattle(Washington):abstract 1297.

11. Ouriadov AV, Fox M, L. F-W, McKenzie C, Santyr G. Hyperpolarized 129Xe Gas and Dissolved Phase Lung Imaging using IDEAL. Proceedings of the 19th Annual Meeting of ISMRM 2011;Québec(Montréal):abstract 6040.

12. Cleveland ZI, Cofer GP, Metz G, et al. Hyperpolarized Xe MR imaging of alveolar gas uptake in humans. PloS one 2010;5(8):e12192.

13. Cleveland ZI, Virgincar RS, Qi Y, Robertson SH, Degan S, Driehuys B. 3D MRI of impaired hyperpolarized 129Xe uptake in a rat model of pulmonary fibrosis. Nmr Biomed 2014;27(12):1502-1514.

14. Qing K, Ruppert K, Jiang Y, et al. Regional mapping of gas uptake by blood and tissue in the human lung using hyperpolarized xenon-129 MRI. J Magn Reson Imaging 2014;39(2):346-359.

15. Wiesinger F, Weidl E, Menzel MI, et al. IDEAL spiral CSI for dynamic metabolic MR imaging of hyperpolarized [1-13C]pyruvate. Magn Reson Med 2012;68(1):8-16.

16. Schulte RF, Sperl JI, Weidl E, et al. Saturation-recovery metabolic-exchange rate imaging with hyperpolarized [1-13C] pyruvate using spectral-spatial excitation. Magn Reson Med 2013;69(5):1209-1216.

17. Haacke EM, Brown RW, Thompson MR, Venkatesan R. Magnetic Resonance Imaging: Physical Principles and Sequence Design: Wiley: 1999.

18. Qin Q. Point spread functions of the T2 decay in k-space trajectories with long echo train. Magn Reson Med 2012;30(8):1134-1142.

19. Rahmer J, Bornert P, Groen J, Bos C. Three-dimensional radial ultrashort echo-time imaging with T2 adapted sampling. Magn Reson Med 2006;55(5):1075-1082.

20. Miller GW, Altes TA, Brookeman JR, De Lange EE, Mugler JP, 3rd. Hyperpolarized 3He lung ventilation imaging with B1-inhomogeneity correction in a single breath-hold scan. Magma 2004;16(5):218-226.

21. Ouriadov AV, Lam WW, Santyr GE. Rapid 3-D mapping of hyperpolarized 3He spin-lattice relaxation times using variable flip angle gradient echo imaging with application to alveolar oxygen partial pressure measurement in rat lungs. Magma 2009;22(5):309-318.

22. Lee JH, Hargreaves BA, Hu BS, Nishimura DG. Fast 3D imaging using variable-density spiral trajectories with applications to limb perfusion. Magn Reson Med 2003;50(6):1276-1285.

23. Foster-Gareau P, Heyn C, Alejski A, Rutt BK. Imaging single mammalian cells with a 1.5 T clinical MRI scanner. Magn Reson Med 2003;49(5):968-971.

24. Reeder SB, Brittain JH, Grist TM, Yen YF. Least-squares chemical shift separation for (13)C metabolic imaging. J Magn Reson Imaging 2007;26(4):1145-1152.

25. Zhao L, Mulkern R, Tseng CH, et al. Gradient-Echo Imaging Considerations for Hyperpolarized 129Xe MR. Journal of magnetic resonance Series B 1996;113(2):179-183.

26. Doganay O, Thind K, Wade TP, Ouriadov A, Santyr GE. A Transmit-Only/Receive-Only Radiofrequency Coil Configuration for Hyperpolarized ^{129}Xe Imaging of the Rodent Lung. Proceedings of the 21th Annual Meeting of ISMRM 2013;Lake City(Utah):abstract 1479.

27. Fox MS, Welch I, Hobson D, Santyr GE. A novel intubation technique for minimally invasive longitudinal studies of rat lungs using hyperpolarized 3He magnetic resonance imaging. Laboratory animals 2012;46(4):311-317.

28. Leung G, Norquay G, Schulte RF, Wild JM. Radiofrequency pulse design for the selective excitation of dissolved Xe. Magn Reson Med 2014.

29. Tsao J, Jiang Y. Hierarchical IDEAL: fast, robust, and multiresolution separation of multiple chemical species from multiple echo times. Magn Reson Med 2013;7 0(1):155-159.

30. Meisamy S, Hines CD, Hamilton G, et al. Quantification of hepatic steatosis with T1-independent, T2-corrected MR imaging with spectral modeling of fat: blinded comparison with MR spectroscopy. Radiology 2011;258(3):767-775.

31. Lechner SM, Sipila PT, Wiesinger F, Kerr AB, Vogel MW. Spiral Imaging Artifact Reduction: A Comparison of Two k-Trajectory Measurement Methods. J Magn Reson Imaging 2009;29(6):1485-1492.

32. Wiesinger F, Sipilae PT, Yen Y-F, et al. k-Space trajectory mapping for ultra-short, single-shot, non-Cartesian imaging. Proceedings of the 17th Annual Meeting of ISMRM 2009;Honolulu(Hawaii):abstract 6755.

33. Doganay O, Wade TP, Hegarty E, Schulte RF, McKenzie C, Santyr GE. Hyperpolarized ^{129}Xe Imaging of the Lung using Spiral IDEAL. Proceedings of the 23th Annual Meeting of ISMRM 2015;Toronto(Ontario):abstract 1497.

34. Patz S, Muradyan I, Hrovat MI, et al. Diffusion of hyperpolarized Xe-129 in the lung: a simplified model of Xe-129 septal uptake and experimental results. New J Phys 2011;13.

35. Chang YV. MOXE: a model of gas exchange for hyperpolarized 129Xe magnetic resonance of the lung. Magn Reson Med 2013;69(3):884-890.

36. Doganay O, Fox M, Santyr GE. Measurement of Pulmonary Perfusion and Gas Exchange using Hyperpolarized ^{129}Xe in a Rodent Model of Radiation-Induced

Lung Injury. Proceedings of the 22th Annual Meeting of ISMRM 2014;Milan(Italy):abstract 2290.

37. Teh K, Lee KJ, Paley MN, Wild JM. Parallel imaging of hyperpolarized helium-3 with simultaneous slice excitation. Magn Reson Med 2006;55(2):258-262.

38. Holmes JH, O'Halloran RL, Brodsky EK, Jung Y, Block WF, Fain SB. 3D hyperpolarized he-3 MRI of ventilation using a multi-echo projection acquisition. Magn Reson Med 2008;59(5):1062-1071.

39. Ruppert K, Miller GW, Altes TA, et al. Rapid hyperpolarized He-3 ventilation scanning with an optimized 3D acquisition scheme. Proceedings of the 13th Annual Meeting of ISMRM 2005;Miami(Florida):abstract 2774.

40. Kaushik SS, Robertson SH, Freeman MS, et al. Single-breath clinical imaging of hyperpolarized xe in the airspaces, barrier, and red blood cells using an interleaved 3D radial 1-point Dixon acquisition. Magn Reson Med 2015.

Chapter 4 : Early Detection of RILI using ^{129}Xe Gas Exchange

This chapter is adapted from the submitted paper: Doganay O, Stirrat E T, McKenzie C, Schulte RF, Santyr GE. Quantification of Regional Gas Exchange Changes using Hyperpolarized ^{129}Xe MRI in a Rat Model of Early Stage Radiation-induced Lung Injury. *Medical Physics*, 2015 (in revision).

4.1 Introduction

Radiation therapy is a primary treatment method for thoracic malignancies (2). However, the lung is a very radiosensitive organ (3-7), and Radiation-induced Lung Injury (RILI) is an important factor limiting thoracic radiotherapy. The incidence for moderate and severe RILI in patients after radiation therapy is 50% and 5-35% respectively (8,9). RILI generally progresses in two phases: (i) early-phase, radiation pneumonitis (RP) and (ii) late-phase, pulmonary fibrosis. RP is acute and occurs within 12 weeks after radiation therapy, mainly comprising of inflammation with symptoms of dry cough and dyspnea. Pulmonary fibrosis is irreversible and can develop as early as three months after radiation therapy. Severe pulmonary fibrosis may lead to organ failure and even death (10,11). Detection of early-stage RILI (i.e. RP) can improve outcomes by reducing normal tissue injury and late-stage effects (8,12) through adjustments in therapy plan (e.g. radiation fractionation) or use of pharmaceuticals, including radioprotectors and anti-inflammatory drugs (13-15). Pulmonary function tests (PFTs), such as spirometry, are often used for monitoring RILI but provide measures of whole-lung function only, without regional information (16). Furthermore, PFT measurements depend strongly on patient positioning and effort, obstructive disease and are sensitive to hyperfractionated therapy (total dose > 25 Gy) (17-19).

To overcome some of the limitations of PFTs and to provide regional detection of RILI, imaging techniques have been investigated. The most commonly used imaging approach for detection of RILI involves computed tomography (CT). CT is sensitive to increases in lung density (ie. microanatomy) due to RILI (16,20-22), but these increases are typically detected during the late irreversible phase of fibrosis. Furthermore, CT lung density measurements are variable and depend on the degree of inspiration and patient posture (23). CT perfusion imaging with intravenous injection of contrast agents has been shown to be sensitive to vessel damage associated with RILI as soon as 4 weeks following irradiation (6,24), but does not provide ventilation information. Single-photon emission computed tomography (SPECT) imaging is sensitive to radiation-induced reductions in regional perfusion and ventilation (25-27). Ventilation SPECT of the lungs can be based on administration of radioactive gas (e.g. ^{81m}Kr and ^{133}Xe), particulate aerosols labeled with radioactive compounds (i.e. ^{99m}Tc-DTPA) and ultrafine graphite particles labeled with ^{99m}Tc. Perfusion SPECT of lungs typically uses intravenous administration of macroaggregates of albumin labeled with ^{99m}Tc (28). Lung perfusion SPECT has been shown to be more sensitive than CT to early-phase RILI (6 weeks post-irradiation), capable of detecting approximately 20% perfusion reduction in 3D dose distributions over the range 15 to 30 Gy (29). However, quantitative SPECT images have inherently poor spatial resolution and require corrections for image-degrading factors (i.e., photon scatter and attenuation), leading to underestimation of ventilation-to-perfusion ratios (28,30,31). Positron Emission Tomography (PET) using ^{18}F-FDG offers higher spatial resolution than

SPECT and has been shown to detect metabolic changes associated with RILI within 1-3 months after radiotherapy (32). Hybrid nuclear imaging approaches such as SPECT/CT and PET/CT further improve diagnostic accuracy and sensitivity to RILI by reducing registration problems and improving corrections for image degradation (33); however, CT, SPECT and PET are all limited by radiation exposure (~3 mSV) and SPECT and PET are additionally limited by long scan times (10-30 minutes).

Although conventional proton Magnetic Resonance Imaging (MRI) of the lungs is limited by low signal, the addition of hyperpolarized (Hp) nuclei including: ^{129}Xe, ^{3}He and ^{13}C can significantly improve image quality and provide functional information (34). Hyperpolarization permits increases in signal of up to 105 from these nuclei, allowing rapid and high spatial resolution MRI of the effects of radiation on the lung. Advances in Dynamic Nuclear Polarization of ^{13}C-pyruvate (35) have enabled identification of early (days – weeks) metabolic changes in lung lactate-to-pyruvate ratios in a rat model of whole thorax irradiation (36) and right thorax irradiation which correlates well with increases in inflammatory cells (ie. macrophages) as confirmed by histology (37). The first case study on rat model has shown that there is a significant increase in ADC maps of Hp ^{3}He associated with three months-post irradiation dose of 40 Gy (38). Hp ^{3}He gas MRI has been used to investigate human subjects undergoing radiotherapy suggesting that assessment of ADC and ventilated defect percent can reveal late-phase (i.e. 6-8 months) RILI (39). Another Hp ^{3}He study showed the feasibility of detecting ventilation changes in image intensity due to late RP (40). Recently, Hp ^{129}Xe gas MRI morphometry has been shown to be sensitive to microstructural changes in lung parenchyma in rat model of RILI after two weeks irradiation (41).

Due to the relatively high solubility of xenon in biological tissues, Hp ^{129}Xe has been shown to be a promising approach for quantification of gas exchange between the alveolar airspace and the dissolved phases, principally the pulmonary tissue (PT) and red blood (RBC) compartments. Dissolved phase ^{129}Xe exhibits a large chemical shift in PT (197 ppm) and RBCs (218 ppm) relative to the gas phase signal (42). Furthermore, the Chemical Shift Saturation Recovery (CSSR) technique has been used for assessment of gas exchange curves in the whole lung (43). Fitting the CSSR data to gas exchange models permits quantification of lung function (i.e. gas exchange time constants and perfusion) as well as microstructural (i.e. alveolar wall thickness and relative blood volume) changes (1,44-46). Recently, whole lung CSSR has been shown to be sensitive to RILI at two weeks following whole thorax ^{60}Co irradiation in a rat model (47).

The above spectroscopic CSSR approaches, while quantitative, do not provide regional information, which is expected to reflect regional heterogeneity in RILI, particularly in the case of conformal irradiation approaches. MRI of Hp ^{129}Xe in the dissolved phase can be accomplished using multiple echo time MRI approaches, which exploits the phase evolution of the MRI echo signal as a function of echo time to reconstruct images corresponding to each dissolved compartment. In particular, IDEAL (Iterative Decomposition of water and fat with Echo Asymmetry and Least-square estimation) MRI has been shown to be efficient for obtaining gas and dissolved phase ^{129}Xe images in a breath-hold duration (48-51).

Recently, we have shown that an IDEAL approach utilizing single-shot spiral read-outs can provide approximately a factor of ten improvement in speed, allowing measurement of regional gas exchange curves in healthy rats (52). The purpose of this work was to investigate early-stage regional RILI changes using Hp ^{129}Xe and the rapid single shot-spiral IDEAL approach. A rat model of RILI involving unilateral exposure of the right lung to ^{60}Co radiation followed by two weeks incubation period was employed. Using this technique, separate gas, PT and RBC images were acquired at various gas transfer times in order to obtain gas exchange curves for the left and right lungs. The ability of this approach to distinguish regional changes between an irradiated rat cohort from a non-irradiated rat cohort is demonstrated. The differences are correlated with histology and reconciled in terms of pulmonary tissue thickening (i.e. RP) and vascular damage due to RILI using a theoretical gas exchange model.

4.2 Methods

4.2.1 Animal Irradiation

All procedures followed animal use protocols approved by Western University’s Animal Use Subcommittee and were consistent with the guidelines written by the Canadian Council on Animal Care (CCAC). Animal preparation details for irradiation were described previously (41). Two cohorts of five age-matched Sprague Dawley rats (374±26 g, Charles River Laboratories, Saint-Constant, Canada) were prepared for experiments. The animals in the irradiated group were exposed to a total dose of 18 Gy delivered uniformly to the right lung using a ^{60}Co source at the London Regional Cancer Program centre. A semi-circular collimator with a diameter of 4 cm was used to irradiate the right thorax only. To achieve a uniform dose distribution, 9 Gy was delivered to the rat in the supine position (at a rate of 95.1 cGy/min) and 9 Gy was delivered with the rat in the prone position (at a rate of 80.3 cGy/min), with the collimator appropriately re-positioned to irradiate only the right lung and spare the left lung. The second group of rats were not irradiated and served as age-matched controls. The irradiated and non-irradiated cohorts were housed in HEPA-filtered cages for two weeks prior to MRI. The image analyst (O. D.) was blinded to the identity of the cohorts until after the analysis of the MRI results.

4.2.2 MR Image Acquisition and Analysis:

Imaging was performed using a 3T MRI system (MR750, GEHC, Waukesha, WI), a custom-built transmit-only/receive-only birdcage coil (53) and a high performance insertable gradient system as described previously (54). Hp ^{129}Xe gas (approximately 80% enriched with 10% polarization) was obtained from a commercial xenon polarizer system (Polarean 9800, Durham, NH). All animals were imaged in the supine position following three breaths of Hp ^{129}Xe using a MRI-compatible mechanical ventilator (GE Healthcare, Malmo, Sweden) for delivery of Hp ^{129}Xe to the lung as described previously (47).

Four-point IDEAL: Images corresponding to gas, PT and RBC compartments were acquired using a single-shot spiral, four-point IDEAL pulse sequence described previously (1). Briefly, four-point IDEAL images were obtained using four echoes with a low flip angle on the gas phase, high flip angle on the dissolved phases per echo and echo-times of 340 us × m, (m=1, 2, 3, 4). The sequence was averaged 10 times during a breath-hold period of 3 s. The gas, PT and RBC images were reconstructed off-line using a Matlab routine (MathWorks, Natick, MA) as described in Schulte *et al.* (2,3).

To obtain ^{129}Xe gas exchange curves, the acquisition above was repeated for TR = 30, 50, 100, 200, 300 ms using separate breath-holds. Other pulse sequence parameters included: FOV = 70 mm, BW = 125 kHz, a nominal matrix resolution of 22. The four-point gas images were used to define ROIs corresponding to the left and right lungs of each rat (as described in Figure 4.1). ROIs were used as masks to identify the lungs on all subsequent four-point IDEAL images. The first acquired PT and RBC images were discarded since they were not weighted by *TR*. The PT and RBC images were normalized by the Hp ^{129}Xe gas image to account for any systematic differences between breath-holds, including polarization and ventilation. ^{129}Xe gas exchange signal curves (S_{PT} and S_{RBC} vs. TR) were then calculated corresponding to each lung (i.e. right vs. left) for the PT and RBC compartments respectively for further analysis as described below.

Three-point IDEAL: Compared to four-point, higher SNR, temporal and spatial resolution can be achieved using three-point IDEAL (1). However, three-point IDEAL is a less practical imaging method for processing large cohorts since it results in long scan times and gas consumption per animal. Therefore, for demonstration and conceptual purposes, representative gas-PT and gas-RBC images were acquired for separate breath-holds for only two rats in the cohort. Figure 4.1 shows a representative set of three-point IDEAL images explaining the segmentation method (used also for the four-point IDEAL gas exchange analysis above). Three-point IDEAL images of gas-RBC and gas-PT were acquired for a $FOV = 60$ mm and $TE = 50$ us × m, ($m = 1, 2, 3$) from an irradiated animal in the cohort study using two separate breath-holds. To achieve adequate SNR and spatial resolution, the representative three-point IDEAL images were averaged 15 times during each breath-hold taking advantage of higher temporal resolution.

4.2.3 Histology

Following MRI, rats were euthanized and lungs were extracted for histological analysis. The rat lungs were fixed by intratracheal infusion of 9 mL of 10% neutral-buffered formalin, and embedded in paraffin wax (57,58). The tissue was then cut into 5 µm thick tissue sections and stained with haematoxylin-eosin (H&E). The sections were chosen to avoid major airways and vessels and be evenly distributed between the apex and base of each lung. Five images were acquired from both the left and right lungs at 40× magnification corresponding to a pixel resolution of 0.23 µm using a Zeiss Axio Imager microscope with a Retiga EXi Digical CCD camera (Q Imaging, Vancouver, BC, Canada). Each image was then binarized using Matlab image processing functions (graythresh.m, Matlab). The average percent tissue area (*PTA*), was calculated from each image by counting the number of pixels with signal corresponding to all non-airspaces (e.g. parenchyma, vessels etc.) and dividing by the total number of pixels in the field using an automated binary thresh-holding approach (59). The *PTA* was calculated separately for both the left and right lungs for each rat of both cohorts.

4.2.4 Gas Exchange Curve Analysis

The theoretical gas exchange model of Mansson *et al*. (1) was fitted to the S_{PT} and S_{RBC} data as a function of *TR* for the left and right lungs. This analysis was similar to the fitting of CSSR data from whole lungs described previously (46,47) and used the following exponential function:

$$S(TR) = S_o\,(\,1 - \exp(\,TR\,/\,\tau\,)\,) + S_1\,TR \qquad [4.1]$$

;where So is the y-intercept of the linear slope, τ, is the exponential gas transfer time constant and S_1 is the linear slope. From this fitting, the parameters So, S_1, and τ were obtained separately for S_{PT} and S_{RBC} for each of the right and left lungs of all rats. The average alveolar tissue thickness (L_{PT}) and the relative RBC volume (V_{RBC}) were then calculated for both left and right lungs of all rats as described in (1). Additionally, a total PT and RBC signal, $S_{total} = S_{PT} + S_{RBC}$, for each of the right and left lungs of each rat was calculated based on the respective normalized image signal intensities at TR = 300 ms, for comparison with *PTA*.

4.2.5 Statistical Analysis

Statistical analysis was performed using Tukey's multiple comparison as part of a two-way ANOVA analysis (Graphpad Prism software, version 6, La Jolla, CA, USA) within a confidence interval of 95% to assess whether the differences in L_{PT} and V_{RBC} between left and right lungs were significant for the irradiated and non-irradiated groups. Additionally, Fisher's Least Significant Difference (LSD) multiple comparison test was used to compare the mean *PTA* of the irradiated and non-irradiated groups within a 95% confidence interval.

Unlike the Tukey's multiple comparison test, Fisher's LSD test does not correct for multi comparison of the left and right lungs, since the PTA values were not found to differentiate between the left and right lungs of either the irradiated or unirradiated cohorts, as discussed later. Finally, a correlation analyses between S_{total} and PTA was performed using two-tailed nonparametric Spearman correlation within a confidence interval of 95%.

4.3 Results

Figure 4.1 shows coronal three-point IDEAL images of (a) gas, (b) PT and (c) RBC compartments from a representative irradiated animal. The gas compartment image indicated in grey scale corresponds to the ventilation of ^{129}Xe gas in the airways and in the alveoli. The false color scale of the PT and RBC images allows the dissolved ^{129}Xe signal to be compared qualitatively and quantitatively between the left and right lungs taking advantage of higher SNR of three-point IDEAL. In particular, the PT image shows excellent correspondence with the gas image. The RBC image displayed signal both within and outside the lung and is notably higher at the center of the image, corresponding to the location of the heart and main pulmonary vessels. Figure 4.1 (d) and (e) show the RBC and PT images respectively in false color overlaid on the corresponding gas image and cropped to the contour lines obtained from the gas image. Regional intensity variations could be seen between the right (irradiated) and left (unirradiated) lungs. An increase in the ^{129}Xe tissue image signal from the irradiated right lung compared to the unirradiated left lung is apparent in Figure 4.1 (b) and (d). By contrast, the RBC image signal of the irradiated right lung in Figure 4.1 (c) and (e) is reduced compared to the un-irradiated left lung.

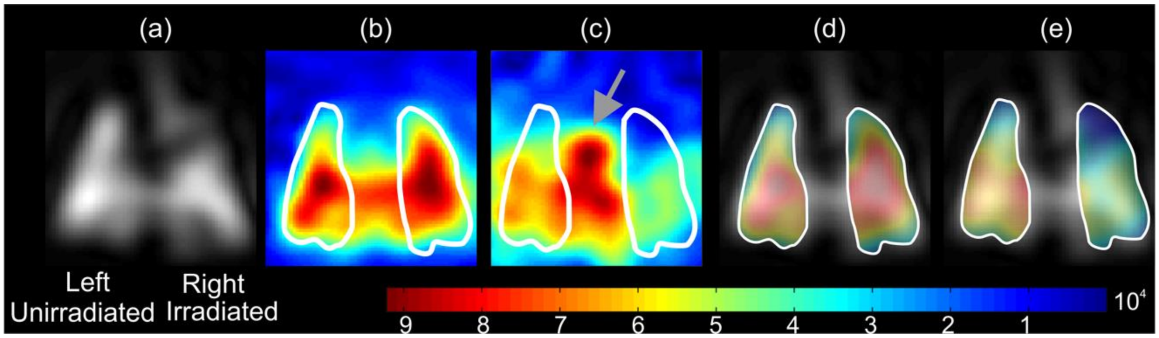

Figure 4.1: Representative coronal gas (a), PT (b), and RBC (c) images from an irradiated animal obtained using three-point IDEAL for gas-PT and gas-RBC separately. The white contour lines represent the masks for the left and right lungs used for region-of-interest (ROI) analysis. The left and right lungs of PT (d) and RBC (e) images (in color) and underlying gas images (in grey scale) with contour lines are shown for visual confirmation of the PT and RBC. The strong signal in the center of RBC image (c) as shown by the arrow appears to correspond to the left atrium, ventricle and arch of the aorta.

Experimentally measured gas exchange curves (S_{PT} and S_{RBC} as a function of TR) for both the left and right lungs of the non-irradiated and irradiated cohorts are shown respectively in Figure 4.2 (a), (b), (c), and (d). In Figure 4.2, the points represent the mean values based on all animals in the two cohorts and the error bars represent the standard deviation based on all animals in the respective cohorts. The smooth curves are the best fits to the data based on Eqn. [4.1], yielding R-square values > 0.9979±0.0018, for all animals.

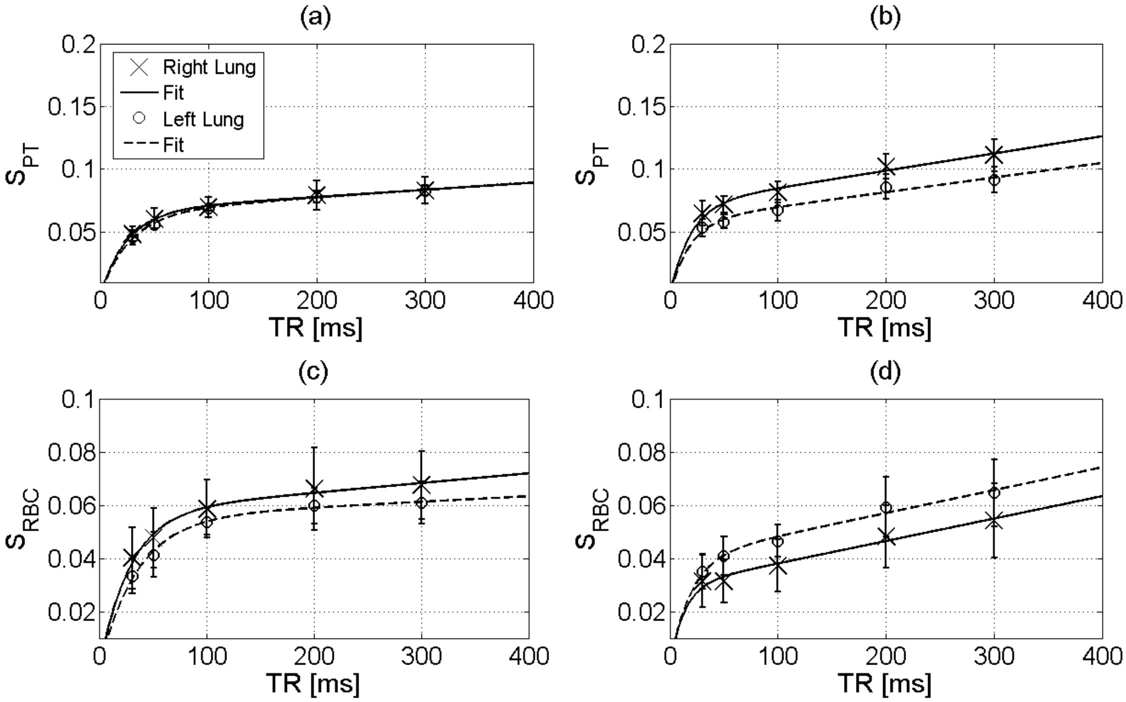

Figure 4.2: Mean gas transfer curves and corresponding fits to Eqn. [4.1] for the left and right lungs of the unirradiated group (N=5) for PT (a) and RBC (c). Mean gas transfer data and corresponding fits to Eqn. [4.1] for the left and right lungs of the irradiated group for PT (b) and RBC (d). The smooth curves represent the best fits to the data and the points and error bars represent the mean values calculated over all the animals in each respective cohort for each lung.

The individual L_{PT} and V_{RBC} values are shown is a scatter plot in Figure 4.3 and summarized in Table 4.1 for both the left and right lungs of both cohorts. The mean L_{PT} values of the left and right lungs (Figure 4.3 (a)) were determined to be 6.46±0.2 µm and 6.40±0.2 µm respectively for the non-irradiated group (Table 4.1). The irradiated cohort demonstrated a significant increase in L_{PT} compared to the non-irradiated cohort of approximately 8.2% (P = 0.0002) and 5.0% (P = 0.0497) for the right lungs and the left lungs respectively. As expected, L_{PT} was not statistically significantly different (P = 0.9682) between the left and right lungs of the non-irradiated cohort. L_{PT} was observed to be statistically significantly different between the irradiated right lungs and unirradiated left lungs of the irradiated cohort (P = 0.0210). The irradiated cohort exhibited a reduction in V_{RBC} compared to the non-irradiated cohort as shown in Figure 4.3 (b). As expected, the mean V_{RBC} values were not statistically different for the left and right lungs (P = 0.9353) of the non-irradiated cohort. Compared to the non-irradiated cohort, V_{RBC} values of the irradiated cohort decreased by 36.1% (P = 0.0002) and 11.7% (P < 0.0354) for the right and left lungs respectively. V_{RBC} values were statistically significantly different (P = 0.0223) between the irradiated right lungs and unirradiated left lungs of the irradiated group and showed variations similar to L_{PT} in Figure 4.3 (a).

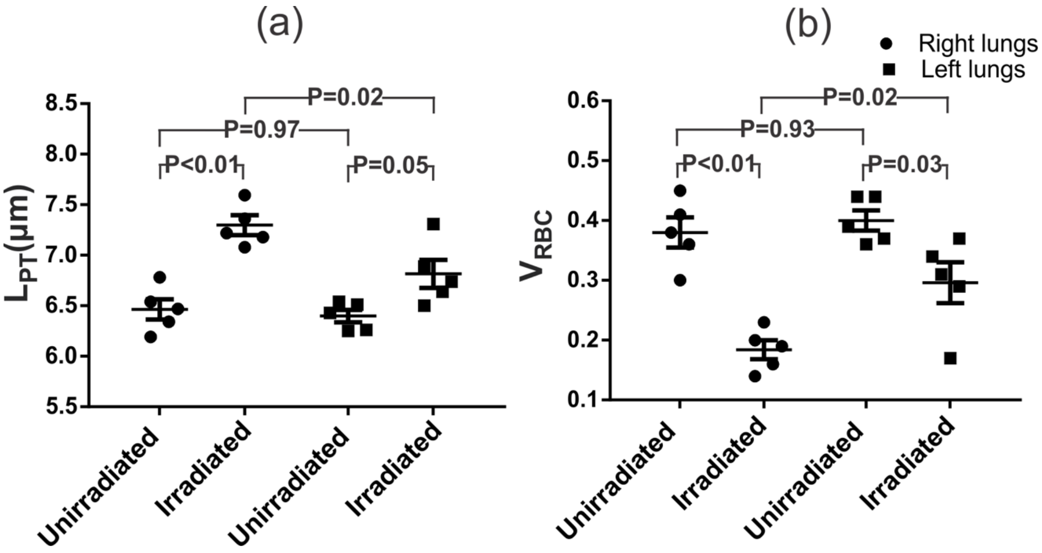

Figure 4.3: Scatter plots of calculated L_{PT} (a) and V_{RBC} (b) values for all animals for both left and right lungs from fit to Eqn. [4.1] in Figure 4.2. Corresponding p values are also shown.

Table 4.1: Summary of mean PT thickness (L_{PT}) and relative blood volume (V_{RBC}) calculated for all rats for both left and right lungs.

		Right Lung	**Left Lung**	**Right Lung**	**Left Lung**
	Rat number	L_{PT}[a] [μm]	L_{PT} [μm]	V_{RBC}[b]	V_{RBC}
NON-IRRADIATED	1	6.54±0.5	6.43±0.5	0.36±0.07	0.39±0.08
	2	6.34±0.3	6.25±0.6	0.41±0.08	0.44±0.10
	3	6.19±0.4	6.51±0.4	0.45±0.10	0.37±0.07
	4	6.47±0.4	6.26±0.5	0.38±0.11	0.44±0.08
	5	6.78±0.6	6.54±0.5	0.30±0.12	0.36±0.09
	M±SD	**6.46±0.2**	**6.40±0.2**	**0.38±0.04**	**0.40±0.04**
IRRADIATED	1	7.65±0.4	6.74±0.5	0.14±0.07	0.31±0.07
	2	7.36±0.3	7.31±0.4	0.16±0.08	0.17±0.05
	3	7.18±0.6	6.50±0.6	0.20±0.07	0.37±0.08
	4	7.08±0.5	6.64±0.6	0.23±0.08	0.34±0.10
	5	7.22±0.4	6.89±0.7	0.19±0.05	0.29±0.08
	M±SD	**7.30±0.2**	**6.82±0.3**	**0.18±0.03**	**0.30±0.03**

[a]L_{PT} and [b]V_{RBC} are the pulmonary tissue thickness and the relative blood volume respectively obtained from the Mansson model (4).

Figure 4.4 shows binarized histology images of (a) a non-irradiated and (b) an irradiated rat lung chosen to visually accentuate the differences in pulmonary tissue thickening. Figure 4.4 (c) shows a scatter plot of *PTA* values between the left and right lungs in the non-irradiated and irradiated groups. The *PTA* values from the left (23.2 ± 4.8 %) and right (22.2 ± 3.1 %) lungs in the non-irradiated group were not statistically significantly different

(P = 0.855) and close to expected values for normal animals (59) confirming that the rats in this cohort were healthy. The *PTA* values of both the irradiated right lungs and unirradiated left lungs of the irradiated cohort were observed to be significantly elevated (~26.8 %) compared to the non-irradiated cohort for both the left (P = 0.048) and right lungs (P = 0.0089), confirming the presence of radiation pneumonitis. However, there was no statistically significant difference in *PTA* measurements between the irradiated right lungs and unirradiated left lungs of the irradiated cohort (P = 0.524) showing that histology was not able to distinguish differences in RP between the irradiated right lung and the unirradiated left lung of the irradiated cohort. Figure 4.4 (d) shows a scatter plot of the measured *PTA* values for all rats versus S_{total}. The *PTA* measurements showed a significant correlation with S_{total} for both the non-irradiated (r = 0.795, P = 0.0081) and irradiated groups (r = 0.911, P = 0.0005) and the two cohorts could be distinguished on the basis of S_{total}.

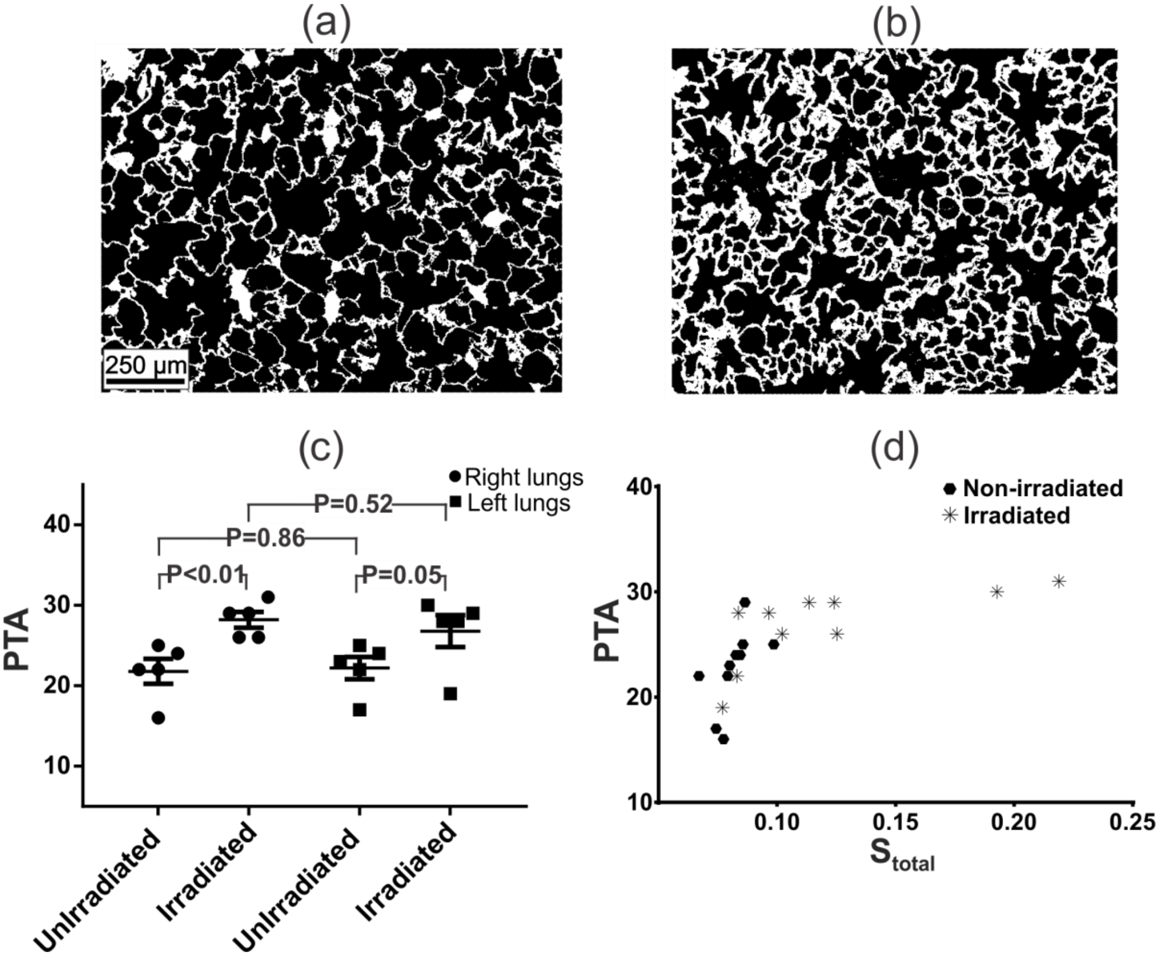

Figure 4.4: Binarized histology images of a non-irradiated (a) and an irradiated (b) rat lung obtained at 10× magnification chosen to accentuate changes in pulmonary tissue thickening (i.e. *PTA*). Scatter plot (c) showing *PTA* values for all rats and p values from Fisher's LSD multi-comparison test. Scatter plot (d) showing *PTA* and S_{total}, for all rats. The corresponding Spearman correlation coefficients were (r=0.911, p=0.0005) and (r=0.795, p=0.0081) for the irradiated and non-irradiated groups respectively.

4.4 Discussion

The results of this work confirm the feasibility of measuring changes in gas exchange curves associated with RILI regionally using Hp ^{129}Xe MRI and a single-shot spiral four-point IDEAL approach. Regional mapping of gas exchange curves based on imaging of PT and RBC compartments separately enables regional differences in RILI to be resolved, allowing contributions from RBC signal (i.e. heart and main pulmonary vessels), to be excluded from the PT signal, and thereby provide insight into radiation pneumonitis (RP) spatially, based on the choice of region of interest. Specifically, this work demonstrates that S_{PT} and S_{RBC} gas exchange curves are significantly different for irradiated rats compared to non-irradiated rats at two weeks following irradiation. Based on these differences in gas exchange curves, the calculated L_{PT} and V_{RBC} were found to be statistically larger and smaller respectively for the irradiated cohort compared to the non-irradiated cohort. The L_{PT} thickening was shown to correlate well with RP based on *PTA* determined using histology. Furthermore, differences were more significant for the irradiated right lung compared to the unirradiated left lung of the irradiated cohort, as expected.

The sufficiently high SNR of PT images enables precise measurement of S_{PT} gas exchange curves from the left and right lungs separately with a standard error of less than 5% of the mean S_{PT} (N = 5). As expected, the S_{PT} curves and calculated PT thickness in the non-irradiated group were approximately the same for the left and right lungs. The signal from blood plasma, which has the same chemical shift (197 ppm) as the PT signal, was expected to be highest from the heart and corresponding arteries on PT image. However, it did not appear to be as strong as the RBC signal from the heart. Therefore, we assume that the contribution of blood plasma to the PT signal is not significant since the Ostwald solubility of xenon in the blood plasma is approximately three times less than the RBC (60). Furthermore, since the ROIs were also chosen such that the heart was excluded, the contribution of plasma from the heart and great vessels to the tissue signal from the left and right lungs can be safely ignored. However, it should be noted that this assumption may not hold for the whole lung CSSR spectroscopy technique as discussed further below.

Both S_{PT} and S_{RBC} curves had a standard error less than reported for a whole lung CSSR spectroscopy technique (~15%) (47) confirming the ability of the IDEAL imaging approach to more accurately localize signal contributions. Furthermore, including the signal from ^{129}Xe-rich blood pool (i.e. heart and pulmonary arteries) leads to overestimation of the linear slope (S_1) and thereby the gas transfer time constant (τ_{RBC}) with CSSR techniques for long gas transfer times (or TR) on the order of seconds. The direct comparison of fitting parameters obtained in this study to previously-published whole lung CSSR spectroscopy results is not straight-forward due to the confounding effects of multiple regional PT and RBC signals affecting CSSR. As discussed previously by Chang et. al. (44) implementing overestimated fitting parameters would also cause inaccurate calculation of physiological parameters.

Nevertheless, the S_{PT} from the irradiated group showed a higher linear slope compared to the non-irradiated group, which was consistent with findings previously reported by Fox et. al. (47) for a whole lung irradiated rat model within the transfer time interval of 300 ms (61). The signal amplitude was correlated to increased tissue volume (48). A higher signal amplitude on the injured right lung compared to the non-irradiated left lung was also noted in the representative PT image (Figure 4.1). Although the pulmonary tissue thickening developed in both lungs, the impact of the injury was more severe on the irradiated right lung leading to image intensity variations when compared to the unirradiated left lung. Presumably this is due to the development of RP in the early stages of RILI (after two weeks of irradiation) resulting in tissue thickening from inflammation and/or edema. Correspondingly, the time course of exchange of Hp ^{129}Xe from the gas phase to PT will be elevated due the increased PT thickness leading to a steeper gas exchange curve (or increased S_1) in the early *TR* data points. The PT gas exchange curves from the irradiated right lungs were also statistically different from those of the unirradiated left lungs of the irradiated cohort confirming the presence of more significant RP in the right lung. This agrees with the findings previously reported by Thind *et al*. for a partially irradiated rat lung model (37).

Despite the approximations inherent to the theoretical gas exchange model used here and designed for global lung function with the CSSR technique, the average L_{PT} values agree well with previously published healthy rat pulmonary tissue thicknesses (5-6 μm) obtained using optical microscopy techniques (57). Although the mean *PTA* measurements made in this study using histology (Figure 4.4 (a) and (b)) were not capable of separating the contributions of PT and vessels (including RBC) from each other and any other tissue present, the mean *PTA* of the irradiated cohort was still found to be statistically significantly different from the non-irradiated cohort confirming that the irradiated animals had developed RP. This is perhaps not surprising since the tissue thickening due to inflammation is likely more significant than any losses in blood vessels (and RBC) due to irradiation, thus giving rise to a net increase in *PTA* (62). Nevertheless, in contrast to the

MRI approach, the *PTA* was not found to be different between the left and right lungs of the irradiated cohort, suggesting that regional differences in RP and vessel damage cannot be discriminated using histology. The densities of vessels in the histology images and choice of the slice location could help explain discrepancies in measured *PTA*. Further studies using vessel and RBC specific techniques (e.g. autofluorescence) are needed to histologically measure the pulmonary tissue and RBC separately for comparison with the L_{PT} and V_{RBC} values obtained from MRI measurements.

The selection of ROIs based on the three-point IDEAL gas images permits the assessment of RBC gas exchange curves, S_{RBC}, primarily from the pulmonary capillaries, excluding the confounding signal from the heart and other great vessels. Interestingly, there was approximately a 5% difference in S_{RBC} observed between the left and right lungs in the non-irradiated group which may due to the inherent difference between the normal total blood volumes in the healthy right and left lungs of the rat (3). Another possible explanation for the difference between the left and right lung in the non-irradiated group might be to low signal, variation in the regional pulsation (60) and the asymmetry due to the strong signal from the heart and corresponding arteries in the region of interest. Nevertheless, a relatively large standard error in S_{RBC} (~10%) compared to the S_{PT} (~5%) was observed and the S_{RBC} differ, on average, approximately two-fold in the irradiated cohort compared to the non-irradiated group.

The reduction of arterial perfusion and obstruction of capillaries in the irradiated lungs due to RILI has been observed histologically in other studies (3-5). However, reduced perfusion has only previously been reported after 30 days post-irradiation using SPECT. The early and significant reductions in S_{RBC} with irradiation observed in this study could potentially provide another method by which to quantify and discern the mechanisms of RILI, for example RP versus vascular changes known to depend on the method of radiation fractionation. Stereotactic body radiation therapy (SBRT) which is based on giving a large total dose (60 Gy) using fewer fractions (20 Gy/fraction) has been shown to provide better local tumor control and higher rates of local progression-free survival (63,64). Despite the improved survival rates with high dose approaches, lung toxicity is still a limiting factor (65) and detection of RILI after two weeks irradiation may help to reduce incidence of radiation pneumonitis. In particular, SBRT could benefit from early identification of RP and vascular changes using the approach described in this study. The two-week post-irradiation time interval chosen for this study should allow detection of the early stage pneumonitis and re-evaluation of the dose fractionation scheme or indicate the need for pharmaceuticals (i.e. radioprotective drugs). Further studies are needed to identify how could this new imaging technique would help to improve RT planning for patients.

In this study, the theoretical model of Mansson *et al.* (1) was used to extract measures of average pulmonary tissue thickness and relative blood volume regionally. This model is based on one-dimensional radial diffusive exchange in a 2D compartmental geometry. It is likely that a more sophisticated diffusive gas exchange which accounts for the 3D structure of alveoli including blood flow within surrounding capillaries would provide more physiologically insight and help to reveal RILI mechanisms in more detail, including vascular damage (61). In particular, measurement of changes in surface area between the capillaries and alveolar walls independent of changes in perfusion would help to assess early RILI. This approach could also be applied to perfusion of other organs specifically the heart using a dedicated TO/RO RF coils optimized for heart imaging (53).

The four-point IDEAL method used here should be translatable to clinical early-phase RILI detection within a single breath-hold time of 10.7 seconds using an interleaved spiral approach with *TR* values of 15, 30, 50, 100, 250 ms and would benefit by acceleration provided by parallel MRI. Higher polarizations (30-40%) should also allow measurement of regional gas exchange curves and mapping on a voxel-by-voxel basis and, potentially, isotropic 3D imaging allowing resolution of early-phase RILI regional effects associated with complex dose distributions in the lung.

4.5 Conclusion

Regional gas exchange changes associated with early (two week) radiation pneumonitis in a rat model of Radiation-Induced Lung Injury (RILI) can be measured using Hp ^{129}Xe MRI and a single-shot spiral IDEAL approach. The pulmonary tissue (PT) and red blood cell (RBC) compartments are significantly different in irradiated rats compared to non-irradiated rats. The novel approach was also capable of distinguishing irradiated lung from the non-irradiating lung suggesting that the early-phase changes can be measured regionally. The measured pulmonary tissue thickness (L_{PT}) of non-irradiated rats is in agreement with previously reported histology measurements, and the L_{PT} from irradiated rat lungs is significantly elevated compared to unirradiated lung and correlates with histology. In addition, the RBC volume (V_{RBC}) is reduced in the irradiated lung. These preliminary in vivo results confirm that this new approach can be used to quantify regional gas exchange changes associated with a rat model of early stage RILI two weeks post irradiation and potentially could be translated to humans for improving thoracic radiotherapy outcomes.

4.6 References

1. Mansson S, Wolber J, Driehuys B, Wollmer P, Golman K. Characterization of diffusing capacity and perfusion of the rat lung in a lipopolysaccaride disease model using hyperpolarized Xe-129. Magn Reson Med 2003;50(6):1170-1179.

2. Ghafoori P, Marks LB, Vujaskovic Z, Kelsey CR. Radiation-induced lung injury. Assessment, management, and prevention. Oncology 2008;22(1):37-47;52-33.

3. Ts'ao CH, Ward WF, Port CD. Radiation injury in rat lung. I. Prostacyclin (PGI2) production, arterial perfusion, and ultrastructure. Radiat Res 1983;96(2):284-293.

4. Ts'ao CH, Ward WF, Port CD. Radiation injury in rat lung. III. Plasminogen activator and fibrinolytic inhibitor activities. Radiat Res 1983;96(2):301-308.

5. Ward WF, Solliday NH, Molteni A, Port CD. Radiation injury in rat lung. II. Angiotensin-converting enzyme activity. Radiat Res 1983;96(2):294-300.

6. Milliat F, Francois A, Isoir M, Deutsch E, Tamarat R, Tarlet G, Atfi A, Validire P, Bourhis J, Sabourin JC, Benderitter M. Influence of endothelial cells on vascular smooth muscle cells phenotype after irradiation: implication in radiation-induced vascular damages. Am J Pathol 2006;169(4):1484-1495.

7. Hill RP. Radiation effects on the respiratory system. The British Journal of Radiology 2005;27(1):75-81.

8. Bentzen SM. Preventing or reducing late side effects of radiation therapy: radiobiology meets molecular pathology. Nat Rev Cancer 2006;6(9):702-713.

9. Evans ES, Hahn CA, Kocak Z, Zhou SM, Marks LB. The role of functional imaging in the diagnosis and management of late normal tissue injury. Semin Radiat Oncol 2007;17(2):72-80.

10. Koh WJ, Stelzer KJ, Peterson LM, Staker BL, Ward WF, Russell KJ, Griffin TW. Effect of pentoxifylline on radiation-induced lung and skin toxicity in rats. International journal of radiation oncology, biology, physics 1995;31(1):71-77.

11. Dion MW, Hussey DH, Doornbos JF, Vigliotti AP, Wen BC, Anderson B. Preliminary results of a pilot study of pentoxifylline in the treatment of late radiation soft tissue necrosis. International journal of radiation oncology, biology, physics 1990;19(2):401-407.

12. Rubin P, Johnston CJ, Williams JP, McDonald S, Finkelstein JN. A perpetual cascade of cytokines postirradiation leads to pulmonary fibrosis. International journal of radiation oncology, biology, physics 1995;33(1):99-109.

13. Tahamtan R, Shabestani Monfared A, Tahamtani Y, Tavassoli A, Akmali M, Mosleh-Shirazi MA, Naghizadeh MM, Ghasemi D, Keshavarz M, Haddadi GH. Radioprotective effect of melatonin on radiation-induced lung injury and lipid peroxidation in rats. Cell J 2015;17(1):111-120.

14. Citrin D, Cotrim AP, Hyodo F, Baum BJ, Krishna MC, Mitchell JB. Radioprotectors and Mitigators of Radiation-Induced Normal Tissue Injury. Oncologist 2010;15(4):360-371.

15. Serin M, Gulbas H, Gurses I, Erkal HS, Yucel N. The histopathological evaluation of the effectiveness of melatonin as a protectant against acute lung injury induced by radiation therapy in a rat model. International Journal of Radiation Biology 2007;83(3):187-193.

16. Marks LB, Munley MT, Spencer DP, Sherouse GW, Bentel GC, Hoppenworth J, Chew M, Jaszczak RJ, Coleman RE, Prosnitz LR. Quantification of radiation-induced regional lung injury with perfusion imaging. International journal of radiation oncology, biology, physics 1997;38(2):399-409.

17. Choi NC, Kanarek DJ. Toxicity of thoracic radiotherapy on pulmonary function in lung cancer. Lung Cancer 1994;10(1):S219-230.

18. Curran WJ, Jr., Moldofsky PJ, Solin LJ. Observations on the predictive value of perfusion lung scans on post-irradiation pulmonary function among 210 patients with bronchogenic carcinoma. International journal of radiation oncology, biology, physics 1992;24(1):31-36.

19. Gergel TJ, Leichman L, Nava HR, Blumenson LE, Loewen GM, Gibbs JF, Khushalani NI, Leichman CG, Bodnar LM, Douglass HO, Smith JL, Kuettel MR, Proulx GM. Effect of concurrent radiation therapy and chemotherapy on pulmonary function in patients with esophageal cancer: dose-volume histogram analysis. Cancer J 2002;8(6):451-460.

20. Wennberg B, Gagliardi G, Sundbom L, Svane G, Lind P. Early response of lung in breast cancer irradiation: radiologic density changes measured by CT and symptomatic radiation pneumonitis. International journal of radiation oncology, biology, physics 2002;52(5):1196-1206.

21. Jenkins P, Welsh A. Computed Tomography Appearance of Early Radiation Injury to the Lung: Correlation with Clinical and Dosimetric Factors. Int J Radiat Oncol 2011;81(1):97-103.

22. Mah K, Van Dyk J. Quantitative measurement of changes in human lung density following irradiation. Radiotherapy and oncology 1988;11(2):169-179.

23. Palma DA, de Koste JRV, Verbakel WFAR, Senan S. A new approach to quantifying lung damage after stereotactic body radiation therapy. Acta Oncologica 2011;50(4):509-517.

24. Hu XY, Fang XM, Chen HW, Yao XJ, Qian PY, Zhou JY, Guo J, Lerner A, Hu CH. Early detection of acute radiation-induced lung injury with multi-section CT perfusion imaging: An initial experience. Clin Radiol 2014;69(8):853-860.

25. Woel RT, Munley MT, Hollis D, Fan M, Bentel G, Anscher MS, Shafman T, Coleman RE, Jaszczak RJ, Marks LB. The time course of radiation therapy-induced reductions in regional perfusion: a prospective study with >5 years of follow-up. International journal of radiation oncology, biology, physics 2002;52(1):58-67.

26. Boersma LJ, Damen EM, de Boer RW, Muller SH, Roos CM, Valdes Olmos RA, van Zandwijk N, Lebesque JV. Dose-effect relations for local functional and structural changes of the lung after irradiation for malignant lymphoma. Radiotherapy and oncology 1994;32(3):201-209.

27. Damen EM, Muller SH, Boersma LJ, de Boer RW, Lebesque JV. Quantifying local lung perfusion and ventilation using correlated SPECT and CT data. Journal of nuclear medicine 1994;35(5):784-792.

28. Petersson J, Sanchez-Crespo A, Larsson SA, Mure M. Physiological imaging of the lung: single-photon-emission computed tomography (SPECT). Journal of applied physiology 2007;102(1):468-476.

29. Marks LB, Yu X, Vujaskovic Z, Small W, Jr., Folz R, Anscher MS. Radiation-induced lung injury. Semin Radiat Oncol 2003;13(3):333-345.

30. Petersson J, Sanchez-Crespo A, Rohdin M, Montmerle S, Nyren S, Jacobsson H, Larsson SA, Lindahl SG, Linnarsson D, Glenny RW, Mure M. Physiological evaluation of a new quantitative SPECT method measuring regional ventilation and perfusion. Journal of applied physiology 2004;96(3):1127-1136.

31. Zhang W, Wang J, Tang M, Pan J, Bai P, Lin D, Qian F, Lin F, Yang X, Zhang S. Quantitative study of lung perfusion SPECT scanning and pulmonary function testing for early radiation-induced lung injury in patients with locally advanced non-small cell lung cancer. Exp Ther Med 2012;3(4):631-635.

32. McCurdy MR, Castillo R, Martinez J, Al Hallack MN, Lichter J, Zouain N, Guerrero T. [18F]-FDG uptake dose-response correlates with radiation pneumonitis in lung cancer patients. Radiotherapy and oncology 2012;104(1):52-57.

33. Siva S, Callahan J, Kron T, Martin OA, MacManus MP, Ball DL, Hicks RJ, Hofman MS. A prospective observational study of Gallium-68 ventilation and perfusion PET/CT during and after radiotherapy in patients with non-small cell lung cancer. BMC Cancer 2014;14:740.

34. Santyr G, Fox M, Thind K, Hegarty E, Ouriadov A, Jensen M, Scholl TJ, Van Dyk J, Wong E. Anatomical, functional and metabolic imaging of radiation-induced lung injury using hyperpolarized MRI. Nmr Biomed 2014;27(12):1515-1524.

35. Ardenkjaer-Larsen JH, Fridlund B, Gram A, Hansson G, Hansson L, Lerche MH, Servin R, Thaning M, Golman K. Increase in signal-to-noise ratio of > 10,000 times in liquid-state NMR. Proceedings of the National Academy of Sciences of the United States of America 2003;100(18):10158-10163.

36. Thind K, Chen A, Friesen-Waldner L, Ouriadov A, Scholl TJ, Fox M, Wong E, VanDyk J, Hope A, Santyr G. Detection of radiation-induced lung injury using hyperpolarized C-13 magnetic resonance spectroscopy and imaging. Magn Reson Med 2013;70(3):601-609.

37. Thind K, Jensen MD, Hegarty E, Chen AP, Lim H, Martinez-Santiesteban F, Van Dyk J, Wong E, Scholl TJ, Santyr GE. Mapping metabolic changes associated with early Radiation Induced Lung Injury post conformal radiotherapy using hyperpolarized (1)(3)C-pyruvate Magnetic Resonance Spectroscopic Imaging. Radiotherapy and oncology;110(2):317-322.

38. Ward ER, Hedlund LW, Kurylo WC, Wheeler CT, Cofer GP, Dewhirst MW, Marks LB, Vujaskovic Z. Proton and hyperpolarized helium magnetic resonance imaging of radiation-induced lung injury in rats. International journal of radiation oncology, biology, physics 2004;58(5):1562-1569.

39. Mathew L, Gaede S, Wheatley A, Etemad-Rezai R, Rodrigues GB, Parraga G. Detection of longitudinal lung structural and functional changes after diagnosis of radiation-induced lung injury using hyperpolarized He-3 magnetic resonance imaging. Med Phys 2010;37(1):22-31.

40. Ireland RH, Din OS, Swinscoe JA, Woodhouse N, van Beek EJR, Wild JM, Hatton MQ. Detection of radiation-induced lung injury in non-small cell lung cancer patients using hyperpolarized helium-3 magnetic resonance imaging. Radiotherapy and Oncology 2010;97(2):244-248.

41. Ouriadov A, Fox M, Hegarty E, Parraga G, Wong E, Santyr EG. Early Stage Radiation-Induced Lung Injury Detected Using Hyperpolarized 129Xe Morphometry: Proof-of-Concept Demonstration in a Rat Model. Magn Reson Med 2015;in press.

42. Mugler JP, Driehuys B, Brookeman JR, Cates GD, Berr SS, Bryant RG, Daniel TM, deLange EE, Downs JH, Erickson CJ, Happer W, Hinton DP, Kassel NF, Maier T, Phillips CD, Saam BT, Sauer KL, Wagshul ME. MR imaging and spectroscopy using hyperpolarized Xe-129 gas: Preliminary human results. Mag Reson Med 1997;37(6):809-815.

43. Patz S, Muradian I, Hrovat MI, Ruset IC, Topulos G, Covrig SD, Frederick E, Hatabu H, Hersman FW, Butler JP. Human pulmonary imaging and spectroscopy with hyperpolarized Xe-129 at 0.2T. Acad Radiol 2008;15(6):713-727.

44. Chang YV. MOXE: a model of gas exchange for hyperpolarized 129Xe magnetic resonance of the lung. Magn Reson Med 2013;69(3):884-890.

45. Patz S, Muradyan I, Hrovat MI, Dabaghyan M, Washko GR, Hatabu H, Butler JP. Diffusion of hyperpolarized Xe-129 in the lung: a simplified model of Xe-129 septal uptake and experimental results. New J Phys 2011;13.

46. Stewart NJ, Leung G, Norquay G, Marshall H, Parra-Robles J, Murphy PS, Schulte RF, Elliot C, Condliffe R, Griffiths PD, Kiely DG, Whyte MK, Wolber J, Wild JM. Experimental validation of the hyperpolarized Xe chemical shift saturation recovery technique in healthy volunteers and subjects with interstitial lung disease. Magn Reson Med 2014.

47. Fox MS, Ouriadov A, Thind K, Hegarty E, Wong E, Hope A, Santyr GE. Detection of radiation induced lung injury in rats using dynamic hyperpolarized Xe-129 magnetic resonance spectroscopy. Med Phys 2014;41(7).

48. Driehuys B, Cofer GP, Pollaro J, Mackel JB, Hedlund LW, Johnson GA. Imaging alveolar-capillary gas transfer using hyperpolarized Xe-129 MRI. Proceedings of the National Academy of Sciences of the United States of America 2006;103(48):18278-18283.

49. Kaushik SS, Robertson SH, Freeman MS, He M, Kelly KT, Roos JE, Rackley CR, Foster WM, McAdams HP, Driehuys B. Single-breath clinical imaging of hyperpolarized xe in the airspaces, barrier, and red blood cells using an interleaved 3D radial 1-point Dixon acquisition. Magn Reson Med 2015.

50. Qing K, Mugler JP, Altes TA, Jiang Y, Mata JF, Miller GW, Ruset IC, Hersman FW, Ruppert K. Assessment of lung function in asthma and COPD using hyperpolarized Xe-129 chemical shift saturation recovery spectroscopy and dissolved-phase MRI. Nmr Biomed 2014;27(12):1490-1501.

51. Qing K, Ruppert K, Jiang Y, Mata JF, Miller GW, Shim YM, Wang C, Ruset IC, Hersman FW, Altes TA, Mugler JP, 3rd. Regional mapping of gas uptake by blood and tissue in the human lung using hyperpolarized xenon-129 MRI. J Magn Reson Imaging 2014;39(2):346-359.

52. Doganay O, Wade TP, Hegarty E, McKenzie C, Schulte RF, Santyr EG. Hyperpolarized 129Xe Imaging of the Rat Lung using Spiral IDEAL. Magn Reson Med 2015; DOI 10.1002/mrm.25911.

53. Doganay O, Thind K, Wade T, Ouriadov A, Santyr GE. Transmit-only/receive-only radiofrequency coil configuration for hyperpolarized 129Xe MRI of rat lungs. Concepts in Magnetic Resonance Part B: Magnetic Resonance Engineering 2015: DOI: 10.1002/cmr.b.21288.

54. Foster-Gareau P, Heyn C, Alejski A, Rutt BK. Imaging single mammalian cells with a 1.5 T clinical MRI scanner. Magn Reson Med 2003;49(5):968-971.

55. Wiesinger F, Weidl E, Menzel MI, Janich MA, Khegai O, Glaser SJ, Haase A, Schwaiger M, Schulte RF. IDEAL spiral CSI for dynamic metabolic MR imaging of hyperpolarized [1-13C]pyruvate. Magn Reson Med 2012;68(1):8-16.

56. Schulte RF, Sperl JI, Weidl E, Menzel MI, Janich MA, Khegai O, Durst M, Ardenkjaer-Larsen JH, Glaser SJ, Haase A, Schwaiger M, Wiesinger F. Saturation-recovery metabolic-exchange rate imaging with hyperpolarized [1-13C] pyruvate using spectral-spatial excitation. Magn Reson Med 2013;69(5):1209-1216.

57. Tanaka R, Al-Jamal R, Ludwig MS. Maturational changes in extracellular matrix and lung tissue mechanics. Journal of applied physiology 2001;91(5):2314-2321.

58. Sukstanskii AL, Yablonskiy DA. Lung morphometry with hyperpolarized 129Xe: theoretical background. Magn Reson Med 2012;67(3):856-866.

59. Takahashi A, Hamakawa H, Sakai H, Zhao X, Chen F, Fujinaga T, Shoji T, Bando T, Wada H, Date H. Noninvasive assessment for acute allograft rejection in a rat lung transplantation model. Physiol Rep 2014;2(12).

60. Ruppert K, Altes TA, Mata JF, Ruset IC, Hersman FW, Mugler JP, 3rd. Detecting pulmonary capillary blood pulsations using hyperpolarized xenon-129 chemical shift saturation recovery (CSSR) MR spectroscopy. Magn Reson Med 2015.

61. Doganay O, Fox M, Santyr GE. Measurement of Pulmonary Perfusion and Gas Exchange using Hyperpolarized 129Xe in a Rodent Model of Radiation-Induced Lung Injury. Proceedings of the 22th Annual Meeting of ISMRM 2014;Milan(Italy):abstract 2290.

62. Gayzik FS, Hoth JJ, Stitzel JD. Quantitative histology of contused lung tissue with comparison to computed tomography. Biomed Sci Instrum 2008;44:225-230.

63. Goldstraw P, Ball D, Jett JR, Le Chevalier T, Lim E, Nicholson AG, Shepherd FA. Non-small-cell lung cancer. Lancet 2011;378(9804):1727-1740.

64. Salama JK, Schild SE. Radiation therapy for oligometastatic non-small cell lung cancer. Cancer Metastasis Rev 2015.

65. Fairchild A, Harris K, Barnes E, Wong R, Lutz S, Bezjak A, Cheung P, Chow E. Palliative thoracic radiotherapy for lung cancer: a systematic review. J Clin Oncol 2008;26(24):4001-4011.

Chapter 5 : Thesis Discussion and Future Work

5.1 Thesis Discussion

Various imaging modalities such as SPECT, PET, CT, Hp MRI, and non-imaging techniques (eg. PFTs) are capable of providing functional information about RILI. Among them, Hp ^{129}Xe MR imaging technique may exceed the capacities of established modalities for detection of early phase RILI. The reason for this is ^{129}Xe diffuses in the lung air space, PT and RBC in a way similar to O_2 providing relevant functional information about the gas exchange (ie. gas exchange curves). Additionally, ^{129}Xe is a chemically inert and metabolically inactive gas in the PT and RBC. ^{129}Xe gas exchange curves can be quantitatively used to explore regional lung function when fitted to appropriate theoretical models.

In this work, a new approach using Hp ^{129}Xe MRI was developed to quantitatively measure the early phase of RILI in a rat model two weeks post-irradiation. The design and development of this approach required the establishment of multi-disciplinary interactions, including technical developments for improved Hp MRI tools. Firstly, SNR was increased by designing, constructing and optimizing a custom transmit-only / receive-only (TO/RO) coil consisting of two components: (i) a high-pass birdcage transmit-only coil that produced a homogenous B_1 magnetic field, and (ii) a saddle-shaped receive-only surface coil that allowed high sensitivity for the lung. Next, a single-shot spiral IDEAL imaging technique was implemented and optimized for Hp ^{129}Xe dissolved phase imaging. I*n vivo* results using a rat model showed regional detection of xenon exchange curves. Finally, with the use of the TO/RO coil in combination with the single-shot spiral IDEAL pulse sequence, the feasibility of early detection of RILI in a rat model two weeks-post irradiation (18 Gy) was investigated. Lung tissue for histological examinations were obtained from both an irradiated (N=5) and a non-irradiated (N=5) cohort on order to confirm whether the rats developed RILI at two weeks following irradiation. The following sections provide an overall discussion about each chapter and addresses the potential of translating this Hp ^{129}Xe MRI technique to clinical imaging.

5.2 SNR Improvement

Chapter 2 described the study performed to improve the SNR by developing a TO/RO coil configuration for rat imaging. In general, Hp ^{129}Xe gas phase imaging is conventionally achieved using birdcage volume coils, which provide acceptable transmit RF field and image homogeneity for gas imaging. However, improved SNR is necessary for imaging the dissolved phases of ^{129}Xe as they represent only 2% of the total signal available. To demonstrate the efficiency of our novel TO/RO RF coil configuration, a thermally-polarized phantom was imaged in Chapter 2. Since there was not an available dissolved phase MR sequence and the polarization of the ^{129}Xe gas was limited (~ 5%), the feasibility of the TO/RO RF coil was initially tested for imaging only the gas phase *in vivo* in rat lungs. FGRE coronal images showed an SNR improvement factor of approximately three with the new TO/RO coil configuration compared to the conventional T/R coil configuration. Although this SNR improvement was encouraging, further development was required for imaging the dissolved phases of ^{129}Xe.

In Chapter 3, an additional improvement of approximately three-fold in SNR was accomplished using a single shot-spiral IDEAL pulse sequence. The total improvement in SNR, using both the new TO/RO RF coil configuration and the single-shot IDEAL spiral imaging sequence, enabled imaging of gas, PT and RBC compartments separately. Even though polarization levels of 10% with enriched ^{129}Xe gas was used during the study, the SNR was not sufficient to achieve the necessary image quality to capture the gas exchange curves within a single breath-hold (6-10s). To address this problem, 10 sets of IDEAL images were acquired for a specific TR value within a single breath-hold time. Apart from the non-renewable nature of the noble gas polarization, the dissolved phase signal replenishes during the TR value due to transfer from the gas phase reservoir. The IDEAL sequence used this property to improve SNR by additional factor of three. Altogether, a total improvement in SNR was approximately 27-fold for each breath-hold image. Consequently, the measurement of gas exchange curves was achievable by analyzing the image intensity variations as a function of TR.

5.3 Early Detection of RILI in a Rat Model

Chapter 4 discussed the use of the new TO/RO RF coil and single-shot spiral IDEAL pulse sequence for detection of RILI in a partially irradiated rat thorax. The dynamics of gas exchange significantly changed within the two weeks post-irradiated group compared to the control group. This was consistent with previously published ^{129}Xe CSSR MR results in a whole-lung irradiated rat model (1). In particularly, we investigated whether the new imaging approach would allow detect of regional changes due to the partial-irradiation of the right thorax. This new technique was able to distinguish the irradiated lung from the unirradiated lung in the irradiated cohort group.

Compared to previous published studies using SPECT, PET, and CT, Hp ^{129}Xe MRI was also capable of differentiating the effects of RILI on the PT and RBC compartments. An increase in L_T was observed in both the left and right lungs in the irradiated cohort compared to the non-irradiated cohort (Table 4.1). Although, the increase in L_T was less in the unirradiated (left) lungs compared to the irradiated right lungs of the irradiated cohort, this result was not surprising, since it was also observed in the histology and has been reported previously in other imaging studies such as Hp ^{13}C (2). One hypothesis to explain this effect is that the whole organ responded to the irradiation delivered to one side. A significant drop in V_{RBC} was observed in the irradiated lungs, which was similar to observations in studies using SPECT lung perfusion (3,4). However, SPECT was only able to detect RILI with doses greater than 20 Gy and four weeks post-irradiation. Therefore, Hp ^{129}Xe MRI was highly sensitive to the regional changes of RILI as early as to two weeks post-irradiation with 18 Gy in the rat model.

The PTA values derived from the histology of the total pulmonary tissue and surrounding capillaries were unable to distinguish between the irradiated and unirradiated lungs in the irradiated cohort as discussed in Chapter 4. However, PTA measurements showed a statistically significant difference between the irradiated and non-irradiated rat cohorts. In the future, the histological measurements could be improved using better techniques to validate L_T and V_{RBC} measurements separately. For example, autofluorescent microscopy techniques could be used in future to verify changes in V_{RBC} (5).

5.4 Analysis of Gas Exchange Curves

The quantification of lung function using theoretical 1D gas exchange models as used in this thesis are often based on assumptions that over-simplify the alveolar geometry as shown in Figure 1.11 (b) (6). Therefore, the 1D-gas exchange model used in this thesis can only be used to calculate the variations in the 1D (i.e. radial) diffusion path length (i.e. L_T and L_C) separately for the PT and RBC compartments. Changes in the diffusion path length are then interpreted in terms of other estimations of global function of the lungs, including the relative blood volume by integration of the 1D-geometry over the entire alveolar cell volume. The 1D circularly symmetric gas exchange model excludes information about the gas exchange volume and diffusion surface area between (i) the alveolar air space and the PT compartment, and (ii) the PT and RBC compartments. This information is more appropriately extracted using a 3D-gas exchange model of the alveolus.

Another 1D-gas exchange model, the MOXE model, also interprets CSSR gas exchange data through diffusion path lengths by solving diffusion equations (7). In the MOXE model, the missing link between the diffusion path length and the CSSR measurement is provided using two normalization factors including the surface-to-volume ratio and barrier-to-septum ratio. The normalization factors are empirically obtained from the fitting parameters of the gas exchange curves. The first normalization factor is used to scale the solution of the diffusion equations between the gas and PT (8). The second normalization factor is used to scale the solution of the diffusion equations between the PT and RBC (7).

Overall, all the existing analytical gas exchange models treat the lung as a simplified uniform 1D model to fit to the CSSR data from the whole lung. In this study, the Mansson model was used to analyze the gas exchange curves because the Mansson model was easy to implement and did not require additional normalization factors. However, as already discussed in Chapter 4 (Figure 4.1), the RBC image intensity distribution was significantly different regionally from both the gas and PT compartment images. Therefore, an improved theoretical model with a more a sophisticated 3D geometry may be important to consider for explaining the spatial variation in RBC signal intensity. Additionally, the dynamics of the gas diffusion from the PT to RBC has to consider the diffusion area, possible using a 3D numerical model (9). In future, using a 3D model, the RBC compartments could be simulated without using a scaling factor from the PT signal. In this way, a study using a 3D numerical model may reveal mechanisms of RILI changes in the RBC compartment independently from the PT compartment.

5.5 Future Work

Although SNR improvement accomplished in this thesis with the TO/RO RF coil and single-shot spiral IDEAL pulse sequence design, was able to capture the dynamics of gas exchange within a single breath-hold, this was still challenging with the relatively modest 10% polarization and required multiple breath-holds to perform averaging, especially for the low TR values. The SNR can be significantly elevated using new commercially available polarizers (i.e. Polarean 9820 ^{129}Xe hyperpolarizer, Polarean Inc., Durham) that can produce polarization levels of approximately 45%. Further improvement in polarization can be achieved by addressing the unwanted thermal gradients along the SEOP cell, improving the spin exchange interaction time between ^{129}Xe and polarized ^{87}Rb, and improving the filtration of ^{129}Xe process traps. The use of higher polarizations (~30% or higher) in future would significantly improve the ^{129}Xe dissolved phase signal. In this case, smaller flip angle values, on the order of 1-2 degrees, would be sufficient to produce enough SNR for the gas phase images. Since the low flip angles do not consume the gas reservoir magnetization, a further increase in dissolved phase SNR would be achieved due to the replenishment of dissolved phase magnetization. This could be accomplished by using a selective excitation RF pulse based on a composite pulse approach (10).

As discussed previously in Chapter 3, the read-out time (T_{read}) of the spiral k-space sampling scheme should be as low as possible to achieve the desired resolution. In this thesis, T_{read} values of 2-3 ms were obtained using a high performance insertable gradient system. Unfortunately, typical clinical gradient coil strengths are not strong enough to sample the whole k-space data within such a short T_{read}. Therefore, interleaved spiral approaches could be used to address this limitation in future. With interleaved spirals, the whole k-space data could be divided into six interleaves and sampled after the application of independent RF pulses. Using an interleaved spiral approach, the dependence on high slew rates and gradient amplitudes could be eliminated for clinical MR imaging. This could also be tested using a healthy rat.

Imaging at low magnetic field strengths (0.5 T – 1.5 T) could significantly improve the spatial resolution. The T_2^* is inversely proportional to the magnetic field strength allowing for the use of longer T_{read}. The longer T_{read} would be beneficial for improving spatial resolution or reducing the number of interleaved acquisitions required for clinical gradient configurations. Therefore, translation of the technique presented in this thesis towards human imaging would benefit from the use of an interleaved spiral approach, higher polarization, and a selective excitation RF pulse.

The MRI technique developed in this thesis can potentially be used to diagnose gas exchange abnormalities resulting in other lung diseases such as chronic obstructive pulmonary disease (COPD), asthma, and cystic fibrosis. Corresponding changes in the gas exchange curves can be helpful to detect regional physiological abnormalities. Additionally, the strong dissolved phase signal from the RBC compartment of the heart can be translated to a perfusion image by taking advantage of high polarization and optimized RF coil configurations. Similarly, white matter, grey matter and blood flow of the brain can be imaged by taking advantage of the different chemical shifts using a spiral IDEAL imaging approach in the future.

5.6 Thesis Summary

A novel Hp ^{129}Xe MRI technique was developed and used to successfully detect Radiation-Induced Lung Injury (RILI) in a rodent model as early as two-weeks post-irradiation. To test the hypothesis, firstly, a TO/RO radiofrequency coil configuration was optimized and built for hyperpolarized ^{129}Xe MRI providing a three-fold SNR improvement compared to the commercially available RF coils. Next, a single-shot spiral IDEAL MRI pulse sequence, capable of separating the Hp ^{129}Xe gas and dissolved phase images, was implemented to image rat lungs. This new imaging approach offered benefits of fewer and higher flip angle RF pulses to increase the SNR of the PT and RBC images. Additionally, the short read-out times of single-shot spiral IDEAL permitted multiple gas, PT, and RBC images to be acquired within a single breath-hold time of a few seconds. Substantially improved SNR of the PT and RBC images and short scan time permitted imaging of the exchange between the gas, PT and RBC compartments for regional characterization of lung microstructure and pulmonary and vascular function. Finally, regional gas exchange changes associated with radiation pneumonitis in a rat model of RILI was measured using a single-shot spiral IDEAL approach. An *in vivo* proof-of-concept approach was able to distinguish the irradiated lung from the non-irradiating lung. The measured pulmonary tissue thickness (L_{PT}) of non-irradiated rats were found to increase in the irradiated cohort and was in agreement with previously reported studies. Additionally, in the irradiated cohort, the L_{PT} from the irradiated rat lungs was significantly elevated compared to unirradiated lung. Furthermore, again in the irradiated cohort, the RBC volume (V_{RBC}) was significantly reduced in the irradiated lung compared to unirradiated lungs. A histological measurement of the percent tissue area (PTA) was correlated to the pathology of the irradiated and non-irradiated cohorts. The novel Hp ^{129}Xe MRI method presented in this thesis showed regional change in gas exchange curves associated with a rat model of early-phase RILI two-weeks post-irradiation. The method is a promising approach for detection of early-phase RILI and has considerable potential for translation clinic, including radiation therapy, for management of RILI.

5.7 References

1. Fox MS, Ouriadov A, Thind K, et al. Detection of radiation induced lung injury in rats using dynamic hyperpolarized Xe-129 magnetic resonance spectroscopy. Med Phys 2014;41(7).

2. Thind K, Jensen MD, Hegarty E, et al. Mapping metabolic changes associated with early Radiation Induced Lung Injury post conformal radiotherapy using hyperpolarized (13)C-pyruvate Magnetic Resonance Spectroscopic Imaging. Radiotherapy and oncology 2014;110(2):317-322.

3. Woel RT, Munley MT, Hollis D, et al. The time course of radiation therapy-induced reductions in regional perfusion: a prospective study with >5 years of follow-up. International journal of radiation oncology, biology, physics 2002;52(1):58-67.

4. Hoover DA, Reid RH, Wong E, et al. SPECT-based functional lung imaging for the prediction of radiation pneumonitis: a clinical and dosimetric correlation. J Med Imaging Radiat Oncol 2014;58(2):214-222.

5. Kuebler WM. Real-time imaging assessment of pulmonary vascular responses. Proc Am Thorac Soc 2011;8(6):458-465.

6. Mansson S, Wolber J, Driehuys B, Wollmer P, Golman K. Characterization of diffusing capacity and perfusion of the rat lung in a lipopolysaccaride disease model using hyperpolarized Xe-129. Magn Reson Med 2003;50(6):1170-1179.

7. Chang YV. MOXE: a model of gas exchange for hyperpolarized 129Xe magnetic resonance of the lung. Magn Reson Med 2013;69(3):884-890.

8. Patz S, Muradyan I, Hrovat MI, et al. Diffusion of hyperpolarized Xe-129 in the lung: a simplified model of Xe-129 septal uptake and experimental results. New J Phys 2011;13.

9. Doganay O, Fox M, Santyr GE. Measurement of Pulmonary Perfusion and Gas Exchange using Hyperpolarized ^{129}Xe in a Rodent Model of Radiation-Induced Lung Injury. Proceedings of the 22th Annual Meeting of ISMRM 2014;Milan(Italy):abstract 2290.

10. Leung G, Norquay G, Schulte RF, Wild JM. Radiofrequency pulse design for the selective excitation of dissolved Xe. Magn Reson Med 2014.

Appendix A: Calculation of Spiral PSF

$H(k_r, k_\theta)$ is the modulation transfer function in polar coordinates for the spiral k-space trajectory given by:

$$H(k_r, k_\theta) = H_w(k_r, k_\theta) \times \exp(-(\frac{\Delta r T_{\mathrm{Re}\,ad}}{2\pi T_2^*}(k(r,\theta)))) \qquad \text{[A.1]}$$

;where, $H_w(k_r, k_\theta)$ is a rect function used for truncation of k-space invoking circular symmetry and can be reduced to $H_w(k_r)$ for 1D in the radial direction, Δr is the nominal resolution in k-space, T_{read} is k-space readout time. The point spread function, $h(r,\theta)$, is calculated by the inverse Fourier transform of the modulation transfer function, $H(k_r, k_\theta)$:

$$h(r,\theta) = \Im^{-1}\{H(k_r, k_\theta)\} = \int_0^{2\pi}\int_0^{\infty} H(k_r, k_\theta)\exp(-i2\pi k_r r\cos\theta) k_r dk_r dk_\theta, \qquad \text{[A.2]}$$

Substituting Eqn [A.1] in Eqn. [A.2], using the convolution identity and invoking circular symmetry, Eqn. [A.2] can be re-written as follows:

$$h(r) = H_o(2\pi f_1(k_r) f_2(k_r)) = F_1(r) * F_2(r) \qquad \text{[A.3]}$$

;where $F_1(r)$ is the Hankel transform of the rect function, $f_1(k_r)$, and integral transformations whose kernels are Bessel functions. $F_1(r)$ was calculated using *besselj.m* function for solution of zero-order Bessel functions of the first kind in Matlab (Natick MA, USA) as follows:

$$F_1(r) = H_o\{2\pi f_1(k_r)\} = 2\pi\int_0^{\infty} H_w(k_r)k_r J_o(2\pi k_r r)dk_r = 2\pi\int_0^{k_{r\max}} k_r J_o(2\pi k_r r)dk_r$$

$$= 2\pi\int_0^{k_{r\max}} \frac{1}{2\pi r}\frac{d}{dk_r}[k_r J_o(2\pi k_r r)]dk_r = 2\pi\int_0^{k_{r\max}} \frac{1}{2\pi r}\frac{d}{dk_r}[k_r J_o(2\pi k_r r)]dk_r \qquad \text{[A.4]}$$

$$F_1(r) = \frac{k_{r\max}}{r}J_1(2\pi r k_{r\max})$$

In Eqn. [A.4], $F_2(r)$ is the Hankel transform of $f_2(k_r)$ which is dependent on T_{read}/T_2 and can be solved by differentiation in the Laplace transform domain as follows:

$$F_2(r) = H_o\{f_2(r)\} = \int_0^{\infty}\exp(-Bk_r)k_r dk_r J_o(rk_r) = \frac{B}{[r^2+B^2]^{3/2}} \qquad \text{[A.5]}$$

;where, $f_2(k_r) = \exp(-\frac{\Delta r k_r}{2\pi}\frac{T_{\mathrm{Re}ad}}{T_2^*})$, $B = \frac{\Delta r}{2\pi}\frac{T_{\mathrm{Re}ad}}{T_2^*}$. $F_2(r)$ was normalized by the global minimum of $F_2(r)$ (for T_{read}/T_2^*=0.01) before the convolution.

Appendix B: Calculation of Cartesian PSF

H(k) is the modulation transfer function in Cartesian coordinates where k-space trajectories are sampled along the frequency encoding direction, k_x from $-k_{x\,max}$ *to* $k_{x\,max}$ and is given by (1,2):

$$H(k) = rect(k/W) \times \exp(-t(k)/T_2^*) \qquad [B.1]$$

;where, $t(k) = \frac{\Delta x T_{\mathrm{Re}ad}}{2\pi}(k_x)$ and Δx is the nominal resolution. Since the signal decay is dominated by T_2^*effect along the frequency encoding direction, *h(x)* is calculated analytically along x, as follows:

$$h(x) = \exp(-Ak_{\max})\frac{1}{(ix+A)}(\exp(k_{\max}(ix+A)) - \exp(-k_{\max}(ix+A))) \qquad [B.2]$$

;where $A = \frac{\Delta x T_{\mathrm{Re}ad}}{2\pi T_2^*}$.

1. Qin Q. Point spread functions of the T2 decay in k-space trajectories with long echo train. Magnetic resonance imaging 2012;30(8):1134-1142.
2. Haacke EM, Brown RW, Thompson MR, Venkatesan R. Magnetic Resonance Imaging: Physical Principles and Sequence Design: Wiley: 1999.

Appendix C: Dissolved Phase Signal Following Multiple Pulses

A Bloch equation analysis was performed including the replenishment of dissolved tissue magnetization between RF pulses. Assuming the signal from Hp ^{129}Xe is much larger than the thermal equilibrium magnetization and ignoring T_1 relaxation, the transverse (M_{xy}) and longitudinal (M_z) magnetizations following the first RF pulses ($n = 1$) are given respectively by:

$$M_z(n=1) = M_i \cos(\alpha_G) \quad [C.1]$$

$$M_{xy}(n=1) = M_i \lambda \sin(\alpha_{PT}) \quad [C.2]$$

;where, λ is the solubility of xenon, α_G and α_{PT} are the flip angles delivered to the gas and pulmonary tissue phases respectively and M_i is the initial gas phase magnetization dependent on the polarization.

The corresponding magnetizations following the second RF pulse ($n = 2$) are given by:

$$M_z(n=2) = M_z(n=1)\cos(\alpha_G) \quad [C.3]$$

$$M_{xy}(n=2) = M(TR)\, M_z(n=1)\, \lambda \sin(\alpha_{PT}) + M_i \lambda \cos(\alpha_{PT}) \sin(\alpha_{PT}) \quad [C.4]$$

;where, $M(TR)$ is the percentage replenishment of ^{129}Xe in pulmonary tissue depending on TR. $M(TR)$ was calculated by dividing the gas exchange curves by its maximum value thereby making it independent of the MRI parameters. Mansson’s gas exchange model was fitted to previously published CSSR data set of the gas transfer curve for healthy rats. Then, $M(TR)$ was calculated as follows:

$$M(TR) = (S_o [1 - \exp(-\Delta / \tau_1)] + S_1\Delta) / M(TR_{max}) \quad [C.5]$$

;where, the pulse repetition time, *TR*, corresponds to Δ in Mansson's model which is the time duration for the replenishment of Hp ^{129}Xe. τ_1, S_o, S_1 were the fitting parameters for the healthy animal respectively. Thus, *M(TR=30 ms)* and *M(TR=4 ms)* were found to be 0.5 and 0.1 respectively within a measurement uncertainty of ±5%. In other word, *M(TR)* represents the percentage concentration of Hp ^{129}Xe molecules in the pulmonary tissue pool at the end of each TR period and independent from the use of excitation flip angle.

Extending to the n^{th} excitation, the dissolved signal is given by the following:

$$S_{PT}= M_{PT}\, [\, M(TR)\, [\cos(\alpha_G)]^{n-1} \sin(\alpha_{PT}) + [\cos(\alpha_{PT})]^{n-1} \sin(\alpha_{PT})] \qquad \text{[C.6]}$$

;where M_{PT} term represents the total contribution from polarization M_i, solubility of xenon λ, and other imaging parameters (e.g., resolution, coil sensitivity etc.). The first term is the signal contribution from the kinetics of gas exchange including the effect of the flip angle on the gas phase pool and the pulmonary tissue phase pool. The second term is magnetization in the pulmonary tissue phase, which was left over after the n^{th}-1 excitation. Additionally, RF pulse width is short (<<1 ms) with respect to the relevant exchange times (tens to hundreds of ms). Therefore, exchange during the application of the RF pulse is ignored.

Appendix D: Animal Use Protocol Approval

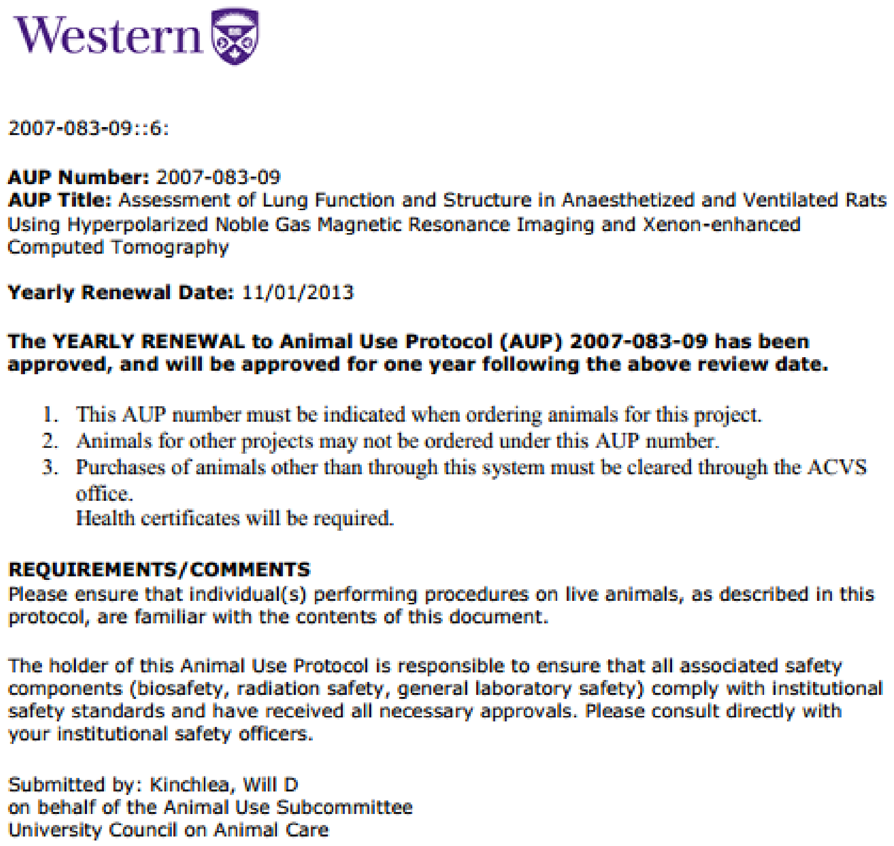

Western

2007-083-09::6:

AUP Number: 2007-083-09
AUP Title: Assessment of Lung Function and Structure in Anaesthetized and Ventilated Rats Using Hyperpolarized Noble Gas Magnetic Resonance Imaging and Xenon-enhanced Computed Tomography

Yearly Renewal Date: 11/01/2013

The YEARLY RENEWAL to Animal Use Protocol (AUP) 2007-083-09 has been approved, and will be approved for one year following the above review date.

1. This AUP number must be indicated when ordering animals for this project.
2. Animals for other projects may not be ordered under this AUP number.
3. Purchases of animals other than through this system must be cleared through the ACVS office.
   Health certificates will be required.

REQUIREMENTS/COMMENTS
Please ensure that individual(s) performing procedures on live animals, as described in this protocol, are familiar with the contents of this document.

The holder of this Animal Use Protocol is responsible to ensure that all associated safety components (biosafety, radiation safety, general laboratory safety) comply with institutional safety standards and have received all necessary approvals. Please consult directly with your institutional safety officers.

Submitted by: Kinchlea, Will D
on behalf of the Animal Use Subcommittee
University Council on Animal Care

Curriculum Vitae

DEGREES

Ph.D. Candidate	September 2011 to present Medical Biophysics University of Western Ontario, London, ON, CANADA Thesis: Hyperpolarized Xenon-129 Magnetic Resonance Imaging of Radiation-Induced Lung Injury.
M.Sc.	August 2010 Biomedical Physics Ryerson University, Toronto, ON, CANADA Thesis: Monitoring electric field-induced changes in biological tissues by using ultrasound.
B.Sc.	June 2007 Physics Ege University, Izmir, TURKEY Thesis: Sub-Nuclear Particles, Weak Interactions and Unitary Symmetry U(1), SU(2), SU(3).

PROFESSIONAL EXPERIENCE

Teaching Assistant

Western University, Department of Mathematics, London, ON., from Sep 2014 to Apr 2015.

Duties: Tutorial, invigilation, and marking for following undergrad courses:

- Calculus I (1000a)
- Applied Math (1413)

Ryerson University, Department of Physics, Toronto, ON., from Sep 2008 to May 2011.

Duties: Tutorial, laboratory instruction, invigilation, and marking for following undergrad and graduate courses:

- Medical Imaging (PCS405)
- Solid State Physics (PCS224)
- Physics I and II (PCS130)

Research Assistant

Western University, Imaging Department, London, ON., from Jun 2011 to Sep 2014.
Duties: MR technical support, RF coils design, MR sequence design, animal preparation and surgery, etc.

Ryerson University, Ultrasound Imaging, Toronto, ON., from Sep 2010 to Jun 2011.
Duties: Design magneto acoustic electrical signal experiments and analyze data, design single element ultrasound experiments, collect and analyze data, etc.

PUBLICATIONS

Refereed Journal Articles

Submitted and/or Accepted (pending revisions)

1. **O. Doganay**, E. Hegarty, C. McKenzie, R. F. Schulte, G. E. Santyr. Quantification of Regional Gas Exchange Changes using Hyperpolarized ^{129}Xe MRI in a Rat Model of Early Stage Radiation-induced Lung Injury, Medical Physics 2015 (in Revision).

Published or In Press

1. **O. Doganay**, T. Wade, E. Hegarty, C. McKenzie, R. F. Schulte, G. E. Santyr. Hyperpolarized Xenon-129 MR imaging of the rat lung using spiral IDEAL, Magnetic Resonance in Medicine 2015, DOI 10.1002/mrm.25911 (in Press).
2. **O. Doganay**, K. Thind, T. Wade, A. Ouriadov, and G. E. Santyr. Transmit-only/receive-only radiofrequency coil configuration for hyperpolarized ^{129}Xe MRI of rat lungs, Concepts in Magnetic Resonance Part B: Magnetic Resonance Engineering 2015, DOI: 10.1002/cmr.b.21288.
3. K. Wawrzyn, V. Demidov, B. Vuong, M. Harduar, C. Sun, V. X. D. Yang, **O. Doganay**, V. Toronov, and Y. Xu. Imaging the electro-kinetic response of biological tissues with optical coherence tomography, Optics Letters 2013, Vol. 38, pp. 2572-4.
4. **O. Doganay** and Y. Xu. Reversibility of electric-field induced mechanical changes (EIMC) in soft tissues, IEEE Ultrasonics, Ferroelectrics, and Frequency Control 2011, Vol. 59, pp. 552-6.
5. **O. Doganay** and Y. Xu. Electric-field induced strain in biological tissues. The Journal of the Acoustical Society of America 2010, Vol. 128, pp. 261-7.

Published Proceedings of Conferences

1. A. Pandya, **O. Doganay**, Y. Xu. Ultrasound-mediated study of the electrokinetic effects in gelatin phantoms, International Federation for Medical and Biological Engineering (IFMBE) Proceedings 2013, Vol. 39, pp 1109-12.
2. **O. Doganay** and Y. Xu. The effect of electric current in biological tissue on ultrasound echoes, Ultrasonics Symposium (IUS), IEEE International 2009, DOI: 10.1109/ULTSYM.2009.5441825, pp. 2103-6.

Refereed Proceedings of Conferences:

1. **O. Doganay**, E. Hegarty, C. McKenzie, R. F. Schulte, G. E. Santyr. Hyperpolarized ^{129}Xe Magnetic Resonance Imaging of a Rat Model of Radiation-Induced Lung Injury Involving Single-Lung Irradiation, World Congress on Medical Physics and Biomedical Engineering 2015, Abstract 2197, Toronto, ON.
2. **O. Doganay**, T. Wade, E. Hegarty, C. McKenzie, R. F. Schulte, G. E. Santyr. Hyperpolarized ^{129}Xe Imaging of the Lung using Spiral IDEAL, Proceedings of the 23th Annual Meeting of ISMRM 2015, Abstract 1497, Toronto, ON.
3. B. Zanette, **O. Doganay**, E. Hegarty, G. E. Santyr. Effect of Gas Phase Replenishment on Dissolved Phase Hyperpolarized ^{129}Xe MRI. World Congress on Medical Physics and Biomedical Engineering 2015, Abstract 1252, Toronto, ON.
4. B. Zanette, **O. Doganay**, E. Hegarty, G. E. Santyr. Effect of RF Pulse Repetition Time on Gas Transfer for Dissolved Hyperpolarized ^{129}Xe MRI, Proceedings of the 23th Annual Meeting of ISMRM 2015, Abstract 1493, Toronto, ON.
5. **O. Doganay**, E. Hegarty, C. McKenzie, R. F. Schulte, G. E. Santyr. Detection of Regional Radiation-Induced Lung Injury using Hyperpolarized ^{129}Xe Localized Magnetic Resonance Spectroscopy, 13th Imaging Network Ontario Symposium 2015, pp. 128, London, ON.
6. A. Lindenmaier, E. Hegarty, **O. Doganay**, A. Ouriadov, G. E. Santyr. Dependence of Hyperpolarized ^{129}Xe Lung MRI Morphometry on the Free Diffusion Coefficient of Xenon Gas, 13th Imaging Network Ontario Symposium 2015, pp. 139, London, ON.
7. B. Zanette, **O. Doganay**, E. Hegarty, G. E. Santyr. Effect of Gas Phase Replenishment on Dissolved Phase Hyperpolarized ^{129}Xe MRI, 13th Imaging Network Ontario Symposium 2015, pp. 154, London, ON.
8. E. Hegarty, **O. Doganay**, B. Zanette, A. Lindenmaier, G. E. Santyr. Hyperpolarized 129Xe Magnetic Resonance Imaging of Radiation-Induced Lung Injury with Correlation to Histology, 13th Imaging Network Ontario Symposium 2015, pp. 133, London, ON.
9. **O. Doganay**, M. Fox, G. E. Santyr. Measurement of Pulmonary Perfusion and Gas Exchange using Hyperpolarized ^{129}Xe in a Rodent Model of Radiation-Induced Lung Injury. Proceedings of the 22th Annual Meeting of ISMRM 2014, Abstract 2290, Milan, Italy.
10. E. Hegarty, D. Engelberts, T. Wade, K. Wawrzyn, **O. Doganay**, B. Kavanagh, G. E. Santyr. Hyperpolarized ^{129}Xe MRI for evaluation of a continuous negatively-applied pressure (CNAP) approach for recruitment of atelectasis in a rat model, American Thoracic Society (ATS) 2014, San Diego, USA.
11. **O. Doganay**, K. Thind, T.P. Wade, A. Ouriadov, G. E. Santyr. A Transmit-Only/Receive-Only Radiofrequency Coil Configuration for Hyperpolarized ^{129}Xe Imaging of the Rodent Lung. Proceedings of the 21th Annual Meeting of ISMRM 2013, Abstract 1479, Lake City, Utah.
12. **O. Doganay**, A. Farag, A. Ouriadov and G. E. Santyr. Hyperpolarized Xenon-129 Production System for MRI of the Lung, 12th Imaging Network Ontario Symposium 2013, pp. 133, London, ON.

13. Y. Xu and **O. Doganay**. Ultrasound methods to image the electrical/electrokinetic properties of biomaterials, MITACS-Fields Conference on the Mathematics of Medical Imaging 2011, Toronto, ON.
14. Y. Xu and **O. Doganay**. Monitoring the physiological-level electric-field-induced mechanical changes (PLEFIMC) in general soft biological tissues with ultrasound. Ultrasonic Imaging and Tissue Characterization (UITC) 2011, Arlington, VA.

AWARDS

1. CIHR in Cancer Research and Technology Transfer (CaRTT), London, ON. Amount: $19100/year, Sep 2013 – Present.
2. Western Graduate Research Scholarship, University of Western Ontario, London, ON. Amount: $2452/term, Sep 2011 – Present.
3. Ryerson Graduate Scholarship, Ryerson University, Toronto, ON. Amount: $7500/yearly, Sep 2008 – Sep 2010.
4. Ontario Student Opportunity Grant, Ontario Ministry of Training Colleges and Universities. Amount: $11,500, Sep 2008 – Sep 2009.